1-1-2012

# Icp-Ms Analysis of Lanthanide-Doped Nanoparticles: A Quantitative and Multiplexing Approach to Investigate Biodistribution, Blood Clearance, and Targeting

Samuel Henry Crayton
*University of Pennsylvania*, crayton@mail.med.upenn.edu

# Icp-Ms Analysis of Lanthanide-Doped Nanoparticles: A Quantitative and Multiplexing Approach to Investigate Biodistribution, Blood Clearance, and Targeting

**Abstract**
The rapidly progressing field of nanotechnology promises to revolutionize healthcare in the 21st century, with applications in the prevention, diagnosis, and treatment of a wide range of diseases. However, before nanoparticulate agents can be brought into clinical use, they must first be developed, optimized, and evaluated in animal models. In the typical pre-clinical paradigm, almost all of the optimization is done at the in vitro level, with only a few select agents reaching the level of animal studies. Since only one experimental nanoparticle formulation can be investigated in a single animal, and in vivo experiments have relatively higher complexity, cost, and time requirements, it is not feasible to evaluate a very large number of agents at the in vivo stage. A major drawback of this approach, however, is that in vitro assays do not always accurately predict how a nanoparticle will perform in animal studies. Therefore, a method that allows many agents to be evaluated in a single animal subject would allow for much more efficient and predictive optimization of nanoparticles. We have found that by incorporating lanthanide tracer metals into nanoparticle formulations, we are successfully able to use inductively coupled plasma mass spectrometry (ICP-MS) to quantitatively determine a nanoparticle's blood clearance kinetics, biodistribution, and tumor delivery. This approach was applied to evaluate both passive and active tumor targeting, as well as metabolically directed targeting of nanoparticles to low pH tumor microenvironments. Importantly, we found that these in vivo measurements could be made for many nanoparticle formulations simultaneously, in single animals, due to the high-order multiplexing capability of mass spectrometry. This approach allowed for efficient and reproducible comparison of performance between different nanoparticle formulations, by eliminating the effects of subject-to-subject variability. In the future, we envision that this "higher-throughput" evaluation of agents at the in vivo level, using ICP-MS multiplex analysis, will constitute a powerful tool to accelerate pre-clinical evaluation of nanoparticles in animal models.

**Degree Type**
Dissertation

**Degree Name**
Doctor of Philosophy (PhD)

**Graduate Group**
Bioengineering

**First Advisor**
Andrew Tsourkas

**Keywords**
ICP-MS, SPIO, Warburg effect

# ICP-MS ANALYSIS OF LANTHANIDE-DOPED NANOPARTICLES: A QUANTITATIVE AND MULTIPLEXING APPROACH TO INVESTIGATE BIODISTRIBUTION, BLOOD CLEARANCE, AND TARGETING

**Samuel Crayton**

**A DISSERTATION**

**in**

**Bioengineering**

Presented to the Faculties of the University of Pennsylvania

in

Partial Fulfillment of the Requirements for the

Degree of Doctor of Philosophy

2012

_____

**Andrew Tsourkas, Ph.D., Associate Professor of Bioengineering - Supervisor of Dissertation**

_____

**Beth Winkelstein, Ph.D., Professor of Bioengineering - Graduate Group Chairperson**

**Dissertation Committee**

Jason A. Burdick, Ph.D., Associate Professor of Bioengineering

Jerry D. Glickson, Ph.D., Research Professor of Radiology

Vladimir R. Muzykantov, M.D., Ph.D., Professor of Pharmacology

This thesis is dedicated to my parents, Kathryn and Gary

Without their love and guidance, this thesis would not have been possible…

# ABSTRACT


## ICP-MS ANALYSIS OF LANTHANIDE-DOPED NANOPARTICLES: A QUANTITATIVE AND MULTIPLEXING APPROACH TO INVESTIGATE BIODISTRIBUTION, BLOOD CLEARANCE, AND TARGETING

Samuel Crayton

Andrew Tsourkas, Ph.D.

The rapidly progressing field of nanotechnology promises to revolutionize healthcare in the 21$^{st}$ century, with applications in the prevention, diagnosis, and treatment of a wide range of diseases. However, before nanoparticulate agents can be brought into clinical use, they must first be developed, optimized, and evaluated in animal models. In the typical pre-clinical paradigm, almost all of the optimization is done at the *in vitro* level, with only a few select agents reaching the level of animal studies. Since only one experimental nanoparticle formulation can be investigated in a single animal, and *in vivo* experiments have relatively higher complexity, cost, and time requirements, it is not feasible to evaluate a very large number of agents at the *in vivo* stage. A major drawback of this approach, however, is that *in vitro* assays do not always accurately predict how a nanoparticle will perform in animal studies. Therefore, a method that allows many agents to be evaluated in a single animal subject would allow for much more efficient and predictive optimization of nanoparticles. We have found that by incorporating lanthanide tracer metals into nanoparticle formulations, we are successfully able to use inductively

coupled plasma mass spectrometry (ICP-MS) to quantitatively determine a nanoparticle's blood clearance kinetics, biodistribution, and tumor delivery. This approach was applied to evaluate both passive and active tumor targeting, as well as metabolically directed targeting of nanoparticles to low pH tumor microenvironments. Importantly, we found that these *in vivo* measurements could be made for many nanoparticle formulations simultaneously, in single animals, due to the high-order multiplexing capability of mass spectrometry. This approach allowed for efficient and reproducible comparison of performance between different nanoparticle formulations, by eliminating the effects of subject-to-subject variability. In the future, we envision that this "higher-throughput" evaluation of agents at the *in vivo* level, using ICP-MS multiplex analysis, will constitute a powerful tool to accelerate pre-clinical evaluation of nanoparticles in animal models.

# TABLE OF CONTENTS

## LIST OF TABLES

## LIST OF FIGURES

# Chapter 1: Introduction to Nanoparticle Diversity, Applications, Delivery, and Detection

## 1.1 Introduction

Extensive research is currently underway on a global scale to develop nanotechnology for applications in the prevention, diagnosis, and treatment of disease. Such innovations have the potential to revolutionize healthcare in the 21st century by improving quality of life, extending life expectancy, and reducing healthcare costs.[1] Already, nanoparticles platforms are being applied to diverse fields including regenerative medicine,[2] vaccines,[3] imaging,[4, 5] surgery,[6] and drug delivery.[7, 8] Given the variety of materials used in nanoparticle synthesis, the breadth of their applications, and growth of active targeting molecules, the number of distinct nanoparticle formulations is truly astronomical.

In order to evaluate the performance of any nanoparticle formulation, a central consideration is what amount of nanoparticles (or nanoparticle payload) has reached the particular site of interest. It is also important to examine the amount of nanoparticles delivered to off-target tissues, since this can lead to increased toxicity in drug delivery studies and diminished contrast in imaging studies. Additionally, it is helpful to examine the blood clearance profile for any nanoparticles under investigation, since this will influence nanoparticle delivery to both the target of interest and other locations.

There are a number of approaches to assessing nanoparticle concentrations *in vitro* and in tissue or blood samples. They range from direct and quantitative methods, such as radiolabeling, to indirect and qualitative surrogates, like the rate of tumor growth

following nanoparticle administration. The nanoparticle detection technique chosen by the investigator is influenced by a number of factors including convenience, cost, and level of detail required. Ideally, every evaluation of nanoparticle performance would include quantitative and absolute determination of nanoparticle particle concentration at the site of pathology, in off-target locations, and in the blood. However, the gold standard for such measurements (radiolabeling) can be inconvenient for many investigators, due to the special handling requirements of radioactive materials and quarantine considerations of exposed animal subjects. Consequently, it is common for investigators to rely on semi-quantitative measurements such as whole-animal and *ex vivo* fluorescence measurements. A convenient and cost-effective alternative to radiolabeling that provides quantitative measurements of biodistribution and blood clearance could make these data more accessible to nanoparticle investigators.

Inherent in any nanoparticle study is also the comparison of delivery between two or more formulations. For example, a passive targeting study might seek to optimize some nanoparticle property (such as size, shape, charge, surface coating, or elasticity), which requires comparison of multiple formulations that vary across the property of interest. Or an active targeting study might compare the actively targeted agent to a negative control that lacks the targeting ligand. Conventionally, these comparisons would be made by administering each agent in a separate cohort of animals. The major drawback to this approach, however, is the large animal-to-animal experimental variability of *in vivo* studies. A convenient way to compare agents while controlling for subject-to-subject variability is to employ a ratiometric/multiplex approach, whereby two

or more agents are administered simultaneously to a single subject, and a "signal" from each one can be independently resolved.

Even when radiolabeling is used to trace a nanoparticle's biodistribution and blood clearance, it is usually only feasible to examine one nanoparticle formulation in a single sample or animal. It is possible to employ a ratiometric approach with radiolabeling, using gamma emitters with resolvable energies[9] or a combination of gamma counting and scintillation,[10] but physical restrictions of energy resolution ultimately limit the number of compounds that can be simultaneously investigated.

Herein, we have sought to streamline the evaluation of sets of distinct nanoparticle formulations, *in vitro* and *in vivo*, with the use of a quantitative and multiplex assay for nanoparticle detection. Specifically, we have developed a method whereby the concentration of superparamagnetic iron oxide (SPIO) nanoparticles can be quantitatively determined using inductively coupled mass spectrometry (ICP-MS) of a lanthanide metal tracer incorporated into the nanoparticle. Importantly, the concentration of each lanthanide metal can be determined independently of other lanthanides present in the sample. Therefore, it is possible to simultaneously administer multiple SPIO formulations, with distinct physicochemical properties, to a single animal subject and orthogonally assess their blood clearance, biodistribution, and passive delivery to a tumor xenograft (Chapter 2). Investigation into the versatility of this system found that it could be easily extended to a number of other commonly used imaging and therapeutic nanoparticle constructs, such as liposomes, polymersomes, dendrimers, and gold nanoparticles (Chapter 3). The technique was then applied to compare the active targeting capability of SPIO formulations directed against distinct tumor markers (Chapter 4).

Finally, a novel pH-sensitive SPIO nanoparticle was engineered for the detection of acidic tumor microenvironments, and the ICP-MS based method was used to evaluate its performance *in vivo* (Chapter 5). In this chapter, extensive background is provided on the mechanisms of active and passive nanoparticle delivery, pH mediated delivery and imaging, commonly used nanoparticle platforms, and typical methods of nanoparticle detection and imaging *in vivo*.

## 1.2 Background

### 1.2.1 Passive and Active Targeting of Nanoparticle Platforms

#### 1.2.1a Overview

As a nascent tumor develops, it will reach a stage in which the nutrient and waste exchange through its local vasculature is insufficient to sustain its accelerated growth profile.[11] Thereafter, the tumor initiates the process of angiogenesis, in order to form new blood vessels and allow for continued growth. Often these rapidly generating blood vessels possess an abnormal basement membrane and an increased density of pericytes associated with the proliferating endothelial cells.[12] Consequently, the tumor neo-vasculature exhibits an increased level of permeability to macromolecular components. Additionally, actively growing tumors often have disorganized and disrupted lymphatic vessels, resulting in poor lymphatic drainage and impaired clearance of material from the tumor interstitium.[11] This combination of leaky vasculature and inefficient lymphatic drainage results in a phenomenon known as the enhanced permeability and retention (EPR) effect. EPR is a driving force for nanoparticles to preferentially accumulate in

regions of malignancy and is consistently exploited in studies of nanoparticle-based imaging and therapeutic agents. Tumor accumulation derived solely from the nanoparticle's blood residence time and the EPR effect is commonly referred to as passive targeting. Methods to improve nanoparticle tumor delivery, through specific interactions with malignant cells or extracellular components, are termed active targeting. Figure 1.1 depicts tumor delivery by the EPR effect and further enhancement through active targeting.

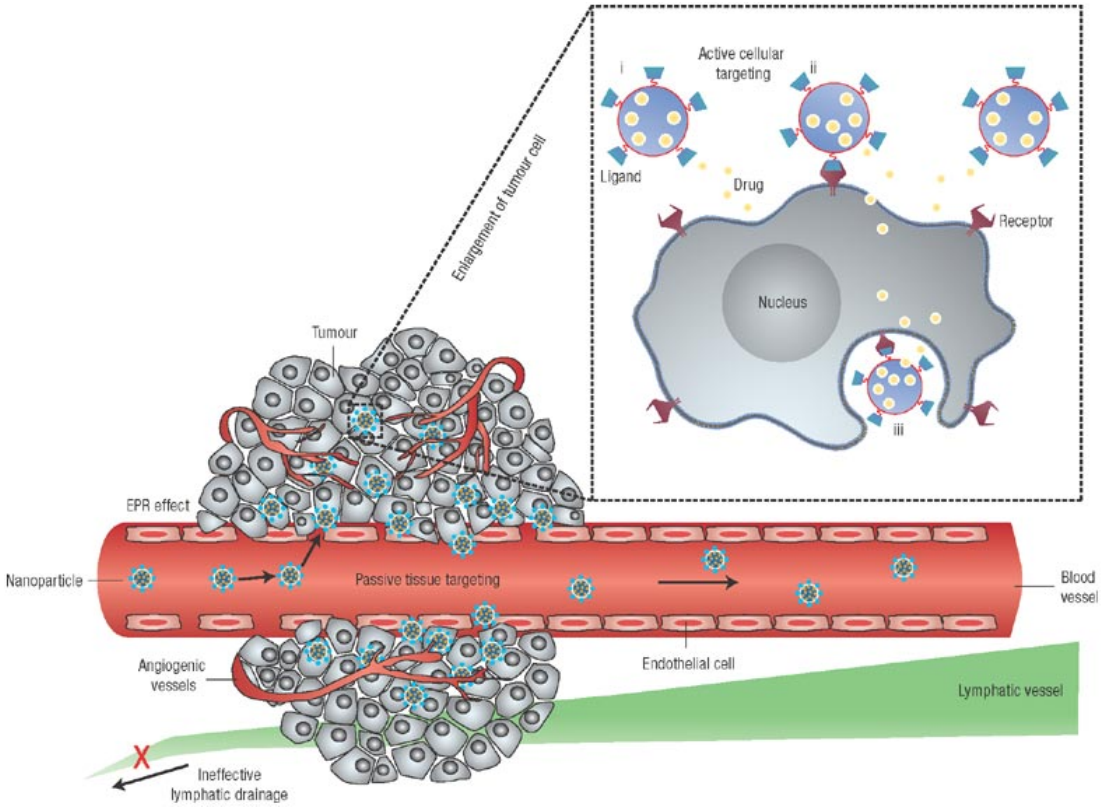


**Figure 1.1** Schematic of the enhanced permeability and retention (EPR) effect (passive targeting) followed by nanoparticle binding to tumor cell receptor (active targeting)[13]

## 1.2.1b Passive Targeting

Passive targeting of nanoparticle formulations is their preferential, but non-specific, accumulation at a tumor site secondary to the EPR effect. Even with a highly permeable tumor vasculature, many passes through the circulation are required in order for a large amount of nanoparticles to extravasate at the tumor. Therefore, a central component of passive delivery is the design of nanoparticles with long *in vivo* circulation times. One major obstacle to passive tumor delivery is the reticuloendothelial system (RES), also commonly known as the mononuclear phagocyte system (MPS), which efficiently clears nanoparticulate material from blood circulation.[14] Accordingly, nanoparticle formulations must be engineered to minimize interaction with the cells of the RES. It is known that many properties of a nanoparticle (e.g. size, shape, surface charge, hydrophilicity, and specific coating material) all influence the nanoparticle's interaction with blood and cellular components, thereby affecting circulation time. [15]

The hydrodynamic diameter of a nanoparticle has a very strong influence on circulation time and passive nanoparticle delivery.[16] Specifically, nanoparticles smaller than 5 nm are under the renal filtration threshold and are very rapidly cleared from circulation. Blood circulation time and passive delivery by EPR is usually optimized for nanoparticle sizes in the 10 – 100 nm range, where interaction with the RES is minimized. Once the nanoparticle size begins to exceed 100 nm, interaction with the RES increases again and extravasation through capillary fenestrations becomes impaired.[17]

Also critically important to nanoparticle circulation time and passive tumor delivery by EPR is surface charge. Previous studies have demonstrated that prolonged blood circulation, and therefore, optimal tumor delivery is achieved with nanoparticles displaying a neutral to mildly negative surface charge.[14, 18] When the surface charges

becomes overly negative, excessive association with phagocytic cells of the reticuloendothelial system (RES) decreases circulation time,[14, 18] and it has been commonly reported that positively charged nanoparticles are cleared very rapidly due to local electrostatic interactions near the injection site [19].

Specific properties of the nanoparticle coating material (e.g. hydrophilicity) also influence nanoparticle circulation time. Since many groups have demonstrated that incorporation of polyethylene glycol (PEG) into the surface of nanoparticles helps avoid opsonization and increases circulation times,[15, 20, 21] nanoparticle PEGylation is a very popular method to impart in vivo stealth properties.[22] Although PEGylation increases a nanoparticle's circulation time by minimizing its interactions with the RES, it may also impair the nanoparticle's ability to interact with tumor cells, thereby limiting uptake via endocytic pathways. [23, 24] This potential drawback also must be considered when designing nanoparticles for active targeting studies, so as not to have the nanoparticle's PEG brush mask or bury the active targeting ligand.

## 1.2.1c Active Targeting Strategies

Active targeting is a nanoparticle delivery strategy whereby affinity ligands on the agent's surface bind to specific receptors or biomarkers within the tumor. It is important to note that successful active targeting still relies on efficient extravasation of the nanoparticles through the permeable tumor endothelium. Therefore, the nanoparticle's physicochemical properties, which influence blood circulation and passive delivery by the EPR effect, are still critically important in the design of actively targeted nanoparticles. Once delivered to the tumor, however, actively targeted agents possess several key advantages. While completely passive targeting is dependent on poor

lymphatic drainage in order to achieve nanoparticle retention at the tumor site, active targeting also exploits specific binding to tumor receptors.[25] Thus, actively targeted nanoparticles can accumulate at higher concentrations compared to passively targeted formulations, which are more easily washed out of the tumor interstitial compartment.

Also, depending on the type and surface density of ligands on the nanoparticle, it is possible for the actively targeted agent to be internalized once it becomes bound.[26, 27] Unlike individual antibodies, nanoparticles have varying degrees of multivalency, which further increases the likelihood of cellular internalization.[28, 29] For drug delivery applications with membrane permeable drugs, nanoparticle delivery to the interstitial compartment can be sufficient to achieve a therapeutic dose. However, membrane impermeable payloads, such as hydrophilic small molecules, proteins, peptides, or nucleic acids, require the nanoparticle to deliver them into the cell. Also, when nanoparticles are internalized within cells, they payload is more efficiently trapped within the tumor region and cell surface becomes available for interaction with additional nanoparticles, resulting in greater payload delivery to the tumor. For these reasons, active targeting strategies, whereby nanoparticles are engineered to specifically bind to tumor cells and become internalized, have the potential to enhance diagnostic and therapeutic potential.

## 1.2.1d Specific Active Targeting Biomakers Examined

A number of actively targeted agents for diagnosis and treatment of cancer are currently in clinical use and an even greater number are currently being investigated. They range in scale from radiolabeled small molecules such as $^{18}$F-fluorodeoxyglucose for PET imaging of tumor metabolic activity,[30] short peptide analogs like $^{111}$In-

pentetreotide for neuroendocrine tumor imaging,[31] to antibodies such as $^{131}$I-anti-CD20 for treatment of recurrent B-cell lymphoma,[32] to nanoparticle assemblies for magnetic resonance imaging of tumors.[33] Various specific receptors have been targeted including folate,[34] transferrin,[35] EGFR,[36] IL2,[37] and many others. In addition to directly targeting surface receptors on malignant cells, contrast agents have been developed for to detect neovascularization[38, 39] and apoptosis,[40, 41] two phenomena associated with tumorigenesis. In Chapter 4, three specific active targeting receptor/ligand pairs will be examined and background on these is provided below:

*HER2/neu Receptor and Affibody Ligand*

Human epidermal growth factor receptor 2 (HER2/neu) is a surface receptor tyrosine kinase involved in signal transduction pathways of cell growth and differentiation.[42] It is overexpressed in approximately 30% of breast cancers, where it correlates with increased tumor aggressiveness and metastatic potential.[43, 44] HER2/neu may also be overexpressed in ovarian cancer,[45] colorectal cancer,[46] and aggressive forms of endometrial carcinoma.[47] For these reasons, HER2/neu was identified as a promising target for tumor active targeting strategies, and an anti-HER2/neu monoclonal antibody (trastuzumab, Herceptin) is used clinically in the treatment of HER2 positive breast cancers.[48] For nanoparticle active targeting, one very promising ligand for HER2 targeting is the HER2/neu affibody. Affibodies are an attractive class of alternative scaffold proteins derived from a 58-amino acid portion of staphylococcal protein A.[49] They possess a high degree of specificity (similar to antibodies) but have a smaller molecular weight of approximately 6.6 kDa (similar to phage-derived peptides).[50, 51] The HER2/neu affibody has high specificity and pM affinity for the HER2/neu receptor, and

has been utilized for several nanoparticle-based studies, with a high degree of targeting success.[52-54]

*$\alpha_V\beta_3$ Integrin and Cyclic RGD Ligand*

$\alpha_V\beta_3$ integrin serves as a receptor for extracellular matrix proteins with exposed arginine-glycine-aspartate (RGD) motifs, including fibronectin, vitronectin, lamin, and collagen.[55-57] Integrin binding facilitates cellular migration along these matrix proteins of the intercellular space and basement membrane.[58, 59] It is expressed at low levels on epithelial and mature endothelial cells, but is overexpressed on activated endothelial cells associated with the neovascularization of tumors.[60-62] Interestingly, in tumor xenograft models $\alpha_V\beta_3$ integrin can be overexpressed both on the malignant cells, themselves, and on host-derived proliferating endothelial cells.[63] Therefore, synthetic cyclic RGD containing peptides are an attractive candidate for active targeting of rapidly growing and metastatic tumors. In fact, radiotracers based on cyclic RGD are being investigated for radiotherapy of $\alpha_V\beta_3$ integrin positive tumors and imaging with single photon emission computed tomography (SPECT) and positron emission tomography (PET).[64-66]

*HSP47 and LDS Affinity Peptide*

Heat shock protein 47 (HSP47) is a collagen binding protein belonging to the serine protease inhibitor (serpin) family.[67] Its expression is upregulated during a cellular stress response to noxious stimuli including high temperature, heavy metal exposure, and oxidative stress.[68] HSP47 is overexpressed in a range of human cancers including oral squamous cell carcinoma,[69] gastric cancer,[70] pancreatic ductal carcinoma,[71] lung cancer,[72] and colonic adenocarcinoma secondary to ulcerative colitis.[73] The ligand chosen to target HSP47 was a small peptide affinity ligand called “LDS”, based on its first three residues.

LDS was derived from phage display panning against HSP47 and its binding to HSP47 positive tumor cells has been demonstrated.[74]

## 1.2.2 pH Imaging

Besides passive nanoparticle delivery (Chapter 2) and conventional receptor/ligand based active targeting (Chapter 4), another increasingly popular strategy is to target local metabolic changes associated with malignancy. In Chapter 5, we present a novel pH-sensitive SPIO nanoparticle and evaluate its performance *in vivo* using a lanthanide tracer. Accordingly, this section contains background information on tumor pH alterations and pH imaging agents.

## 1.2.2a Tumor pH Alterations

In healthy mammalian tissues, acid-base homeostasis is maintained through a delicate balance between acid production and removal. A pH regulatory mechanism is necessary since acids are an invariable side product of both aerobic and anaerobic metabolism. In the case of aerobic metabolism, sugar is metabolized to pyruvate, which in the presence of oxygen is oxidized by the mitochondria to $CO_2$ and $H_2O$. $CO_2$ is then transported outside the cell where it is hydrated by carbonic anhydrases to form bicarbonate plus a free proton, $H^+$. In the case of anaerobic metabolism, *i.e.* in the absence of oxygen, pyruvate is reduced to lactic acid and is subsequently exported from cells. Once in the extracellular space, acids diffuse from the site of production to the blood, where they are buffered by an open and dynamic $CO_2/HCO_3^-$ system.

Although the physiological mechanisms responsible for stabilizing the intra- and extracellular pH are quite robust, many pathological conditions including cancer have

been associated with an increase in tissue acidity. This sub-physiological pH is thought to arise from the increase in glycolysis, seen in nearly all invasive cancers (even under aerobic conditions), and poor perfusion, due to a chaotic and heterogeneous microvasculature in the tumor microenvironment. Interestingly, it has been observed that even in the absence of glycolysis the extracellular pH can still reach values as low as 6.65;[75] however, it has been hypothesized that elevated glycolysis may still be needed for "hyperacidity".[76] Numerous studies have shown that the extracellular pH of human and animal tumors can reach values approaching 6.0, which is likely not possible without elevated glycolysis.[77, 78] The critical importance of identifying pathologies with sub-physiologic pH stems from studies that show low pH stimulates in vitro invasion and in vivo metastases.[79, 80] This has led to the development of numerous techniques and imaging strategies for measuring pH in vivo.

## 1.2.2b Absolute pH Imaging

In recent years, numerous methods have been developed that allow for the non-invasive assessment of tissue pH, most of which are based on magnetic resonance.[81] One common technique relies on the $^{31}$P MR resonance of phosphate.[82] Since intracellular inorganic phosphate (Pi) concentrations are higher than extracellular concentrations and the intracellular volume fraction is greater than 50%, the chemical shift of endogenous Pi is generally thought to reflect intracellular pH. Extracellular pH of tumors can also be separately measured using exogenous agents such as 3-aminopropylphosphate (3-APP).[83] 3-APP is a non-toxic, membrane impermeant compound that has a pH-dependent chemical shift, 1 ppm per pH unit, in the physiological range.

Exogenous agents have also been developed with pH-sensitive $^{19}F$ resonances.[84, 85] The almost complete lack of endogenous $^{19}F$ resonances in normal tissues combined with the high gyromagnetic ratio and large chemical shift dispersion of $^{19}F$ compounds has been reported to result in improved signal-to-noise and resolvable pH-dependent chemical shifts, compared with $^{31}P$ MRS of 3-APP. However, drawbacks of $^{19}F$ approaches include the instability of fluorinated compounds and the inability to simultaneously measure other metabolic compounds.[81]

Since the $^{1}H$ nucleus offers the highest inherent sensitivity for MR detection and because it is possible to image the spatial distribution of tissue pH with pH-sensitive $^{1}H$ resonances, numerous groups have employed imidazole-based compounds such as IEPA to measure pH *in vivo*.[86-89] IEPA is non-toxic, membrane impermeant, and has few interfering background resonances. The drawback of using IEPA, however, is that the chemical shift is only 0.7 ppm over the entire titration range, which generally means that imaging must be conducted under (high) field strengths that are not available in most clinics. An alternative $^{1}H$ MR imaging method exploits the pH-dependent magnetization transfer (CEST) between bulk phase water and either endogenous protein amide groups or exogenous probe molecules.[90, 91] pH-dependent gadolinium-based relaxation agents can also be used;[92-94] however, both of these approaches require an accurate determination of probe concentration, which is difficult to achieve *in vivo*.

Recently, magnetic resonance imaging of pH has also been performed using hyperpolarized $^{13}C$-labeled bicarbonate.[95] Specifically, pH was imaged from the ratio of signal intensities of hyperpolarized bicarbonate ($H^{13}CO_3^-$) and $^{13}CO_2$. The spatial distribution of $^{13}CO_2$ and $H^{13}CO_3^-$ was imaged in a mouse tumor model with an image

resolution of 16 x 16 voxels, each measuring 2 x 2 x 6 mm, on a 9.4T MR. This clearly represents another step towards the ultimate goal of imaging pH in human clinical pathologies; however, advancements must still be made to improve the spatiotemporal resolution of MR spectroscopy on 1.5T scanners before these techniques are adopted for routine clinical use.

### 1.2.2c Relative pH Imaging

A complimentary approach to absolute pH imaging MRS (where the pH is determined by the chemical shift of the probe) or CEST (where changes in pH influence the chemical exchange kinetics) is to detect regions of relatively abnormal pH by designing agents that preferentially accumulate in these regions. That is, the identity of the signal is not influenced by pH, but the biodistribution of the agent is influenced by pH. In this respect, such an agent has much in common with a classic receptor/ligand actively targeted molecule; the agent washes into the tumor through the enhanced permeability of the tumor vasculature and then is preferentially retained at the tumor site through pH mediated alterations in the nanoparticle's physicochemical properties.

One such targeting moiety is pH low insertion peptide (pHLIP).[96-98] At neutral or basic pH this peptide exists in equilibrium between an unstructured aqueous conformation and a conformation bound to the surface of lipid bilayers. As pH falls below 7.0, the equilibrium is directed towards a transmembrane helical conformation such that the affinity of pHLIP for cell membranes is approximately 20 times higher at low pH. Once inserted across a cell membrane at low pH, it can remain in place on the order of days. This pH-sensitive peptide has subsequently been used to produce pH

sensitive contrast agents. An optical agent consists of pHLIP directly conjugated to fluorescent dye (e.g. Cy5.5), and has been used in animal models to detect tumors and visualize tumor margins in mock surgical procedures.[99] A PET agent was constructed by pHLIP conjugation to $^{64}$CuDOTA. Studies using mouse xenografts of two human prostate cancer cell lines demonstrated the PET agent avidly concentrated at the tumor site in a pH dependent manner.[100] Beyond pHLIP agents, recently, a pH sensitive MR contrast agent has been reported that consists of magnetic nanoparticles encapsulated by PEG-PAE diblock copolymer.[101] The composite particle is stable in aqueous environments at physiologic pH and higher, but upon exposure to pH less than 7.0, the PAE polymer block is protonated, leading to destabilization of the construct and precipitation of the magnetic nanoparticles *in situ*. Once micro-precipitation occurs at the tumor site, the MR signal is amplified and diffusion of the agent out of tumor becomes more difficult.

### 1.2.3 Diversity of Nanoparticle Platforms and Properties

There are many different nanoparticle architectures, built from a wide array of materials, possessing great variation across a range of physicochemical parameters. In order to optimize nanoparticle characteristics, improve nanoparticle performance in animal models, and identify specific agents to bring to clinical testing, a method allowing convenient and quantitative detection of multiple agents in a single animal would be valuable. Chapters 2 and 3 demonstrate how ICP-MS multiplex analysis can be adapted to a wide range of nanoparticle platforms *in vivo*. Accordingly, background on these specific nanoparticle constructs is provided in the following section.

## 1.2.3a Superparamagnetic Iron Oxide (SPIO) Nanoparticles

SPIO nanoparticles typically consist of a magnetite ($Fe_3O_4$) and/or maghemite ($\gamma Fe_2O_3$) iron core and a hydrophilic surface coating.[33] In the presence of an external magnetic field, the magnetic moments of the SPIO align with the field and enhance the local magnetic flux. This effect allows them to influence both the longitudinal and transverse relaxation of surrounding protons. While the iron oxide core is responsible for generating magnetic contrast, the hydrophilic coating is used to improve the solubility, biocompatibility, and stability of the iron oxide nanoparticles. A variety of biocompatible polymers have been employed as the coating, including PEG and PLGA, and polysaccharides, such as dextran.[33, 102] Varieties of surface modifications (including attachment of targeting ligands) can subsequently be applied to SPIO, depending on the particular application.

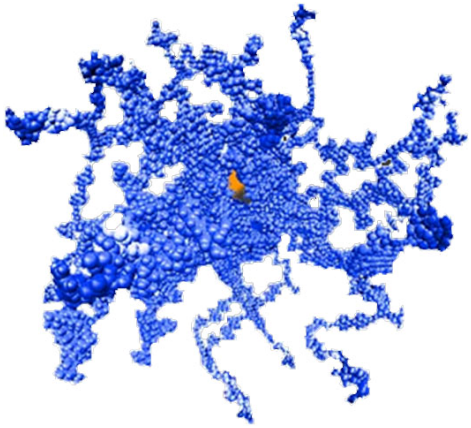

**Figure 1.2**. Illustration of dextran stabilized superparamagnetic iron oxide (SPIO), with metal core in brown and dextran chains in blue.

Clinical use of SPIO nanoparticles as MR contrast agents began in the 1980's. Since SPIO nanoparticles often exhibit uptake in the organs of the RES, they are well suited to aid in delineation of both primary tumors of the liver[103] as well as metastatic

lesions.[104] Furthermore, since SPIO nanoparticles gain access to the lymphatic drainage of tumors and lymph nodes contain a high number of phagocytic cells, SPIO can be used to survey for lymph node metastases, which aids in cancer staging and therapeutic planning.[105-107] Although this application is promising, the ultimate goal is to utilize SPIO nanoparticles for cellular and molecular imaging applications, allowing for the detection of malignancies prior to metastasis.

Detection of non-RES primary tumors with SPIO nanoparticles is currently impeded by the sensitivity limitations associated with many MR contrast agents. There are numerous approaches for improving SPIO nanoparticle sensitivity, including the optimization of SPIO magnetic properties, SPIO targeting methods, MR pulse sequences, MR hardware, and signal post-processing techniques. For example, incorporation of hetero-metals such as manganese into the iron core[108-110] has been shown to increase relaxivity, and loading multiple SPIO into single nanovesicles[111-113] increases the signal of each individual particle. Other groups have used a self-amplification approach[114] to boost the local concentration of SPIO at sites of interest, while others are developing activatable probes,[115, 116] in order to increase contrast by lowering background signal.

## 1.2.3b Liposomes and Polymersomes

Liposomes are small artificial bilayer vesicles composed of either naturally occurring lipids or a number of commercially available synthetic products. The natural or synthetic phospholipids have a hydrophobic lipid “tail” and a polar “head” constructed from various glycerylphosphate derivatives. Due to their amphiphilic nature, when phospholipid molecules are dispersed in aqueous media they can self-assemble into spherical, closed structures consisting of an aqueous core surrounded by a highly ordered

phospholipid bilayer. Consequently, liposomes can encapsulate hydrophilic compounds in their aqueous cores and intercalate hydrophobic compounds in their lipid bilayers.

Liposomes vary widely in size, number of lamellae, surface charge, permeability, and bilayer rigidity, depending on the preparative technique, synthetic conditions, and types of lipids used. Their sizes range over three orders of magnitude, from tens of nanometers to tens of micrometers. These structural parameters affect the behavior of liposomes both *in vitro* and *in vivo*. Therefore, it is critical to carefully select the liposome constituents and preparative technique for the intended application. For example, conventional liposomes are rapidly cleared from the circulation by the phagocytic cells of the RES. Therefore, for *in vivo* applications, steps such as pegylation or steric stabilization, must be taken to prolong circulation time.[117, 118] The coat has been shown to inhibit serum protein binding on the liposomal surface, thereby reducing RES sequestration, complement activation, and destabilization of the liposomal membranes. Incorporation of cholesterol into the phospholipid membrane has also been shown to improve liposome stability.[119]

Polymersomes, by contrast, are self-assembled nanovesicles composed of amphiphilic synthetic block copolymers. Most commonly polyethylene oxide (PEO) is used as the hydrophilic block. This creates a relatively intert, brush-like outer shell, which imparts "stealth" characteristics to the polymersomes and allows them to effectively avoid the reticuloendothelial system.[120] Compared to liposomes, polymersomes are far more robust, have lower membrane permeability, greater stability, and can be finely tuned through polymer selection to yield vesicles with diverse

functionality. Combined with their high stability, polymersomes have been found to exhibit long circulation times and low toxicity.[120]

The improved stability of polyersomes largely stems from the higher molecular weight of the diblock copolymers and the presence of a thick hydrophobic domain, typically ~8-10 nm. This is significantly larger than the hydrophobic domain of most liposomes, which are typically ~3 nm in thickness.[121] However, increased membrane thickness generally leads to decreased membrane fluidity and deformability, bringing the mechanical properties of polymersomes closer to viral capsids than liposomes.

Both liposomes and polymersomes are attractive platforms for imaging and drug delivery because payloads can be encapsulated within the vesicles and delivered to sites of interest. Furthermore, sequestering the payload from direct exposure to the blood can prevent it from being damaged by circulating enzymes or causing excess toxicity. For example, when liposomes are used to encapsulate imaging agents, they help overcome the rapid clearance, non-specific cellular interaction, and toxicity of free contrast, all of which result in images of diminished contrast and resolution.[122] Polyermersomes, as well, are easily transformed into imaging agents through the encapsulation of hydrophilic contrast material (*e.g.* Gd-DTPA, fluorescent dyes) within the aqueous core and/or hydrophobic fluorescent dyes within the membrane.

Nanovesicles can also be combined with active targeting strategies to direct encapsulated drugs or contrast agents to specific organs or pathologies. Targeted delivery of liposomes *in vivo* has been achieved by covalent and non-covalent coupling of site-directing ligands (such as monoclonal antibodies, proteins, vitamins, peptides, and glycolipids) to the surface of liposomes.[123] For example, PEG-shielded liposomes

functionalized with cyclic RGD have been used to target the antivascular agent combretastatin A4 to tumor vasculature.[124] The exterior surface of polymersomes can also be readily functionalized with biologically active ligands for targeting applications.[125]

## 1.2.3c Dendrimeric Nanoparticles

Dendrimers are highly uniform, spheroid polymeric nanostructures that repeatedly branch outward from an inner mulitmeric core. They are usually produced in an iterative sequence of reaction steps, where each generation results in an exponential increase in molecular weight and a geometric increase in volume.[126] For imaging applications, PAMAM dendrimers are most commonly used, and they range in size from about 1 nm to just over 13 nm, depending on the generation.[127] PAMAM dendrimers possess an ethylenediamine core and display amino groups on the surface, which provide convenient reactivity for surface modifications.[128-131] For drug delivery applications, it is also possible to encapsulate molecules inside interior cavities of a high generation dendrimer.[132]

Dendrimers possess many structural parameters, including base material, size, shape, branching, length, and surface functionality,[133] that can all affect the dendrimer's performance as an imaging or therapeutic platform. For example, smaller generation dendrimers are subject to rapid renal elimination, with blood half-lives of only a few minutes.[134] Those with charged or hydrophobic surfaces are also rapidly cleared from circulation, but tend to accumulate in the liver.[135] However, dendrimers with a neutral or hydrophilic surface, such as PEG, can exhibit blood half-lives reaching many hours.[135]

## 1.2.3d Gold Nanoparticles

The use of gold nanoparticles in biological applications began in 1971 when Faulk and Taylor invented the immunogold staining procedure for electron microscopy.[136] Gold nanoparticles which are typically sized between 0.5 and 250 nm, have been prepared in a wide variety of shapes including spherical, [137, 138] rods, [139, 140] and barbells.[141] Gold has also been used as a thin shell-coating for a dielectric core.[142] Their straightforward synthesis, excellent stability, and the ease of functionalization with targeting ligands have permitted the use of gold nanoparticles in both imaging and therapeutic applications.

Gold nanoparticles can be used with multiple imaging platforms for *in vivo* molecular imaging. For instance, gold nanoparticles complexed with a thiol-PEG coating and targeted with anti-EGFR single chain antibody fragments have been used to target tumors *in vivo* using surface enhanced Raman spectroscopy (SERS).[143] Gold nanoparticles are also being investigated as X-ray and computed tomography (CT) contrast agents. Recently, 1.9 nm gold nanoparticles, administered intravenously in a mouse tumor model, allowed for high resolution imaging of the tumor, blood vessels, and kidneys.[144] Since gold nanoparticles exhibit greater X-ray attenuation than iodine-based contrast agents, it was even possible to visualize microvasculature and neovasularization within the tumor. Beyond imaging applications, gold nanorods are also being investigated as therapeutic photothermal agents. Specifically, small axial diameter nanorods, delivered to an animal tumor, serve as highly efficient absorbers of near infrared light.[145] When short IR laser pulses are applied to the tumor volume, the laser energy is converted to heat, leading to ablation of the lesion.[146]

## 1.2.4 Detection and Imaging Modalities

There are numerous modalities to detect, quantify, and image nanoparticle formulations *in vitro*, *in vivo*, and *ex vivo*. Each method has its own unique advantages and disadvantages, which compels the investigator to select a modality that best suits the particular application. A partial list of detection and imaging modalities, along with their strengths and weaknesses is provided in table 2.1.

**Table 1.1.** Common Nanoparticle Detection and Imaging Modalities

| Method | Advantages | Disadvantages / Limitations | Quantitative | Multiplex |
|---|---|---|---|---|
| Nuclear PET/SPECT | Very High Sensitivity, Functional Information | Poor Resolution, Ionizing Radiation, Agent Requires EHRS Handling | Yes | Possible 2-3 |
| Optical / Fluorescence | High Sensitivity, Ease of Use | Lower Resolution, Altered or Prevented by Tissue Type/Depth | Semi | Yes |
| MR / MRS | High Resolution, Anatomical and Functional Information | Low Contrast Sensitivity, Long Scan Time, Low Temporal Resolution, Expensive | Yes* | Possible |
| Mass Spectrometry | High Sensitivity | Ex Vivo Only | Yes | Yes |
| CT / X ray | High Resolution, High Temporal Resolution | Very Low Contrast Sensitivity, Ionizing Radiation | Yes* | Possible |
| Ultrasound | Widely Available, High Temporal Resolution, Inexpensive | Lower Resolution, Contrast is Intravascular Only, Altered or Prevented by Tissue Type/Depth | No | No |
| Histology | High Resolution, Functional and Structural Information | Ex Vivo, Sample Preparation | Semi | Yes |

***** These modalities provide quantitative data, but calculation of exogenous agent concentration is usually semiquantitative

## 1.2.4a Nuclear and Radiolabel Detection and Imaging

The "gold standard" of pharmacokinetic and pharmacodynamic measurements is the use of radionuclide tracers. Radiolabeling provides absolute quantitation of tracer concentrations and very high (pM) sensitivity.[147] Although there are several mechanisms of nuclear decay (*e.g.* alpha, beta, gamma, positron emission, electron capture, isomeric transition, and internal conversion), radiotracer signals largely fall into two categories: gamma or beta emitters. Gamma radiation passes through soft tissue samples with little attenuation and can be quantified with minimal sample preparation using a gamma counting instrument. Beta particles, however, require indirect counting, which necessitates more sample preparation. Specifically, the sample is dissolved in a liquid scintillation solution, containing a scintillant that absorbs the beta particle's energy and emits light for detection.

The earliest experiments studying the *in vivo* biodistribution and clearance of nanoparticle formulations relied on radiolabeling. The long-lived radionuclides $^{3}H$, $^{14}C$, and $^{125}I$ were used to trace the activity of small molecule payloads incorporated into nanoparticles.[148-150] More recently, the γ emitters $^{111}In$ and $^{99m}Tc$ have gained popularity as nanoparticle radiolabels, since they have relatively mild labeling procedures and can be used for *in vivo* imaging (SPECT) followed by *ex vivo* measurements of biodistribution. For PET imaging of nanoparticle formulations, $^{64}Cu$ is most commonly used.

**Table 1.2.** Common Radionuclides for Nanoparticle Investigation

| Radionuclide | Decay Mode | Half Life |
|---|---|---|
| $^{1}H$ | β | 12.35 years |
| $^{14}C$ | β | 5730 years |
| $^{18}F$ | β+ | 109.77 minutes |
| $^{32}P$ | β | 25.4 days |
| $^{64}Cu$ | β+ | 12.7 hours |
| $^{99m}Tc$ | γ | 6.00 hours |
| $^{111}In$ | γ | 2.83 days |
| $^{125}I$ | γ | 60.14 days |
| $^{131}I$ | β | 8.02 days |

One major benefit of the metal radiotracers is the versatility available for incorporating the tracer into the nanoparticle formulation. Direct radiolabeling can be accomplished through reduction of disulfide bonds followed by introduction of the metal.[151, 152] More typically, a chelator (*e.g.* DTPA,[153, 154] HYN-IC,[155, 156] or DOTA[157]) is used to bind the metal. The chelator may be covalently conjugated to the surface of the nanoparticle, face the aqueous core,[158, 159] or be buried within a hydrophobic domain[160, 161] (*e.g.* bilayer of a liposome or core of a micelle). For vesicular structures such as liposomes and polyersomes, a preformed metal-chelator complex can be encapsulated within the aqueous core.[162, 163] It is possible to incorporate the chelator into the monomeric/block co-polymer material prior to nanoparticle assembly,[164] covalently conjugate the chelator to a previously assembled nanoparticle,[165] or non-covalently attach

a chelator functionalized moiety (*e.g*. protein or peptide) to the nanoparticle surface.[166] Addition of radiolabels to nanoparticles may have a minimal or significant impact on the agent's pharmacokinetics, depending on the location of the radiolabel within the nanoparticle (*i.e*. core versus surface) and the fractional increase in nanoparticle size upon radiolabeling.

The major limitation to radiolabeling, for the purposes of nanoparticle characterization, is the relative lack of multiplexing capability. A two-label ratiometric approach is well established using a low and high energy gamma emitter (*e.g*. $^{125}$I and $^{111}$In).[9, 167] A triplex assay is conceivable by adding a beta emitter detected separately by scintillation, but would then require separate preps and measurements to obtain the information. Higher order multiplexing (achievable by optical instrumentation *in vitro* or ICP-MS *ex vivo*) is unlikely to be feasible. Another, smaller consideration is the special handling requirements for radioactive material and animals. Laboratory handling of radionuclides is by no means "difficult"; but its inconvenience decreases the frequency of its use, and an alternative method of absolute quantification of nanoparticle concentration in biological samples, without radioactivity, may lead more investigators to acquire such data.

## 1.2.4b Optical and Fluorescence Detection and Imaging

Optical and fluorescence detection of nanoparticles is arguably the most convenient and widely used approach. Fluorescence is usually imparted to a nanoparticle by incorporation of either an organic dye or inorganic fluorophore (i.e. quantum dot). Many different small molecule organic fluorophores, spanning the visible and infrared spectrum, have been successfully used with nanoparticles, including: fluoresceins,

cyanines, rhodamines, and specific commercial dye lines like Alexa Fluor, DyLight, and BODIPY. The fluorophores can be incorporated by covalent conjugation or encapsulation within an aqueous or hydrophobic core. The labeled nanoparticles can then be imaged at the whole animal level or in *ex vivo* specimens. Multiplexing of fluorophores with resolvable excitation and emission spectra is possible, as evidenced by multi-color flow cytometry.[168] However, applying this principle at the tissue, organ, and animal level is more difficult since a large region of the visible spectrum is unsuitable for fluorescence measurements in complex or thick samples (see below).

Perhaps the biggest limitation of fluorescence detection and imaging of nanoparticles are issues associated with tissue penetration and interference. Specifically, both the incident excitation radiation and the emitted signal are subject to attenuation as they pass through biological tissue. Since light scattering decreases as $1/\lambda^4$ and photon absorption by endogenous oxygenated and deoxygenated hemoglobin reaches a minimum in the near infrared (NIR) spectral window,[169] tissue penetration is wavelength dependent – with longer wavelengths suffering less attenuation than shorter wavelengths. Nevertheless, even the brightest and most red-shifted organic fluorphores are limited to approximately 5 cm of tissue penetration.[170] This distance limit is suitable for small animal work, but is limiting for human applications other than those involving exposed tissue (*e.g.* superficial soft tissue and skin,[171] fluorescence assisited surgery,[172] or endoscopic methods).[173]

Another significant drawback of fluorescence detection of nanoparticles is its restriction to semi-quantitative measurements. That is, the concentration of the fluorophore, and therefore the nanoparticle, cannot be calculated from its signal, due to a

number interfering variables present in biological samples. For example, the peak excitation/emission wavelength, extinction coefficient, and quantum yield can vary with a number of parameters including local chemical environment, exposure time, and temperature. Fluorescence quenching, either from other molecules of the same fluorophore or endogenous absorbers, leads to significant non-linearity. Tissue thickness, density, composition, and auto-fluorescence also all influence signal, even with *ex vivo* sampling.

## 1.2.4c Magnetic Resonance Detection and Imaging

Magnetic resonance approaches are capable of obtaining an extremely diverse array of structural and functional information *in vivo* (see also the pH imaging section above). Generally speaking, the functional information is often extracted in one of three ways. First, in magnetic resonance spectroscopy (MRS) the chemical shift of a particular resonance may change with variations in some physiologic parameter. In this manner, the varying $^{31}$P resonance of 3-APP is used to deduce extracellular pH.[83] Secondly, alterations in the metabolic environment of tissues can be deduced using the ratio of the signals from two or more metabolites in an MRS study. For example, studies have found that a high choline / N-acetyl aspartate is commonly observed in brain tumors.[174] Thirdly, chemical exchange saturation transfer (CEST) measurements detect the transfer of magnetization between two pools in chemical exchange, leading to signal amplification, signals that can be "switched" on and off, and detection of physiologic stimuli by alterations they cause in the CEST effect.[175]

Measuring the absolute concentration of a particular resonance or metabolite with magnetic resonance methods is much more difficult, although significant progress has

been and continues to be made for endogenous metabolites.[176] With regard to determination of nanoparticle concentrations, however, absolute quantification is not yet possible. Since the concentration of nanoparticles delivered in vivo is not very large compared to the sensitivity of MR methods, direct detection of a nanoparticle's resonance is difficult. Instead, nanoparticles imaged by MR are usually detected indirectly through their interaction with bulk water protons. For example, $Gd^{3+}$ can be incorporated into nanoparticles with metal chelators, much the same as metal radionuclides can.[177] The gadolinium ion's seven unpaired electrons provide a conduit through which bulk water protons can transfer energy, allowing their longitudinal relaxation rate to be increased. This in turn leads to a stronger (brighter) signal on T1-weighted images for voxels containing the nanoparticle. SPIO nanoparticles contain iron oxide crystals, which generate disturbances in the local magnetic field surrounding the nanoparticles. This in turn causes accelerated de-phasing of the bulk water magnetization following a 90° radiofrequency pulse, which leads to a weaker (darker) signal on T2-weighted images. With SPIO or $Gd^{3+}$ doped nanoparticles, it is possible to estimate nanoparticle concentration using a calibration curve with a tissue phantom. However, accurate absolute quantification is difficult since many specific properties of the tissue and pulse sequence will influence the signal obtained. Furthermore, detection by this method is not amenable to multiplexing.

### 1.2.4d Inductively Coupled Plasma – Mass Spectrometry (ICP-MS) Detection

ICP-MS is an analytical method allowing for the rapid and sensitive (1 ppt to 1 ppb) detection of a wide range of metal species in a sample. The basic instrument design

places a mass spectrometer downstream of an inductively coupled plasma source. The ICP is generated by introducing a small number of electrons into an argon gas stream and then applying radiofrequency radiation to cause rapid oscillation of the free electrons. Collisions between the electrons and argon atoms result in ionization, producing $Ar^+$ and additional electrons. A steady state is quickly reached, resulting in electro-neutral plasma with a temperature significantly greater than a chemical flame.

In order to analyze a sample containing complex material, such as blood or tissue, the material must first be digested with nitric or hydrochloric acid to produce a more homogenous liquid. The sample is then nebulized and introduced into the plasma stream, where the extremely high temperature leads to atomization, and subsequent ionization, of the material. The metals ions of the sample are then fed from the plasma into a conventional mass spectrometer (usually quadrupole, or less frequently, time of flight). Importantly, the concentration of each metal ion being investigated can be simultaneously acquired with a single measurement.

ICP-MS multiplexing is already being successfully applied to *in vitro* immunoassays.[178] Specifically, a polymer tag containing multiple lanthanide metal chelates is attached to the Fc portion of antibodies.[179] In this manner, each specific antigen/antibody is associated with a specific lanthanide metal. *In vitro* multiplex analysis has been applied for a variety of cell surface biomarkers[180, 181] and growth and transcription factors in cell lysates.[178] Very recently (May 2011) the massively-parallel nature of ICP-MS multiplex analysis was demonstrated with simultaneous "mass cytometric" analysis of more than 30 cell markers.[182]

Another recent development in ICP-MS instrumentation is laser ablation LA-ICP-MS, which offers three considerable advantages over conventional ICP-MS. First, the original sample can be analyzed directly (*i.e.* without chemical digestion) by ablating the sample with a pulsed laser beam and sweeping the aerosol directly into the plasma. Secondly, LA-ICP-MS can be conducted with much smaller amounts of material. Specifically, micrograms samples can be analyzed, versus milligrams for conventional ICP-MS (*i.e*. the entire sample is microgram quantity; the amount of lanthanide need only be parts per billion concentration within the sample). Thirdly, the laser pulses can be scanned across a solid sample, allowing for a mass "image" to be generated for an organ or tumor with heterogeneously distributed nanoparticles.

## 1.3 References


1. Pautler, M.; Brenner, S., Nanomedicine: promises and challenges for the future of public health. *Int J Nanomedicine* 2010, 5, 803-9.

2. Li, Y.; Yao, Y.; Sheng, Z.; Yang, Y.; Ma, G., Dual-modal tracking of transplanted mesenchymal stem cells after myocardial infarction. *Int J Nanomedicine* 2011, 6, 815-23.

3. Feng, L.; Qi, X. R.; Zhou, X. J.; Maitani, Y.; Wang, S. C.; Jiang, Y.; Nagai, T., Pharmaceutical and immunological evaluation of a single-dose hepatitis B vaccine using PLGA microspheres. *J Control Release* 2006, 112, 35-42.

4. Sampietro, M.; Bottani, C. E.; Carminati, M.; Casari, C.; Castoldi, A.; Ferrari, G.; Fusi, M.; Guazzoni, C.; Rottigni, A.; Vergani, M., Biosensors and molecular imaging. *IEEE Pulse* 2011, 2, 35-40.

5. Winer, J. L.; Kim, P. E.; Law, M.; Liu, C. Y.; Apuzzo, M. L., Visualizing the future: enhancing neuroimaging with nanotechnology. *World Neurosurg* 2011, 75, 626-37; discussion 618-9.

6. Gobin, A. M.; O'Neal, D. P.; Watkins, D. M.; Halas, N. J.; Drezek, R. A.; West, J. L., Near infrared laser-tissue welding using nanoshells as an exogenous absorber. *Lasers Surg Med* 2005, 37, 123-9.

7. Cho, K.; Wang, X.; Nie, S.; Chen, Z. G.; Shin, D. M., Therapeutic nanoparticles for drug delivery in cancer. *Clin Cancer Res* 2008, 14, 1310-6.

8. Yoo, J. W.; Irvine, D. J.; Discher, D. E.; Mitragotri, S., Bio-inspired, bioengineered and biomimetic drug delivery carriers. *Nat Rev Drug Discov* 2011, 10, 521-35.

9. Muzykantov, V. R.; Puchnina, E. A.; Atochina, E. N.; Hiemish, H.; Slinkin, M. A.; Meertsuk, F. E.; Danilov, S. M., Endotoxin reduces specific pulmonary uptake of radiolabeled monoclonal antibody to angiotensin-converting enzyme. *J Nucl Med* 1991, 32, 453-60.

10. Cahouet, A.; Denizot, B.; Hindre, F.; Passirani, C.; Heurtault, B.; Moreau, M.; Le Jeune, J.; Benoit, J., Biodistribution of dual radiolabeled lipidic nanocapsules in the rat using scintigraphy and gamma counting. *Int J Pharm* 2002, 242, 367-71.

11. Maeda, H.; Wu, J.; Sawa, T.; Matsumura, Y.; Hori, K., Tumor vascular permeability and the EPR effect in macromolecular therapeutics: a review. *J Control Release* 2000, 65, 271-84.

12. Konerding, M. A.; Fait, E.; Gaumann, A., 3D microvascular architecture of pre-cancerous lesions and invasive carcinomas of the colon. *Br J Cancer* 2001, 84, 1354-62.

13. Peer, D.; Karp, J. M.; Hong, S.; Farokhzad, O. C.; Margalit, R.; Langer, R., Nanocarriers as an emerging platform for cancer therapy. *Nat Nanotechnol* 2007, 2, 751-60.

14. Moghimi, S. M.; Hunter, A. C.; Murray, J. C., Long-circulating and target-specific nanoparticles: theory to practice. *Pharmacol Rev* 2001, 53, 283-318.

15. Vonarbourg, A.; Passirani, C.; Saulnier, P.; Benoit, J. P., Parameters influencing the stealthiness of colloidal drug delivery systems. *Biomaterials* 2006, 27, 4356-73.

16. Huynh, N. T.; Roger, E.; Lautram, N.; Benoit, J. P.; Passirani, C., The rise and rise of stealth nanocarriers for cancer therapy: passive versus active targeting. *Nanomedicine (Lond)* 5, 1415-33.

17. McNeil, S. E., Nanotechnology for the biologist. *J Leukoc Biol* 2005, 78, 585-94.

18. Moghimi, S. M.; Davis, S. S., Innovations in avoiding particle clearance from blood by Kupffer cells: cause for reflection. *Crit Rev Ther Drug Carrier Syst* 1994, 11, 31-59.

19. Chouly, C.; Pouliquen, D.; Lucet, I.; Jeune, J. J.; Jallet, P., Development of superparamagnetic nanoparticles for MRI: effect of particle size, charge and surface nature on biodistribution. *J Microencapsul* 1996, 13, 245-55.

20. Lemarchand, C.; Gref, R.; Couvreur, P., Polysaccharide-decorated nanoparticles. *Eur J Pharm Biopharm* 2004, 58, 327-41.

21. Lemarchand, C.; Gref, R.; Passirani, C.; Garcion, E.; Petri, B.; Muller, R.; Costantini, D.; Couvreur, P., Influence of polysaccharide coating on the interactions of nanoparticles with biological systems. *Biomaterials* 2006, 27, 108-18.

22. Koo, O. M.; Rubinstein, I.; Onyuksel, H., Role of nanotechnology in targeted drug delivery and imaging: a concise review. *Nanomedicine* 2005, 1, 193-212.

23. Duncan, R., Polymer conjugates as anticancer nanomedicines. *Nat Rev Cancer* 2006, 6, 688-701.

24. Hong, R. L.; Huang, C. J.; Tseng, Y. L.; Pang, V. F.; Chen, S. T.; Liu, J. J.; Chang, F. H., Direct comparison of liposomal doxorubicin with or without polyethylene glycol coating in C-26 tumor-bearing mice: is surface coating with polyethylene glycol beneficial? *Clin Cancer Res* 1999, 5, 3645-52.

25. Byrne, J. D.; Betancourt, T.; Brannon-Peppas, L., Active targeting schemes for nanoparticle systems in cancer therapeutics. *Adv Drug Deliv Rev* 2008, 60, 1615-26.

26. Allen, T. M., Ligand-targeted therapeutics in anticancer therapy. *Nat Rev Cancer* 2002, 2, 750-63.

27. Jiang, W.; Kim, B. Y.; Rutka, J. T.; Chan, W. C., Nanoparticle-mediated cellular response is size-dependent. *Nat Nanotechnol* 2008, 3, 145-50.

28. Chiu, G. N.; Edwards, L. A.; Kapanen, A. I.; Malinen, M. M.; Dragowska, W. H.; Warburton, C.; Chikh, G. G.; Fang, K. Y.; Tan, S.; Sy, J.; Tucker, C.; Waterhouse, D. N.; Klasa, R.; Bally, M. B., Modulation of cancer cell survival pathways using multivalent liposomal therapeutic antibody constructs. *Mol Cancer Ther* 2007, 6, 844-55.

29. Gindy, M. E.; Ji, S.; Hoye, T. R.; Panagiotopoulos, A. Z.; Prud'homme, R. K., Preparation of poly(ethylene glycol) protected nanoparticles with variable bioconjugate ligand density. *Biomacromolecules* 2008, 9, 2705-11.

30. Wahl, R. L.; Zasadny, K.; Helvie, M.; Hutchins, G. D.; Weber, B.; Cody, R., Metabolic monitoring of breast cancer chemohormonotherapy using positron emission tomography: initial evaluation. *J Clin Oncol* 1993, 11, 2101-11.

31. Lamberts, S. W.; Bakker, W. H.; Reubi, J. C.; Krenning, E. P., Somatostatin-receptor imaging in the localization of endocrine tumors. *N Engl J Med* 1990, 323, 1246-9.

32. Press, O. W.; Eary, J. F.; Appelbaum, F. R.; Martin, P. J.; Badger, C. C.; Nelp, W. B.; Glenn, S.; Butchko, G.; Fisher, D.; Porter, B.; et al., Radiolabeled-antibody therapy of B-cell lymphoma with autologous bone marrow support. *N Engl J Med* 1993, 329, 1219-24.

33. Thorek, D. L.; Chen, A. K.; Czupryna, J.; Tsourkas, A., Superparamagnetic iron oxide nanoparticle probes for molecular imaging. *Ann Biomed Eng* 2006, 34, 23-38.

34. Konda, S. D.; Aref, M.; Wang, S.; Brechbiel, M.; Wiener, E. C., Specific targeting of folate-dendrimer MRI contrast agents to the high affinity folate receptor expressed in ovarian tumor xenografts. *MAGMA* 2001, 12, 104-13.

35. White, S.; Taetle, R.; Seligman, P. A.; Rutherford, M.; Trowbridge, I. S., Combinations of anti-transferrin receptor monoclonal antibodies inhibit human tumor cell growth in vitro and in vivo: evidence for synergistic antiproliferative effects. *Cancer Res* 1990, 50, 6295-301.

36. Yang, L.; Mao, H.; Wang, Y. A.; Cao, Z.; Peng, X.; Wang, X.; Duan, H.; Ni, C.; Yuan, Q.; Adams, G.; Smith, M. Q.; Wood, W. C.; Gao, X.; Nie, S., Single chain epidermal growth factor receptor antibody conjugated nanoparticles for in vivo tumor targeting and imaging. *Small* 2009, 5, 235-43.

37. Parenteau, G. L.; Dirbas, F. M.; Garmestani, K.; Brechbiel, M. W.; Bukowski, M. A.; Goldman, C. K.; Clark, R.; Gansow, O. A.; Waldmann, T. A., Prolongation of graft survival in primate allograft transplantation by yttrium-90-labeled anti-Tac in conjunction with granulocyte colony-stimulating factor. *Transplantation* 1992, 54, 963-8.

38. Zhang, C.; Jugold, M.; Woenne, E. C.; Lammers, T.; Morgenstern, B.; Mueller, M. M.; Zentgraf, H.; Bock, M.; Eisenhut, M.; Semmler, W.; Kiessling, F., Specific targeting of tumor angiogenesis by RGD-conjugated ultrasmall superparamagnetic iron oxide particles using a clinical 1.5-T magnetic resonance scanner. *Cancer Res* 2007, 67, 1555-62.

39. Boutry, S.; Laurent, S.; Elst, L. V.; Muller, R. N., Specific E-selectin targeting with a superparamagnetic MRI contrast agent. *Contrast Media Mol Imaging* 2006, 1, 15-22.

40. Schellenberger, E. A.; Bogdanov, A., Jr.; Hogemann, D.; Tait, J.; Weissleder, R.; Josephson, L., Annexin V-CLIO: a nanoparticle for detecting apoptosis by MRI. *Mol Imaging* 2002, 1, 102-7.

41. Neves, A. A.; Krishnan, A. S.; Kettunen, M. I.; Hu, D. E.; Backer, M. M.; Davletov, B.; Brindle, K. M., A paramagnetic nanoprobe to detect tumor cell death using magnetic resonance imaging. *Nano Lett* 2007, 7, 1419-23.

42. Freudenberg, J. A.; Wang, Q.; Katsumata, M.; Drebin, J.; Nagatomo, I.; Greene, M. I., The role of HER2 in early breast cancer metastasis and the origins of resistance to HER2-targeted therapies. *Exp Mol Pathol* 2009, 87, 1-11.

43. Ravdin, P. M.; Chamness, G. C., The c-erbB-2 proto-oncogene as a prognostic and predictive marker in breast cancer: a paradigm for the development of other macromolecular markers--a review. *Gene* 1995, 159, 19-27.

44. Slamon, D. J.; Clark, G. M.; Wong, S. G.; Levin, W. J.; Ullrich, A.; McGuire, W. L., Human breast cancer: correlation of relapse and survival with amplification of the HER-2/neu oncogene. *Science* 1987, 235, 177-82.

45. Berchuck, A.; Kamel, A.; Whitaker, R.; Kerns, B.; Olt, G.; Kinney, R.; Soper, J. T.; Dodge, R.; Clarke-Pearson, D. L.; Marks, P.; et al., Overexpression of HER-2/neu is associated with poor survival in advanced epithelial ovarian cancer. *Cancer Res* 1990, 50, 4087-91.

46. Fearon, E. R.; Vogelstein, B., A genetic model for colorectal tumorigenesis. *Cell* 1990, 61, 759-67.

47. Santin, A. D.; Bellone, S.; Roman, J. J.; McKenney, J. K.; Pecorelli, S., Trastuzumab treatment in patients with advanced or recurrent endometrial carcinoma overexpressing HER2/neu. *Int J Gynaecol Obstet* 2008, 102, 128-31.

48. Viani, G. A.; Afonso, S. L.; Stefano, E. J.; De Fendi, L. I.; Soares, F. V., Adjuvant trastuzumab in the treatment of her-2-positive early breast cancer: a meta-analysis of published randomized trials. *BMC Cancer* 2007, 7, 153.

49. Uhlen, M.; Guss, B.; Nilsson, B.; Gatenbeck, S.; Philipson, L.; Lindberg, M., Complete sequence of the staphylococcal gene encoding protein A. A gene evolved through multiple duplications. *J Biol Chem* 1984, 259, 1695-702.

50. Orlova, A.; Magnusson, M.; Eriksson, T. L.; Nilsson, M.; Larsson, B.; Hoiden-Guthenberg, I.; Widstrom, C.; Carlsson, J.; Tolmachev, V.; Stahl, S.; Nilsson, F. Y., Tumor imaging using a picomolar affinity HER2 binding affibody molecule. *Cancer Res* 2006, 66, 4339-48.

51. Nygren, P. A., Alternative binding proteins: affibody binding proteins developed from a small three-helix bundle scaffold. *FEBS J* 2008, 275, 2668-76.

52. Kinoshita, M.; Yoshioka, Y.; Okita, Y.; Hashimoto, N.; Yoshimine, T., MR molecular imaging of HER-2 in a murine tumor xenograft by SPIO labeling of anti-HER-2 affibody. *Contrast Media Mol Imaging* 5, 18-22.

53. Lee, S. B.; Hassan, M.; Fisher, R.; Chertov, O.; Chernomordik, V.; Kramer-Marek, G.; Gandjbakhche, A.; Capala, J., Affibody molecules for in vivo characterization of HER2-positive tumors by near-infrared imaging. *Clin Cancer Res* 2008, 14, 3840-9.

54. Kiesewetter, D. O.; Kramer-Marek, G.; Ma, Y.; Capala, J., Radiolabeling of HER2 specific Affibody(R) molecule with F-18. *J Fluor Chem* 2008, 129, 799-805.

55. Brooks, P. C.; Clark, R. A.; Cheresh, D. A., Requirement of vascular integrin alpha v beta 3 for angiogenesis. *Science* 1994, 264, 569-71.

56. Horton, M. A., The alpha v beta 3 integrin "vitronectin receptor". *Int J Biochem Cell Biol* 1997, 29, 721-5.

57. Hwang, R.; Varner, J., The role of integrins in tumor angiogenesis. *Hematol Oncol Clin North Am* 2004, 18, 991-1006, vii.

58. Folkman, J., Role of angiogenesis in tumor growth and metastasis. *Semin Oncol* 2002, 29, 15-8.

59. Sengupta, S.; Chattopadhyay, N.; Mitra, A.; Ray, S.; Dasgupta, S.; Chatterjee, A., Role of alphavbeta3 integrin receptors in breast tumor. *J Exp Clin Cancer Res* 2001, 20, 585-90.

60. Albelda, S. M.; Mette, S. A.; Elder, D. E.; Stewart, R.; Damjanovich, L.; Herlyn, M.; Buck, C. A., Integrin distribution in malignant melanoma: association of the beta 3 subunit with tumor progression. *Cancer Res* 1990, 50, 6757-64.

61. Bello, L.; Francolini, M.; Marthyn, P.; Zhang, J.; Carroll, R. S.; Nikas, D. C.; Strasser, J. F.; Villani, R.; Cheresh, D. A.; Black, P. M., Alpha(v)beta3 and alpha(v)beta5 integrin expression in glioma periphery. *Neurosurgery* 2001, 49, 380-9; discussion 390.

62. Felding-Habermann, B.; Mueller, B. M.; Romerdahl, C. A.; Cheresh, D. A., Involvement of integrin alpha V gene expression in human melanoma tumorigenicity. *J Clin Invest* 1992, 89, 2018-22.

63. Zitzmann, S.; Ehemann, V.; Schwab, M., Arginine-glycine-aspartic acid (RGD)-peptide binds to both tumor and tumor-endothelial cells in vivo. *Cancer Res* 2002, 62, 5139-43.

64. Harris, T. D.; Kalogeropoulos, S.; Nguyen, T.; Liu, S.; Bartis, J.; Ellars, C.; Edwards, S.; Onthank, D.; Silva, P.; Yalamanchili, P.; Robinson, S.; Lazewatsky, J.; Barrett, J.; Bozarth, J., Design, synthesis, and evaluation of radiolabeled integrin alpha v beta 3 receptor antagonists for tumor imaging and radiotherapy. *Cancer Biother Radiopharm* 2003, 18, 627-41.

65. Haubner, R.; Wester, H. J., Radiolabeled tracers for imaging of tumor angiogenesis and evaluation of anti-angiogenic therapies. *Curr Pharm Des* 2004, 10, 1439-55.

66. Haubner, R.; Wester, H. J.; Weber, W. A.; Mang, C.; Ziegler, S. I.; Goodman, S. L.; Senekowitsch-Schmidtke, R.; Kessler, H.; Schwaiger, M., Noninvasive imaging of alpha(v)beta3 integrin expression using 18F-labeled RGD-containing glycopeptide and positron emission tomography. *Cancer Res* 2001, 61, 1781-5.

67. Whisstock, J.; Skinner, R.; Lesk, A. M., An atlas of serpin conformations. *Trends Biochem Sci* 1998, 23, 63-7.

68. Morimoto, R. I.; Kline, M. P.; Bimston, D. N.; Cotto, J. J., The heat-shock response: regulation and function of heat-shock proteins and molecular chaperones. *Essays Biochem* 1997, 32, 17-29.

69. Nikitakis, N. G.; Rivera, H.; Lopes, M. A.; Siavash, H.; Reynolds, M. A.; Ord, R. A.; Sauk, J. J., Immunohistochemical expression of angiogenesis-related markers in oral squamous cell carcinomas with multiple metastatic lymph nodes. *Am J Clin Pathol* 2003, 119, 574-86.

70. Hirai, K.; Kikuchi, S.; Kurita, A.; Ohashi, S.; Adachi, E.; Matsuoka, Y.; Nagata, K.; Watanabe, M., Immunohistochemical distribution of heat shock protein 47 (HSP47) in scirrhous carcinoma of the stomach. *Anticancer Res* 2006, 26, 71-8.

71. Maitra, A.; Iacobuzio-Donahue, C.; Rahman, A.; Sohn, T. A.; Argani, P.; Meyer, R.; Yeo, C. J.; Cameron, J. L.; Goggins, M.; Kern, S. E.; Ashfaq, R.; Hruban, R. H.; Wilentz, R. E., Immunohistochemical validation of a novel epithelial and a novel stromal marker of

pancreatic ductal adenocarcinoma identified by global expression microarrays: sea urchin fascin homolog and heat shock protein 47. *Am J Clin Pathol* 2002, 118, 52-9.

72. Poschmann, G.; Sitek, B.; Sipos, B.; Ulrich, A.; Wiese, S.; Stephan, C.; Warscheid, B.; Kloppel, G.; Vander Borght, A.; Ramaekers, F. C.; Meyer, H. E.; Stuhler, K., Identification of proteomic differences between squamous cell carcinoma of the lung and bronchial epithelium. *Mol Cell Proteomics* 2009, 8, 1105-16.

73. Araki, K.; Mikami, T.; Yoshida, T.; Kikuchi, M.; Sato, Y.; Oh-ishi, M.; Kodera, Y.; Maeda, T.; Okayasu, I., High expression of HSP47 in ulcerative colitis-associated carcinomas: proteomic approach. *Br J Cancer* 2009, 101, 492-7.

74. Li, D.; Guang, W.; Abuzeid, W. M.; Roy, S.; Gao, G. P.; Sauk, J. J.; O'Malley, B. W., Jr., Novel adenoviral gene delivery system targeted against head and neck cancer. *Laryngoscope* 2008, 118, 650-8.

75. Newell, K.; Franchi, A.; Pouyssegur, J.; Tannock, I., Studies with glycolysis-deficient cells suggest that production of lactic acid is not the only cause of tumor acidity. *Proc Natl Acad Sci U S A* 1993, 90, 1127-31.

76. Schornack, P. A.; Gillies, R. J., Contributions of cell metabolism and H+ diffusion to the acidic pH of tumors. *Neoplasia* 2003, 5, 135-45.

77. Gillies, R. J.; Raghunand, N.; Karczmar, G. S.; Bhujwalla, Z. M., MRI of the tumor microenvironment. *J Magn Reson Imaging* 2002, 16, 430-50.

78. Raghunand, N.; Gatenby, R. A.; Gillies, R. J., Microenvironmental and cellular consequences of altered blood flow in tumours. *British Journal of Radiology* 2003, 76, S11-S22.

79. Martinez-Zaguilan, R.; Seftor, E. A.; Seftor, R. E.; Chu, Y. W.; Gillies, R. J.; Hendrix, M. J., Acidic pH enhances the invasive behavior of human melanoma cells. *Clin Exp Metastasis* 1996, 14, 176-86.

80. Schlappack, O. K.; Zimmermann, A.; Hill, R. P., Glucose starvation and acidosis: effect on experimental metastatic potential, DNA content and MTX resistance of murine tumour cells. *Br J Cancer* 1991, 64, 663-70.

81. Gillies, R. J.; Raghunand, N.; Garcia-Martin, M. L.; Gatenby, R. A., Ph Imaging. *Ieee Engineering in Medicine and Biology Magazine* 2004, 23, 57-64.

82. Stubbs, M.; Bhujwalla, Z. M.; Tozer, G. M.; Rodrigues, L. M.; Maxwell, R. J.; Morgan, R.; Howe, F. A.; Griffiths, J. R., An assessment of 31P MRS as a method of measuring pH in rat tumours. *NMR Biomed* 1992, 5, 351-9.

83. Gillies, R. J.; Liu, Z.; Bhujwalla, Z., 31P-MRS measurements of extracellular pH of tumors using 3-aminopropylphosphonate. *Am J Physiol* 1994, 267, C195-203.

84. McSheehy, P. M.; Seymour, M. T.; Ojugo, A. S.; Rodrigues, L. M.; Leach, M. O.; Judson, I. R.; Griffiths, J. R., A pharmacokinetic and pharmacodynamic study in vivo of human HT29 tumours using 19F and 31P magnetic resonance spectroscopy. *Eur J Cancer* 1997, 33, 2418-27.

85. Ojugo, A. S.; McSheehy, P. M.; McIntyre, D. J.; McCoy, C.; Stubbs, M.; Leach, M. O.; Judson, I. R.; Griffiths, J. R., Measurement of the extracellular pH of solid tumours in mice by magnetic resonance spectroscopy: a comparison of exogenous (19)F and (31)P probes. *NMR Biomed* 1999, 12, 495-504.

86. Bhujwalla, Z. M.; Artemov, D.; Ballesteros, P.; Cerdan, S.; Gillies, R. J.; Solaiyappan, M., Combined vascular and extracellular pH imaging of solid tumors. *NMR Biomed* 2002, 15, 114-9.

87. Garcia-Martin, M. L.; Herigault, G.; Remy, C.; Farion, R.; Ballesteros, P.; Coles, J. A.; Cerdan, S.; Ziegler, A., Mapping extracellular pH in rat brain gliomas in vivo by 1H magnetic resonance spectroscopic imaging: comparison with maps of metabolites. *Cancer Res* 2001, 61, 6524-31.

88. GIL, M. S.; Cruz, F.; Cerdan, S.; Ballesteros, P., Imidazol-1-Ylalkanoate Esters and Their Corresponding Acids - a Novel Series of Extrinsic H-1-Nmr Probes for Intracellular Ph. *Bioorganic & Medicinal Chemistry Letters* 1992, 2, 1717-1722.

89. van Sluis, R.; Bhujwalla, Z. M.; Raghunand, N.; Ballesteros, P.; Alvarez, J.; Cerdan, S.; Galons, J. P.; Gillies, R. J., In vivo imaging of extracellular pH using 1H MRSI. *Magn Reson Med* 1999, 41, 743-50.

90. Aime, S.; Barge, A.; Delli Castelli, D.; Fedeli, F.; Mortillaro, A.; Nielsen, F. U.; Terreno, E., Paramagnetic lanthanide(III) complexes as pH-sensitive chemical exchange saturation transfer (CEST) contrast agents for MRI applications. *Magn Reson Med* 2002, 47, 639-48.

91. Zhou, J.; Payen, J. F.; Wilson, D. A.; Traystman, R. J.; van Zijl, P. C., Using the amide proton signals of intracellular proteins and peptides to detect pH effects in MRI. *Nat Med* 2003, 9, 1085-90.

92. Aime, S.; Botta, M.; Geninatti Crich, S.; Giovenzana, G.; Palmisano, G.; Sisti, M., Novel paramagnetic macromolecular complexes derived from the linkage of a

macrocyclic Gd(III) complex to polyamino acids through a squaric acid moiety. *Bioconjug Chem* 1999, 10, 192-9.

93. Mikawa, M.; Miwa, N.; Brautigam, M.; Akaike, T.; Maruyama, A., Gd(3+)-loaded polyion complex for pH depiction with magnetic resonance imaging. *J Biomed Mater Res* 2000, 49, 390-5.

94. Zhang, S.; Wu, K.; Sherry, A. D., A Novel pH-Sensitive MRI Contrast Agent. *Angew Chem Int Ed Engl* 1999, 38, 3192-3194.

95. Gallagher, F. A.; Kettunen, M. I.; Day, S. E.; Hu, D. E.; Ardenkjaer-Larsen, J. H.; Zandt, R.; Jensen, P. R.; Karlsson, M.; Golman, K.; Lerche, M. H.; Brindle, K. M., Magnetic resonance imaging of pH in vivo using hyperpolarized 13C-labelled bicarbonate. *Nature* 2008, 453, 940-3.

96. Andreev, O. A.; Dupuy, A. D.; Segala, M.; Sandugu, S.; Serra, D. A.; Chichester, C. O.; Engelman, D. M.; Reshetnyak, Y. K., Mechanism and uses of a membrane peptide that targets tumors and other acidic tissues in vivo. *Proc Natl Acad Sci U S A* 2007, 104, 7893-8.

97. Reshetnyak, Y. K.; Andreev, O. A.; Segala, M.; Markin, V. S.; Engelman, D. M., Energetics of peptide (pHLIP) binding to and folding across a lipid bilayer membrane. *Proc Natl Acad Sci U S A* 2008, 105, 15340-5.

98. Reshetnyak, Y. K.; Segala, M.; Andreev, O. A.; Engelman, D. M., A monomeric membrane peptide that lives in three worlds: in solution, attached to, and inserted across lipid bilayers. *Biophys J* 2007, 93, 2363-72.

99. Segala, J.; Engelman, D. M.; Reshetnyak, Y. K.; Andreev, O. A., Accurate analysis of tumor margins using a fluorescent pH Low Insertion Peptide (pHLIP). *Int J Mol Sci* 2009, 10, 3478-87.

100. Vavere, A. L.; Biddlecombe, G. B.; Spees, W. M.; Garbow, J. R.; Wijesinghe, D.; Andreev, O. A.; Engelman, D. M.; Reshetnyak, Y. K.; Lewis, J. S., A novel technology for the imaging of acidic prostate tumors by positron emission tomography. *Cancer Res* 2009, 69, 4510-6.

101. Gao, G. H.; Im, G. H.; Kim, M. S.; Lee, J. W.; Yang, J.; Jeon, H.; Lee, J. H.; Lee, D. S., Magnetite-nanoparticle-encapsulated pH-responsive polymeric micelle as an MRI probe for detecting acidic pathologic areas. *Small* 2010, 6, 1201-4.

102. Gupta, A. K.; Gupta, M., Synthesis and surface engineering of iron oxide nanoparticles for biomedical applications. *Biomaterials* 2005, 26, 3995-4021.

103. Saini, S.; Stark, D. D.; Hahn, P. F.; Bousquet, J. C.; Introcasso, J.; Wittenberg, J.; Brady, T. J.; Ferrucci, J. T., Jr., Ferrite particles: a superparamagnetic MR contrast agent for enhanced detection of liver carcinoma. *Radiology* 1987, 162, 217-22.

104. Anzai, Y.; Blackwell, K. E.; Hirschowitz, S. L.; Rogers, J. W.; Sato, Y.; Yuh, W. T.; Runge, V. M.; Morris, M. R.; McLachlan, S. J.; Lufkin, R. B., Initial clinical experience with dextran-coated superparamagnetic iron oxide for detection of lymph node metastases in patients with head and neck cancer. *Radiology* 1994, 192, 709-15.

105. Will, O.; Purkayastha, S.; Chan, C.; Athanasiou, T.; Darzi, A. W.; Gedroyc, W.; Tekkis, P. P., Diagnostic precision of nanoparticle-enhanced MRI for lymph-node metastases: a meta-analysis. *Lancet Oncol* 2006, 7, 52-60.

106. Klerkx, W. M.; Bax, L.; Veldhuis, W. B.; Heintz, A. P.; Mali, W. P.; Peeters, P. H.; Moons, K. G., Detection of lymph node metastases by gadolinium-enhanced magnetic resonance imaging: systematic review and meta-analysis. *J Natl Cancer Inst* 102, 244-53.

107. Saksena, M. A.; Saokar, A.; Harisinghani, M. G., Lymphotropic nanoparticle enhanced MR imaging (LNMRI) technique for lymph node imaging. *Eur J Radiol* 2006, 58, 367-74.

108. Lee, J. H.; Huh, Y. M.; Jun, Y. W.; Seo, J. W.; Jang, J. T.; Song, H. T.; Kim, S.; Cho, E. J.; Yoon, H. G.; Suh, J. S.; Cheon, J., Artificially engineered magnetic nanoparticles for ultra-sensitive molecular imaging. *Nat Med* 2007, 13, 95-9.

109. Leung, K., Trastuzumab-manganese-doped iron oxide nanoparticles. 2004.

110. Gupta, K.; Maity, A.; Ghosh, U. C., Manganese associated nanoparticles agglomerate of iron(III) oxide: synthesis, characterization and arsenic(III) sorption behavior with mechanism. *J Hazard Mater* 184, 832-42.

111. Faure, C.; Meyre, M. E.; Trepout, S.; Lambert, O.; Lebraud, E., Magnetic multilamellar liposomes produced by in situ synthesis of iron oxide nanoparticles: "magnetonions". *J Phys Chem B* 2009, 113, 8552-9.

112. Amstad, E.; Kohlbrecher, J.; Muller, E.; Schweizer, T.; Textor, M.; Reimhult, E., Triggered release from liposomes through magnetic actuation of iron oxide nanoparticle containing membranes. *Nano Lett* 11, 1664-70.

113. Hickey, R. J.; Haynes, A. S.; Kikkawa, J. M.; Park, S. J., Controlling the self-assembly structure of magnetic nanoparticles and amphiphilic block-copolymers: from micelles to vesicles. *J Am Chem Soc* 133, 1517-25.

114. Simberg, D.; Duza, T.; Park, J. H.; Essler, M.; Pilch, J.; Zhang, L.; Derfus, A. M.; Yang, M.; Hoffman, R. M.; Bhatia, S.; Sailor, M. J.; Ruoslahti, E., Biomimetic amplification of nanoparticle homing to tumors. *Proc Natl Acad Sci U S A* 2007, 104, 932-6.

115. Bremer, C.; Tung, C. H.; Weissleder, R., Molecular imaging of MMP expression and therapeutic MMP inhibition. *Acad Radiol* 2002, 9 Suppl 2, S314-5.

116. Nahrendorf, M.; Sosnovik, D.; Chen, J. W.; Panizzi, P.; Figueiredo, J. L.; Aikawa, E.; Libby, P.; Swirski, F. K.; Weissleder, R., Activatable magnetic resonance imaging agent reports myeloperoxidase activity in healing infarcts and noninvasively detects the antiinflammatory effects of atorvastatin on ischemia-reperfusion injury. *Circulation* 2008, 117, 1153-60.

117. Awasthi, V. D.; Garcia, D.; Goins, B. A.; Phillips, W. T., Circulation and biodistribution profiles of long-circulating PEG-liposomes of various sizes in rabbits. *International Journal of Pharmaceutics* 2003, 253, 121-132.

118. Chonn, A.; Cullis, P. R., Recent advances in liposome technologies and their applications for systemic gene delivery. *Advanced Drug Delivery Reviews* 1998, 30, 73-83.

119. Kirby, C.; Clarke, J.; Gregoriadis, G., Effect of the cholesterol content of small unilamellar liposomes on their stability in vivo and in vitro. *Biochem J* 1980, 186, 591-8.

120. Levine, D. H.; Ghoroghchian, P. P.; Freudenberg, J.; Zhang, G.; Therien, M. J.; Greene, M. I.; Hammer, D. A.; Murali, R., Polymersomes: A new multi-functional tool for cancer diagnosis and therapy. *Methods* 2008, 46, 25-32.

121. Discher, B. M.; Won, Y. Y.; Ege, D. S.; Lee, J. C. M.; Bates, F. S.; Discher, D. E.; Hammer, D. A., Polymersomes: Tough vesicles made from diblock copolymers. *Science* 1999, 284, 1143-1146.

122. Mody, V. V.; Nounou, M. I.; Bikram, M., Novel nanomedicine-based MRI contrast agents for gynecological malignancies. *Advanced Drug Delivery Reviews* 2009, 61, 795-807.

123. Harasym, T. O.; Bally, M. B.; Tardi, P., Clearance properties of liposomes involving conjugated proteins for targeting. *Advanced Drug Delivery Reviews* 1998, 32, 99-118.

124. Nallamothu, R.; Wood, G. C.; Pattillo, C. B.; Scott, R. C.; Kiani, M. F.; Moore, B. M.; Thoma, L. A., A tumor vasculature targeted liposome delivery system for combretastatin A4: design, characterization, and in vitro evaluation. *AAPS PharmSciTech* 2006, 7, E32.

125. Discher, D. E.; Ahmed, F., Polymersomes. *Annual Review of Biomedical Engineering* 2006, 8, 323-341.

126. Gorman, C. B.; Smith, J. C., Structure-property relationships in dendritic encapsulation. *Accounts Chem. Res.* 2001, 34, 60-71.

127. Brocorens, P.; Lazzaroni, R.; Bredas, J. L., Molecular modeling simulations of the morphology of polyphenylene dendrimers. *J. Phys. Chem. B* 2007, 111, 9218-9227.

128. Xu, H.; Regino, C. A. S.; Koyama, Y.; Hama, Y.; Gunn, A. J.; Bernardo, M.; Kobayashi, H.; Choyke, P. L.; Brechbiel, M. W., Preparation and preliminary evaluation of a biotin-targeted, lectin-targeted dendrimer-based probe for dual-modality magnetic resonance and fluorescence Imaging. *Bioconjugate Chemistry* 2007, 18, 1474-1482.

129. Xu, R. Z.; Wang, Y. L.; Wang, X. L.; Jeong, E. K.; Parker, D. L.; Lu, Z. R., In vivo evaluation of a PAMAM-Cystamine-(Gd-DO3A) conjugate as a biodegradable macromolecular MRI contrast agent. *Experimental Biology and Medicine* 2007, 232, 1081-1089.

130. Zhu, W. L.; Mollie, B.; Bhujwalla, Z. M.; Artemov, D., PAMAM dendrimer-based contrast agents for MR imaging of Her-2/neu receptors by a three-step pretargeting approach. *Magnetic Resonance in Medicine* 2008, 59, 679-685.

131. Boswell, C. A.; Eck, P. K.; Regino, C. A. S.; Bernardo, M.; Wong, K. J.; Milenic, D. E.; Choyke, P. L.; Brechbiel, M. W., Synthesis, characterization, and biological evaluation of integrin alpha(v)beta(3)-targeted PAMAM dendrimers. *Molecular Pharmaceutics* 2008, 5, 527-539.

132. Cheng, Y. Y.; Qu, H.; Ma, M. L.; Xu, Z. H.; Xu, P.; Fang, Y. J.; Xu, T. W., Polyamidoamine (PAMAM) dendrimers as biocompatible carriers of quinolone antimicrobials: An in vitro study. *European Journal of Medicinal Chemistry* 2007, 42, 1032-1038.

133. Svenson, S., Dendrimers as versatile platform in drug delivery applications. *Eur J Pharm Biopharm* 2009, 71, 445-62.

134. Boyd, B. J.; Kaminskas, L. M.; Karellas, P.; Krippner, G.; Lessene, R.; Porter, C. J. H., Cationic poly-L-lysine dendrimers: Pharmacokinetics, biodistribution, and evidence for metabolism and bioresorption after intravenous administration to rats. *Molecular Pharmaceutics* 2006, 3, 614-627.

135. Duncan, R.; Izzo, L., Dendrimer biocompatibility and toxicity. *Advanced Drug Delivery Reviews* 2005, 57, 2215-2237.

136. Faulk, W. P.; Taylor, G. M., Immunocolloid Method for Electron Microscope. *Immunochemistry* 1971, 8, 1081-&.

137. Sperling, R. A.; Pellegrino, T.; Li, J. K.; Chang, W. H.; Parak, W. J., Electrophoretic separation of nanoparticles with a discrete number of functional groups. *Advanced Functional Materials* 2006, 16, 943-948.

138. Zanchet, D.; Micheel, C. M.; Parak, W. J.; Gerion, D.; Alivisatos, A. P., Electrophoretic isolation of discrete Au nanocrystal/DNA conjugates. *Nano Letters* 2001, 1, 32-35.

139. Martin, B. R.; Dermody, D. J.; Reiss, B. D.; Fang, M. M.; Lyon, L. A.; Natan, M. J.; Mallouk, T. E., Orthogonal self-assembly on colloidal gold-platinum nanorods. *Advanced Materials* 1999, 11, 1021-1025.

140. Schonenberger, C.; vanderZande, B. M. I.; Fokkink, L. G. J.; Henny, M.; Schmid, C.; Kruger, M.; Bachtold, A.; Huber, R.; Birk, H.; Staufer, U., Template synthesis of nanowires in porous polycarbonate membranes: Electrochemistry and morphology. *Journal of Physical Chemistry B* 1997, 101, 5497-5505.

141. Huang, C.; Chiu, P.; Wang, Y.; Meen, T.; Yang, C., Synthesis and characterization of gold nanodogdones by the seeded mediated growth method. *Nanotechnology* 2007, 18, 395602.

142. Kalele, S.; Gosavi, S. W.; Urban, J.; Kulkarni, S. K., Nanoshell particles: synthesis, properties and applications. *Current Science* 2006, 91, 1038-1052.

143. Qian, X. M.; Peng, X. H.; Ansari, D. O.; Yin-Goen, Q.; Chen, G. Z.; Shin, D. M.; Yang, L.; Young, A. N.; Wang, M. D.; Nie, S. M., In vivo tumor targeting and spectroscopic detection with surface-enhanced Raman nanoparticle tags. *Nature Biotechnology* 2008, 26, 83-90.

144. Hainfeld, J. F.; Slatkin, D. N.; Focella, T. M.; Smilowitz, H. M., Gold nanoparticles: a new X-ray contrast agent. *British Journal of Radiology* 2006, 79, 248-253.

145. Didychuk, C. L.; Ephrat, P.; Chamson-Reig, A.; Jacques, S. L.; Carson, J. J. L., Depth of photothermal conversion of gold nanorods embedded in a tissue-like phantom. *Nanotechnology* 2009, 20, -.

146. Huang, X.; Qian, W.; El-Sayed, I. H.; El-Sayed, M. A., The potential use of the enhanced nonlinear properties of gold nanospheres in photothermal cancer therapy. *Lasers in Surgery and Medicine* 2007, 39, 747-753.

147. Li, Z.; Conti, P. S., Radiopharmaceutical chemistry for positron emission tomography. *Adv Drug Deliv Rev* 2010, 62, 1031-51.

148. Kimelberg, H. K.; Tracy, T. F., Jr.; Biddlecome, S. M.; Bourke, R. S., The effect of entrapment in liposomes on the in vivo distribution of [3H]methotrexate in a primate. *Cancer Res* 1976, 36, 2949-57.

149. Seymour, L. W.; Duncan, R.; Strohalm, J.; Kopecek, J., Effect of molecular weight (Mw) of N-(2-hydroxypropyl)methacrylamide copolymers on body distribution and rate of excretion after subcutaneous, intraperitoneal, and intravenous administration to rats. *J Biomed Mater Res* 1987, 21, 1341-58.

150. Sjoholm, I.; Edman, P., Acrylic microspheres in vivo. I. Distribution and elimination of polyacrylamide microparticles after intravenous and intraperitoneal injection in mouse and rat. *J Pharmacol Exp Ther* 1979, 211, 656-62.

151. Banerjee, T.; Singh, A. K.; Sharma, R. K.; Maitra, A. N., Labeling efficiency and biodistribution of Technetium-99m labeled nanoparticles: interference by colloidal tin oxide particles. *Int J Pharm* 2005, 289, 189-95.

152. Reddy, L. H.; Sharma, R. K.; Chuttani, K.; Mishra, A. K.; Murthy, R. R., Etoposide-incorporated tripalmitin nanoparticles with different surface charge: formulation, characterization, radiolabeling, and biodistribution studies. *AAPS J* 2004, 6, e23.

153. Kommareddy, S.; Amiji, M., Biodistribution and pharmacokinetic analysis of long-circulating thiolated gelatin nanoparticles following systemic administration in breast cancer-bearing mice. *J Pharm Sci* 2007, 96, 397-407.

154. Weissleder, R.; Lee, A. S.; Fischman, A. J.; Reimer, P.; Shen, T.; Wilkinson, R.; Callahan, R. J.; Brady, T. J., Polyclonal human immunoglobulin G labeled with polymeric iron oxide: antibody MR imaging. *Radiology* 1991, 181, 245-9.

155. Laverman, P.; Carstens, M. G.; Storm, G.; Moghimi, S. M., Recognition and clearance of methoxypoly(ethyleneglycol)2000-grafted liposomes by macrophages with enhanced phagocytic capacity. Implications in experimental and clinical oncology. *Biochim Biophys Acta* 2001, 1526, 227-9.

156. Laverman, P.; Dams, E. T.; Oyen, W. J.; Storm, G.; Koenders, E. B.; Prevost, R.; van der Meer, J. W.; Corstens, F. H.; Boerman, O. C., A novel method to label liposomes with 99mTc by the hydrazino nicotinyl derivative. *J Nucl Med* 1999, 40, 192-7.

157. Pressly, E. D.; Rossin, R.; Hagooly, A.; Fukukawa, K.; Messmore, B. W.; Welch, M. J.; Wooley, K. L.; Lamm, M. S.; Hule, R. A.; Pochan, D. J.; Hawker, C. J., Structural effects on the biodistribution and positron emission tomography (PET) imaging of well-defined (64)Cu-labeled nanoparticles comprised of amphiphilic block graft copolymers. *Biomacromolecules* 2007, 8, 3126-34.

158. Harrington, K. J.; Mohammadtaghi, S.; Uster, P. S.; Glass, D.; Peters, A. M.; Vile, R. G.; Stewart, J. S., Effective targeting of solid tumors in patients with locally advanced cancers by radiolabeled pegylated liposomes. *Clin Cancer Res* 2001, 7, 243-54.

159. Laverman, P.; Boerman, O. C.; Oyen, W. J.; Dams, E. T.; Storm, G.; Corstens, F. H., Liposomes for scintigraphic detection of infection and inflammation. *Adv Drug Deliv Rev* 1999, 37, 225-235.

160. Gref, R.; Minamitake, Y.; Peracchia, M. T.; Trubetskoy, V.; Torchilin, V.; Langer, R., Biodegradable long-circulating polymeric nanospheres. *Science* 1994, 263, 1600-3.

161. Jestin, E.; Mougin-Degraef, M.; Faivre-Chauvet, A.; Remaud-Le Saec, P.; Hindre, F.; Benoit, J. P.; Chatal, J. F.; Barbet, J.; Gestin, J. F., Radiolabeling and targeting of lipidic nanocapsules for applications in radioimmunotherapy. *Q J Nucl Med Mol Imaging* 2007, 51, 51-60.

162. Ballot, S.; Noiret, N.; Hindre, F.; Denizot, B.; Garin, E.; Rajerison, H.; Benoit, J. P., 99mTc/188Re-labelled lipid nanocapsules as promising radiotracers for imaging and therapy: formulation and biodistribution. *Eur J Nucl Med Mol Imaging* 2006, 33, 602-7.

163. Bao, A.; Goins, B.; Klipper, R.; Negrete, G.; Phillips, W. T., 186Re-liposome labeling using 186Re-SNS/S complexes: in vitro stability, imaging, and biodistribution in rats. *J Nucl Med* 2003, 44, 1992-9.

164. Sun, G.; Xu, J.; Hagooly, A.; Rossin, R.; Li, Z.; Moore, D. A., Strategies for optimized radiolabeling of nanoparticles for in vivo PET imaging. *Adv Mater* 2007, 19, 3157-62.

165. Xu, J.; Sun, G.; Rossin, R.; Hagooly, A.; Li, Z.; Fukukawa, K. I.; Messmore, B. W.; Moore, D. A.; Welch, M. J.; Hawker, C. J.; Wooley, K. L., Labeling of Polymer Nanostructures for Medical Imaging: Importance of crosslinking extent, spacer length, and charge density. *Macromolecules* 2007, 40, 2971-2973.

166. Rossin, R.; Muro, S.; Welch, M. J.; Muzykantov, V. R.; Schuster, D. P., In vivo imaging of 64Cu-labeled polymer nanoparticles targeted to the lung endothelium. *J Nucl Med* 2008, 49, 103-11.

167. Tai, J. H.; Nguyen, B.; Wells, R. G.; Kovacs, M. S.; McGirr, R.; Prato, F. S.; Morgan, T. G.; Dhanvantari, S., Imaging of gene expression in live pancreatic islet cell lines using dual-isotope SPECT. *J Nucl Med* 2008, 49, 94-102.

168. Baumgarth, N.; Roederer, M., A practical approach to multicolor flow cytometry for immunophenotyping. *J Immunol Methods* 2000, 243, 77-97.

169. Weissleder, R., A clearer vision for in vivo imaging. *Nat Biotechnol* 2001, 19, 316-7.

170. Weissleder, R.; Ntziachristos, V., Shedding light onto live molecular targets. *Nat Med* 2003, 9, 123-8.

171. Zhao, B.; He, Y. Y., Recent advances in the prevention and treatment of skin cancer using photodynamic therapy. *Expert Rev Anticancer Ther* 2010, 10, 1797-809.

172. Gioux, S.; Choi, H. S.; Frangioni, J. V., Image-guided surgery using invisible near-infrared light: fundamentals of clinical translation. *Mol Imaging* 2010, 9, 237-55.

173. Wang, T. D.; Van Dam, J., Optical biopsy: a new frontier in endoscopic detection and diagnosis. *Clin Gastroenterol Hepatol* 2004, 2, 744-53.

174. Horska, A.; Barker, P. B., Imaging of brain tumors: MR spectroscopy and metabolic imaging. *Neuroimaging Clin N Am* 2010, 20, 293-310.

175. Sherry, A. D.; Woods, M., Chemical exchange saturation transfer contrast agents for magnetic resonance imaging. *Annu Rev Biomed Eng* 2008, 10, 391-411.

176. Jansen, J. F.; Backes, W. H.; Nicolay, K.; Kooi, M. E., 1H MR spectroscopy of the brain: absolute quantification of metabolites. *Radiology* 2006, 240, 318-32.

177. Cheng, Z.; Thorek, D. L.; Tsourkas, A., Gadolinium-conjugated dendrimer nanoclusters as a tumor-targeted T1 magnetic resonance imaging contrast agent. *Angew Chem Int Ed Engl* 2010, 49, 346-50.

178. Razumienko, E.; Ornatsky, O.; Kinach, R.; Milyavsky, M.; Lechman, E.; Baranov, V.; Winnik, M. A.; Tanner, S. D., Element-tagged immunoassay with ICP-MS detection: evaluation and comparison to conventional immunoassays. *J Immunol Methods* 2008, 336, 56-63.

179. Lou, X.; Zhang, G.; Herrera, I.; Kinach, R.; Ornatsky, O.; Baranov, V.; Nitz, M.; Winnik, M. A., Polymer-based elemental tags for sensitive bioassays. *Angew Chem Int Ed Engl* 2007, 46, 6111-4.

180. Ornatsky, O.; Baranov, V. I.; Bandura, D. R.; Tanner, S. D.; Dick, J., Multiple cellular antigen detection by ICP-MS. *J Immunol Methods* 2006, 308, 68-76.

181. Tanner, S. D.; Ornatsky, O.; Bandura, D. R.; Baranov, V., Multiplex bio-assay with inductively coupled plasma mass spectrometry: towards a massively multivariate single-cell technology. *Spectrochim Acta, Part B: Atom Spectrosc* 2007, 62, 188.

182. Bendall, S. C.; Simonds, E. F.; Qiu, P.; Amir el, A. D.; Krutzik, P. O.; Finck, R.; Bruggner, R. V.; Melamed, R.; Trejo, A.; Ornatsky, O. I.; Balderas, R. S.; Plevritis, S. K.; Sachs, K.; Pe'er, D.; Tanner, S. D.; Nolan, G. P., Single-cell mass cytometry of differential immune and drug responses across a human hematopoietic continuum. *Science* 2011, 332, 687-96.

# Chapter 2: Development of ICP-MS Analytical Method to Quantify SPIO Nanoparticle Clearance and Organ Concentration

## 2.1 Abstract

Recent advances in material science and chemistry have led to the development of nanoparticles with diverse physicochemical properties, e.g. size, charge, shape, and surface chemistry. Evaluating which physicochemical properties are best for imaging and therapeutic studies is challenging not only because of the multitude of samples to evaluate, but also because of the large experimental variability associated with *in vivo* studies (e.g. differences in tumor size, injected dose, subject weight, etc.). To address this issue, we have developed a novel lanthanide-doped nanoparticle system and analytical method that allows for the quantitative comparison of multiple nanoparticle compositions simultaneously. Specifically, SPIO with a range of different sizes and charges were synthesized, each with a unique lanthanide dopant. Following the simultaneous injection of the various SPIO compositions into tumor-bearing mice, inductively coupled plasma mass spectroscopy (ICP-MS) was used to quantitatively and orthogonally assess the concentration of each specific SPIO composition in serial blood samples and the resected tumor and organs. This approach provides a simple, cost-effective, and non-radiative method to quantitatively compare tumor localization, biodistribution, and blood clearance of more than 10 nanoparticle compositions simultaneously, removing subject-to-subject variability.

## 2.2. Introduction

Over the past decade, interest in the development of nanoparticles for clinical applications, such as diagnosis and drug delivery, has increased exponentially, along with the number of specific nanoparticle formulations reported in the literature.[1-5] Given the variety of nanomaterials from which they can be constructed, the array of physicochemical properties they can possess, and the assortment of specific molecular processes that can be targeted *in vivo*, the number of potential nanoparticle combinations is truly astronomical.

For most nanoparticle applications, a crucial research question is how much of the nanoparticle formulation (and thus imaging or therapeutic payload) reaches the tissue of interest. However, since determining this information directly and quantitatively is often impractical, indirect or semi-quantitative methods are usually employed. For example, relative nanoparticle delivery may be inferred from fluorescence intensity, imaging contrast, or alterations in tumor growth rate. However, since nanoparticle delivery is only one of several variables affecting fluorescence intensity, imaging contrast, and tumor growth rate, they cannot be assumed to represent nanoparticle delivery.

The “gold standard” for quantitative determination of biodistribution and blood clearance is through incorporation of a radioisotope within the compound of interest. Given the large number of radioisotopes to choose from, a compound can usually be radiolabeled by replacement of a stable isotope, ensuring the label has minimal impact on the behavior of the compound. Radiolabeling also has the advantage of being very sensitive. However, one major drawback to the use of radiolabeling is the special handling and containment protocols required when working with radioactivity. Therefore,

a quantitative approach that does not require special laboratory precautions could make measurements of clearance and biodistribution more accessible.

Another, perhaps even more important, research question is how does one nanoparticle's delivery to a tissue of interest compare to another's. Whether comparing a new investigational agent to a negative control or optimizing a specific set of nanoparticles, such data are indispensable for development of better nanoparticle formulations and progression to clinical use. Beyond the difficulties of obtaining quantitative data for an individual nanoparticle's biodistribution, there are also problems using this data to compare nanoparticle formulations due to the large experimental variability of *in vivo* studies. A convenient way to compare agents while controlling for subject-to-subject variability is to employ a ratiometric or multiplex approach, whereby two or more agents are administered simultaneously to a single subject, and a "signal" from each one can be independently resolved. It is possible to employ a multiplex approach with radiolabeling, using gamma emitters with resolvable energies[6] or a combination of gamma counting and scintillation,[7] but physical limitations of energy resolution ultimately limit the number of compounds that can be simultaneously investigated.

In order to address these limitations, a method was designed that would allow for the quantitative determination of biodistribution and blood clearance of multiple nanoparticle formulations in a single animal (Figure 2.1). Specifically, lanthanide metals were doped into the iron cores of superparamagnetic iron oxide (SPIO) nanoparticless. Multiple lanthanide-labeled nanoparticles were then injected in individual animals simultaneously. Inductively coupled mass spectrometry (ICP-MS) was then used to

detect parts-per-billion (ppb) concentrations of the lanthanide metals, independent of one another, in tissue and blood. Since lanthanide and other heavy metals (e.g. gold, silver, etc.) do not naturally exist within animal subjects, the concentration of the lanthanide metals unambiguously represents the concentration of its associated nanoparticle. This "ICP-MS multiplex" approach should provide a sensitive and straightforward method for quantitatively comparing the biodistribution and blood clearance of multiple nanoparticle formulations simultaneously, without the disadvantages of radioactivity and subject-to-subject variability.

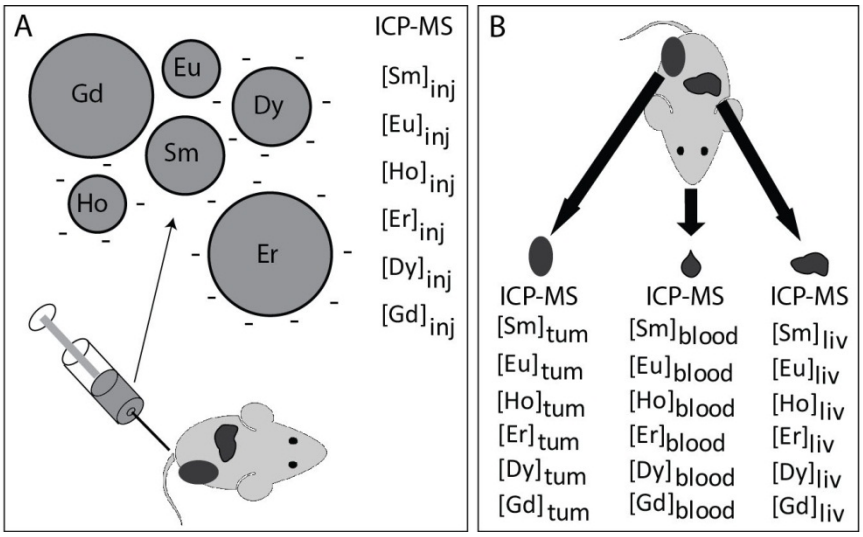


**Figure 2.1** Schematic of the ICP-MS based multiplex method for determining biodistribution and blood clearance. (A) Nanoparticles of varying physicochemical properties are combined into a single solution. Each type of nanoparticle is associated with a unique lanthanide metal; either by encapsulation or chelation (for example, the large and neutral particle contains Gd while the small and negative particle contains Ho). The concentration of each lanthanide metal in the injected solution is measured by ICP-MS and the combined solution is injected intravenously into the animal. (B) Blood samples are drawn at various times post-injection and following the final blood draw, the animal is sacrificed and the tumor and other organs are excised and rinsed in water. The blood and tissue samples are weighed and digested with nitric acid, and then the concentration of each lanthanide metal is determined by ICP-MS.

## 2.3 Materials and Methods

*Synthesis of Dextran Stabilized Lanthanide Doped SPIO*

Dextran coated, lanthanide doped, SPIO nanoparticles were prepared though the coprecipitation of ferrous, ferric, and lanthanide ions in the presence of dextran. [8] Briefly, 25 g of dextran T-10 (Pharmacosmos A/S, Holbaek, Denmark), was dissolved in 500 mL $dH_2O$ and heated to 80°C for 1 hour. The solution was then allowed to cool to room temperature and continued to mix overnight. Subsequently, a solution of 1.85 g $FeCl_3$, 0.73 g $FeCl_2$, and 0.125 g $LnCl_3 \bullet 6H_2O$ (Ln = Ho, Eu, Er, Sm, or Gd) in 25 mL $dH_2O$ was prepared and decanted into the dextran solution. The combined solution was cooled on ice and degassed with $N_2$ for 90 min. While keeping the solution stirring on ice and under $N_2$, an automated syringe pump was then used to introduce 15 mL of concentrated $NH_4OH$ to the solution over 5 hours. The resulting black viscous solution was removed from the $N_2$ atmosphere, heated to 90°C for 1 hour, cooled overnight, and centrifuged at 20,000 RCF for 30 minutes to remove large aggregates. Free iron, lanthanide, and dextran were removed by diafilitration across a 100 kDa membrane and the Ln-SPIO were brought to a final volume of ≈40 mL at 10 mg Fe/mL.

This 40 mL of dextran SPIO at an iron concentration of 10 mg/mL was then combined with an equal volume of 10 M NaOH and mixed for 10 minutes. 80 mL of epichlorohydrin was then added and the solution was vigorously stirred at room temperature overnight. Epichlorohydrin crosslinks the dextran coating within the Ln-SPIO particle and chemically activates the dextran surface for conjugation. The solution was then briefly centrifuged to allow phase-separation into an aqueous black SPIO layer and a clear layer of unreacted epichlorohydrin, which was removed. The SPIO layer was

quickly purified via extraction in isopropanol. Specifically, the Ln-SPIO material was combined with 5 volumes of isopropanol and the mixture was vigorously shaken. Brief centrifugation of the mixture resulted in a layer of precipitated salt, an Ln-SPIO layer, and an isopropanol layer (containing any remaining epichlorohydrin). The SPIO layer was then isolated and combined with an equal volume of concentrated $NH_4OH$ and gently stirred for 24 hours at room temperature, resulting in an aminated nanoparticle surface. After the reaction, the Ln-SPIO was purified by diafiltration across a 100 kDa membrane and was 0.2 μm filtered to remove any oversized material. Finally, to ensure complete purification of the Ln-SPIO from excess salt and lanthanide ions, the nanoparticles were magnetically purified on MACS LS columns using a MidiMACS magnet (Miltenyi Biotec, Auburn, CA, USA).

To prepare SPIO with different surface charges, aminated Ln-SPIO formulations were reacted overnight with varying amounts of succinic anhydride (0 – 1 M) in 0.1 M sodium bicarbonate buffer and subsequently purified by isopropanol precipitation. Nanoparticles with distinct size distributions were obtained by differential centrifugation. Specifically, iterative centrifugation at 10,000 RCF for 10 minutes, resulted in a final nanoparticle pellet enriched for larger sizes. Smaller nanoparticles were obtained by magnetic depletion (i.e. the flow-through of a MACS LS column was collected). Necessarily, this resulted in SPIO without magnetic properties, but selected for smaller nanoparticles, since particularly small iron cores do not have magnetic properties.

*Nanoparticle Physicochemical Characterization*

Ln-SPIO stock samples were diluted in deionized water and deposited on 200-mesh carbon coated copper grids (Polysciences, Warrington, PA, USA) for TEM imaging with a JEOL 1010 transmission electron microscope operating at 80 kV. Mean iron core size was determined by measuring 100 individual nanoparticles. The presence of lanthanide metal incorporated into SPIO nanoparticles, versus the background solution, was assessed by energy dispersive X-ray spectroscopy (EDS) mapping using a JEOL 2010F. Stock samples of Ln-SPIO nanoparticles, dendrimers, polymersomes, and liposomes were diluted into pH 7.4 phosphate buffered saline for determination of the hydrodynamic diameter by dynamic light scattering (DLS). Measurements were acquired with a Zetasizer Nano-ZS (Malvern Instruments, Worcestershire, UK) using the non-invasive back-scatter (NIBS) mode. For zeta potential measurements, stock samples of Ln-SPIO were diluted into either 10 mM HEPES buffered water at pH 7.4 or phosphate buffered saline at pH 7.4 and then mean nanoparticle zeta potential was measured using a Zetasizer Nano-ZS. For Ln-SPIO nanoparticles, the transverse ($r_2$) and longitudinal ($r_1$) relaxivities were measured using a Bruker mq60 tabletop MR relaxometer operating at 1.41 T (60 MHz).

*Nanoparticle Stability Assays*

The stability of the nanoparticles was measured as the amount of lanthanide leakage that could be observed in serum. Nanoparticles were incubated in 100% fetal bovine serum (FBS) at 37°C with shaking. Aliquots were removed at 1, 2, 4, 6, and 24 hours and applied to a 4,000 MWCO centrifugal filter device to collect any free metal in

the filtrate. Lanthanide concentrations were measured by ICP-MS in the original nanoparticle stock and in the filtrates, allowing for calculation of percent of lanthanide leakage.

*Cell Culture and Tumor Model*

T6-17 murine fibroblasts (a derivative of the NIH/3T3 line and kindly provided by Mark Greene, PhD, FRCP, University of Pennsylvania) were cultured and maintained in Dulbecco's modified Eagle's medium (DMEM), supplemented with 10% fetal bovine serum (FBS), 1% penicillin/streptomycin at 37°C and 5% $CO_2$. Approximately 6-week old female nu/nu nude mice (Charles River Laboratory, Charles River, MA, USA) were maintained in accordance with the Institutional Animal Care and Use Committee of the University of Pennsylvania. Mice were anesthetized via isoflurane and T6-17 cells were injected subcutaneously into the back right flank ($2 \times 10^6$ cells in 0.2 mL PBS). Tumors were grown until the longest dimension was approximately 8 mm.

*Quantitation of Tumor Delivery, Biodistribution, and Blood Concentration by ICP-MS*

Three animal cohorts, each containing 3 animals, were used for multiplex experiments, as outlined in Table 2.1. Each nanoparticle formulation was injected at a dose of 10 mg Fe / kg body weight (for a total iron load of 30 mg/kg in each mouse) in 200 μL of injected solution.

**Table 2.1** Summary of animal injection groups (n=3 for all groups).

| Experimental Cohort | Number of Particles Co-injected | Description |
|---|---|---|
| Negative Zeta Potential | 3 | -20.8 mV, -12.2 mV, -5.2 mV SPIO (all ≈ 28 nm) |
| Positive Zeta Potential | 3 | +3.6 mV, +10.0 mV, +14.3 mV SPIO (all ≈ 28 nm) |
| Size | 3 | 15.52 nm, 29.05 nm, 70.72 nm SPIO (all ≈ -20 mV) |

For each experimental group, prior to injection, a nanoparticle aliquot was saved for inductively coupled plasma mass spectrometry (ICP-MS) determination of lanthanide concentration in the injected material. Following nanoparticle injection, 10 μL blood samples were collected from each animal, using the tail-nick method, at times of 1, 2, 4, 7, and 24 hours post-injection. After the final blood draw, the animals were sacrificed and the tumors, livers, spleens, kidneys, hearts, and lungs excised.

For ICP-MS analysis, analytical standards were purchased from SCP (Champlain, NY, USA) and trace metal grade nitric acid and aqua regia was purchased from Fisher Scientific (Pittsburg, PA, USA). All dilutions were done using in-house deionized water (≥18 MΩ-cm) obtained from a Millipore water purification system.

The pre-injection solutions, blood, tumor, and organ samples were analyzed for $^{158}$Gd (gadolinium), $^{147}$Sm (samarium), $^{153}$Eu (europium), and $^{165}$Ho (holmium), using an Elan 6100 ICP-MS (Perkin Elmer, Shelton, CT, USA) at the New Bolton Center Toxicology Laboratory, University of Pennsylvania, School of Veterinary Medicine, Kennett Square, PA, USA. The samples were weighed into Teflon PFA vials (Savillex, Minnetonka, MN, USA) and digested overnight with 70% nitric acid at 70° C. 0.1 mL of 2 ppm $^{159}$Tb (terbium) was added to each of the digested samples and the mixtures were

diluted with deionized water to a final volume of 10 mL. The lanthanide concentration of each sample was measured using a calibration curve of aqueous standards at 0.01, 0.1, 1.0, and 10 ppb for each metal.

The performance of the instrument and accuracy of the results were monitored by analyzing a reagent blank and bovine serum control serum (Sigma) prior to analysis of the samples. Also, standard reference material (Peach Leaves 1547) obtained from National Institute of Standards and Technology (NIST, Gaithersburg, MD, USA) with known values of iron and rare earth elements was analyzed with each batch of samples.

For each nanoparticle formulation, the percent injected dose per gram of tissue, was calculated as $[Ln]_{sample}$ / ($[Ln]_{inj}$*$M_{inj}$) where $[Ln]_{sample}$ is the lanthanide concentration in the sample (blood, tumor, or organ tissue), $[Ln]_{inj}$ is the lanthanide concentration in the injected nanoparticle solution, and $M_{inj}$ is the mass of nanoparticle solution injected (0.2 grams).

## 2.4 Results and Discussion

*Synthesis of and Characterization of Ln-SPIO*

Lanthanide doped superparamagnetic iron oxide (SPIO) nanoparticles were prepared by including a small amount of lanthanide metal with the ferric and ferrous salts during synthesis. Five different lanthanide metals (Gd, Eu, Ho, Sm, and Er) were successfully incorporated into SPIO nanoparticles. Following synthesis and purification of each Ln-SPIO formulation, differential centrifugation and chemical surface modification were used to generate orthogonal sets of nanoparticles having either fixed size and varying surface charge or fixed surface charge and varying size (Table 2.2).

**Table 2.2** Physicochemical properties of the nine unique Ln-SPIO formulations .

| Tracer Metal | Hydrodynamic Diameter (nm) | Zeta Potential (mV), HEPES, pH 7.4 | r2 ($mM^{-1}s^{-1}$) | r1 ($mM^{-1}s^{-1}$) | Core Size (nm) | Ln / Fe% |
|---|---|---|---|---|---|---|
| Ho | **15.52** | -19.6 | < 5 | < 0.5 | 5.1 ± 1.9 | 17.8 |
| Eu | **29.05** | -20.7 | 141.75 | 9.35 | 17.4 ± 3.0 | 1.6 |
| Gd | **70.72** | -19.6 | 214.97 | 2.26 | 41.1 ± 10.6 | 8.0 |
| Sm | 29.84 | **-20.8** | 150.41 | 9.99 | 19.4 ± 3.9 | 1.7 |
| Eu | 28.61 | **-12.2** | 137.18 | 9.10 | 19.2 ± 3.5 | 2.9 |
| Gd | 26.06 | **-5.2** | 123.66 | 11.79 | 15.9 ± 2.7 | 2.0 |
| Sm | 29.16 | **+3.6** | 142.38 | 9.22 | 19.8 ± 3.8 | 1.7 |
| Gd | 27.29 | **+10.0** | 106.76 | 10.31 | 15.1 ± 2.6 | 2.0 |
| Eu | 29.47 | **+14.3** | 176.58 | 8.87 | 18.6 ± 3.8 | 2.9 |

Specifically, to investigate the effect of surface charge, 6 nanoparticle formulations were generated, each with a hydrodynamic diameter of approximately 28 nm but with zeta potentials ranging from -20.8 mV to +14.3 mV (Figure 2.2 A). Since it was hypothesized that negatively and positively charged nanoparticles could not be combined in a single injection due to electrostatic aggregation, these nanoparticles were divided into two sets, one with three negatively charged nanoparticles and one with 3 positively charged nanoparticles. Consequently, only three different Ln-SPIO cores were necessary (Gd, Eu, and Sm) for each of these studies. To investigate the effect of size, three nanoparticle formulations were generated, each with a zeta potential of approximately -20 mV, but with sizes of 15.52 nm, 29.05 nm, and 70.72 nm (Figure 2.2 B).

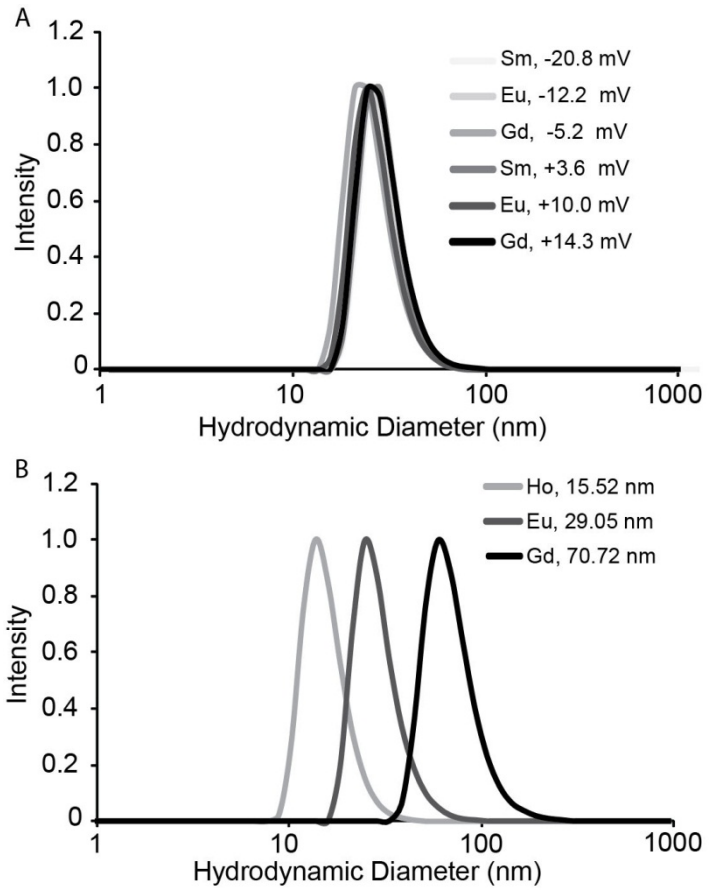


**Figure 2.2** Dynamic light scattering (DLS) size distributions for Ln-SPIO nanoparticles. (A) The six nanoparticle formulations used to investigate the effect of zeta potential on nanoparticle biodistribution and blood clearance have near-equivalent size distributions. (B) The three nanoparticle formulations that were used to isolate the effect of size on nanoparticle biodistribution and blood clearance have distinct size distributions (each with zeta potential ≈ -20 mV).

The mean core size for each formulation of Ln-SPIO was determined by transmission electron microscopy (Table 2.2) and the core morphology was examined (Figure 2.3 A-D). Consistent with SPIO previously synthesized by co-precipitation,[8] the medium and large size formulations have cores consisting of multiple individual crystals, resulting in a heterogeneous appearance.

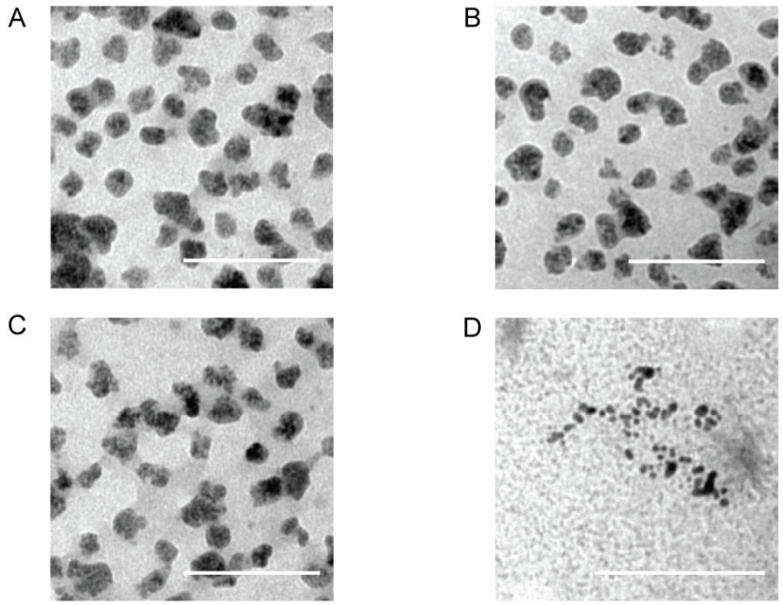


**Figure 2.3** TEM images of Ln-SPIO: Representative TEM images of (A) Sm-SPIO (core size, CS = 19.4±3.9nm, hydrodynamic diameter, HD = 29.84nm), (B) Eu-SPIO (CS = 19.2±3.5nm, HD = 28.61nm), (C) Gd-SPIO (CS = 15.9±2.7nm, HD = 26.06nm) and (D) Ho-SPIO (CS = 5.1±1.9nm, HD = 15.52nm). All scale bars are 100 nm.

Energy dispersive X-Ray spectroscopy (EDS) was used to further confirm that each lanthanide metal was incorporated into the iron core. Specifically, when examining the nanoparticles under transmission electron microscopy, EDS regions of interest placed in the background (i.e. not containing any nanoparticles) yielded signatures of ions of the buffer (Na, Cl) and the TEM grid itself (Cu), but no lanthanide was detectable in the background solution. When the EDS region of interest was moved onto a group of nanoparticles, very large Fe signatures were detected, as well as signatures corresponding to the specific lanthanide that was used for that synthesis (Figure 2.4). EDS examination of conventional SPIO nanoparticles yielded only iron signatures without any lanthanide peaks.

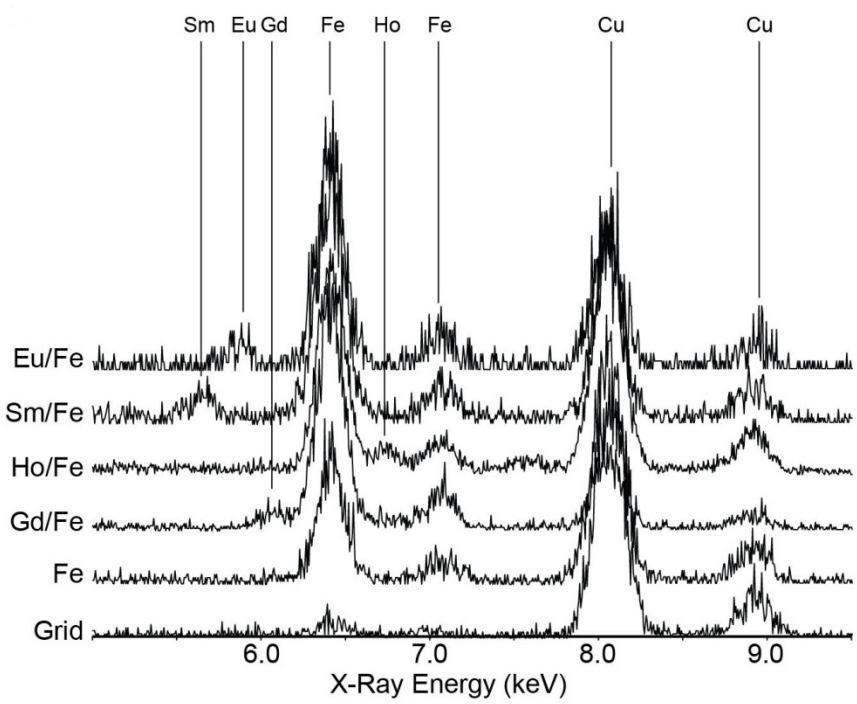


**Figure 2.4** EDS spectra of background (Grid), iron only SPIO (Fe), and Ln-SPIO doped with either Eu, Sm, Ho, or Gd, demonstrating specific incorporation of each lanthanide metal into the nanoparticle core.

MR imaging following a multiplex injection of SPIO nanoparticles provides little information, since the contribution of each individual nanoparticle formulation cannot be de-convoluted. Nevertheless, with the exception of Ho-SPIO, it was found that each Ln-SPIO nanoparticle used in the studies possessed magnetic relaxivities that were comparable to un-doped dextran SPIO (Table 2.2). The Ho-SPIO used in the size study had negligible magnetic relaxivity due to the method in which it was processed to obtain the small size. Prior to processing, the Ho-SPIO had relaxivities similar to the other Ln-SPIO formulations.

To ensure that the lanthanide metals within the core of each SPIO formulation would not readily leach/leak from the nanoparticle following intravenous injection, the stability of each Ln-SPIO was evaluated in serum (Figure 2.5). Upon exposure to 100% serum for 24 hours at 37°C, each Ln-SPIO nanoparticle experienced less than 0.5% leakage of lanthanide metal into the bulk solution. In fact, for two of the Ln-SPIO (Sm and Eu) the amount of leakage was below the limit of detection (≈ 0.2%).

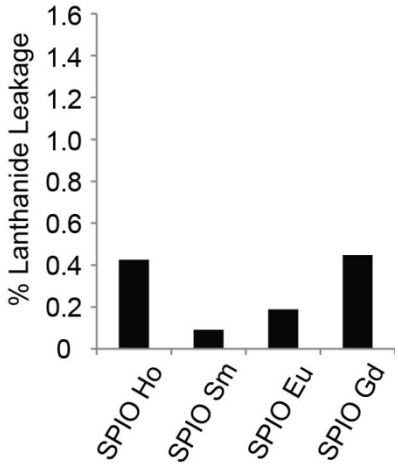


**Figure 2.5** Stability of various lanthanide doped nanoparticles, assayed by percent of lanthanide leakage observed after 24 hours of incubation in 100% serum at 37°C.

*Effect of Surface Charge on SPIO Biodistribution*

The surface charge of the nanoparticle (with a fixed hydrodynamic diameter of approximately 28 nm) was found to have a significant impact on passive tumor delivery (Figure 2.6). Specifically, the mildly negative SPIO formulation (-12.2 mV in 10 mM HEPES) was found to have the highest tumor delivery at 2.05 % injected dose / gram tumor 24 hours post-injection. Zeta potentials closer to neutrality (-5.2 mV and +3.6 mV) had somewhat lower tumor delivery of 1.37 and 1.23 % ID/g, while more extreme

negative values (-20.8 mV) resulted in even less tumor delivery (1.09 % ID/g). The moderate and extreme positive values of zeta potential, at +10.0 mV and +14.3 mV, resulted in the poorest tumor delivery (0.84 and 0.29 % ID/g, respectively).

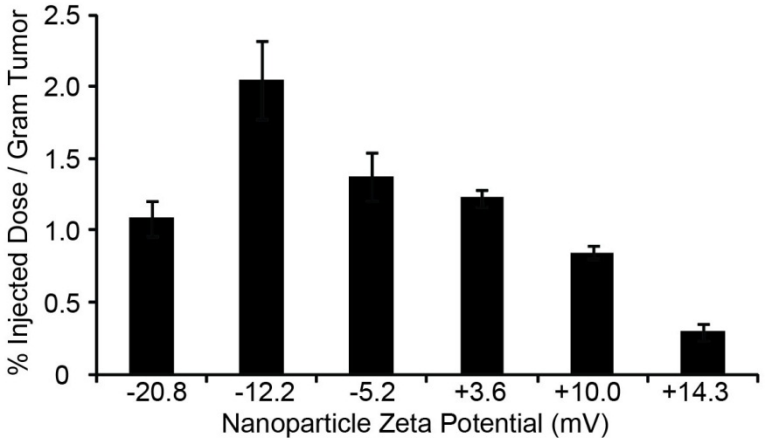


**Figure 2.6** Effect of SPIO surface charge on passive nanoparticle delivery to T6-1 flank tumors, 24 hours post-injection (reported as percent injected dose per gram tumor tissue).

Nanoparticle accumulation in other organs (liver, spleen, kidney, lungs, and heart) was also examined 24 hours post-injection (Figure 2.7). Large uptake was observed in organs of the reticuloendothelial system (RES), with liver concentrations ranging from 25-45 % ID/g and spleen concentrations ranging from 13-40 % ID/g. The lungs, kidney, and heart all showed modest uptake in the range of 0.5-2 % ID/g, with the notable exception of the heart delivery of the three positively charged SPIO nanoparticles. It was found that each positively charged SPIO had significantly elevated delivery to the heart, in the range of 5-7 % ID/g. These data were confirmed with a second set of mice. It was also found that at 5 minutes post-injection, the concentration of +14.3 mV SPIO nanoparticles in a washed heart specimen was 12.2 % ID/g, while its concentration in the blood at 5 minutes was only 2.3 % ID/g.

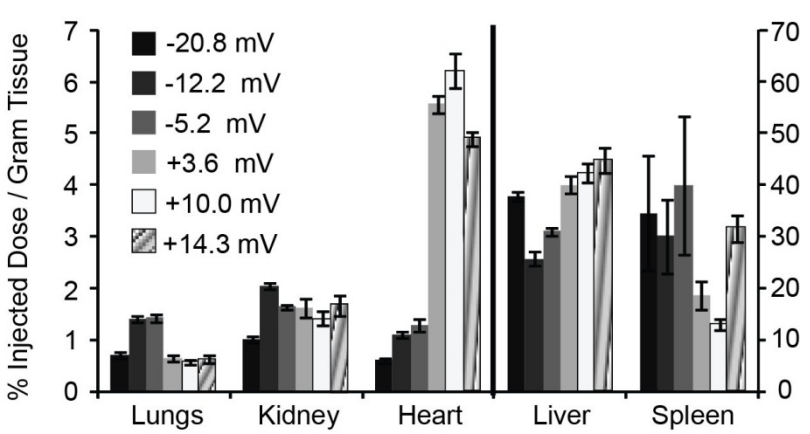


**Figure 2.7** Effect of SPIO surface charge on biodistribution, at 24 hours post-injection.

Finally, the blood clearance profile for each surface charge was investigated (Figure 2.8). Similar to the results observed for tumor delivery, the -12.2 mV SPIO demonstrated the longest blood circulation time, while the more neutral formulations (-5.2 mV and +3.6 mV) had a shorter circulation time. The more positively charged particles exhibited very rapid clearance, with the +14.3 mV formulation's blood concentration falling to 1.1 % ID/g in the first hour post-injection.

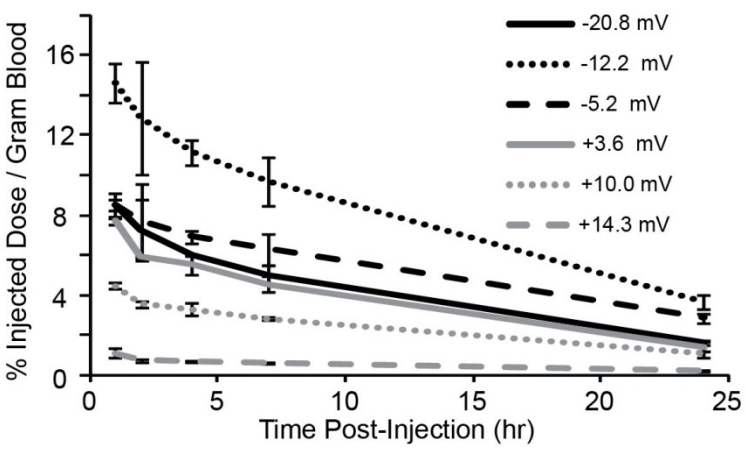


**Figure 2.8** Effect of SPIO surface charge on blood clearance.

It should be noted that the absolute value of a zeta potential measurement is highly dependent on the identity and ionic strength of the buffer in which it is measured. The zeta potentials (as measured in pH 7.4, 10 mM HEPES, with no additional salt) of the 6 nanoparticle formulations tested in this investigation were -20.8, -12.2, -5.2, +3.6, +10.0, and +14.3 mV. A low ionic strength buffer was selected to measure zeta potential for this study in order to highlight relatively small differences in surface charge. In this buffer, the -5.2 mV and +3.6 mV formulations should be considered close to neutral; the -12.2 mV and +10.0 mV are mildly negative and positive, respectively; the remaining two formulations have more significant negative and positive charges.

Previous studies have demonstrated that prolonged blood circulation, and therefore, optimal tumor delivery by the enhanced permeability and retention (EPR) effect is achieved with nanoparticles displaying a neutral to mildly negative surface charge.[9, 10] When the surface charges becomes overly negative, excessive association with phagocytic cells of the reticuloendothelial system (RES) decreases circulation time[9, 10] and it has been commonly reported that positively charged nanoparticles are cleared very rapidly due to local electrostatic interactions near the injection site.[11]

The results obtained in the two zeta potential experimental cohorts are consistent with this general literature consensus, and the tumor delivery was found to correlate well with blood circulation time, consistent with passive delivery by EPR. Specifically, the mildly negative surface charge of -12.2 mV yielded the longest circulation time and greatest tumor delivery. More neutral formulations resulted in slightly lower, but still significant, circulation time and tumor delivery. Excessively negative SPIO (-20.7 mV)

displayed still more rapid clearance and decreased tumor delivery, while moderately and strongly positive formulations had poor circulation time and tumor delivery.

As expected, a large amount of the injected material, for all surface charges, was found in the liver and spleen. However, the two surface charges that yielded the greatest tumor delivery (-5.2 mV and -12.2 mV) exhibited the least liver uptake. The more significantly negative formulation (-20.7 mV) had a larger liver uptake, consistent with stronger association with Kupffer cells and clearance by the liver. Given its relatively large mass, the liver represents a major mechanism by which nanoparticles are removed from circulation, and since nanoparticles removed from circulation by the liver cannot end up delivered to the tumor, it was reasonable to observe the liver concentration as roughly inversely related to tumor delivery.

The relatively high concentration (≈ 6% ID/g) of positively charged nanoparticles observed in the heart 24 hours post-injection was an unexpected finding that is likely due to a “first pass effect”, since the right chambers of the heart are the first organ that the nanoparticles reach after intravenous injection. In fact, washed heart tissue sampled at 5 minutes post-injection contained 12.2% ID/g. Since the nanoparticle concentration in the blood at 5 minutes post-injection was only 2.3% ID/g, the high concentration of nanoparticles detected in the heart cannot be attributed to residual blood in the chambers. The results are consistent with a rapid initial interaction of the positively charged nanoparticles with the endocardium, followed by approximately half of this initial load being washed away during the next 24 hours.

*Effect of Nanoparticle Size on SPIO Biodistribution*

The hydrodynamic diameter of SPIO nanoparticles (with a fixed zeta potential of approximately -20 mV) was also found to influence their passive tumor delivery (Figure 2.9 A). Specifically, the smallest formulation of 15.52 nm yielded the greatest tumor delivery at 1.61 % ID/g, the medium sized formulation of 29.05 nm resulted in a lower delivery at 1.29 % ID/g, and the largest formulation of 70.72 nm demonstrated the lowest delivery at 1.06 % ID/g. Similarly to the negatively charged SPIO tested in the previous cohort of animals, all nanoparticle sizes demonstrated significant RES uptake (28 – 42 % ID/g in the liver and 18 – 38 % ID/g in the spleen) and more modest uptake in the heart, lungs, and kidneys (0.5 – 2 % ID/g, Figure 2.9 B).

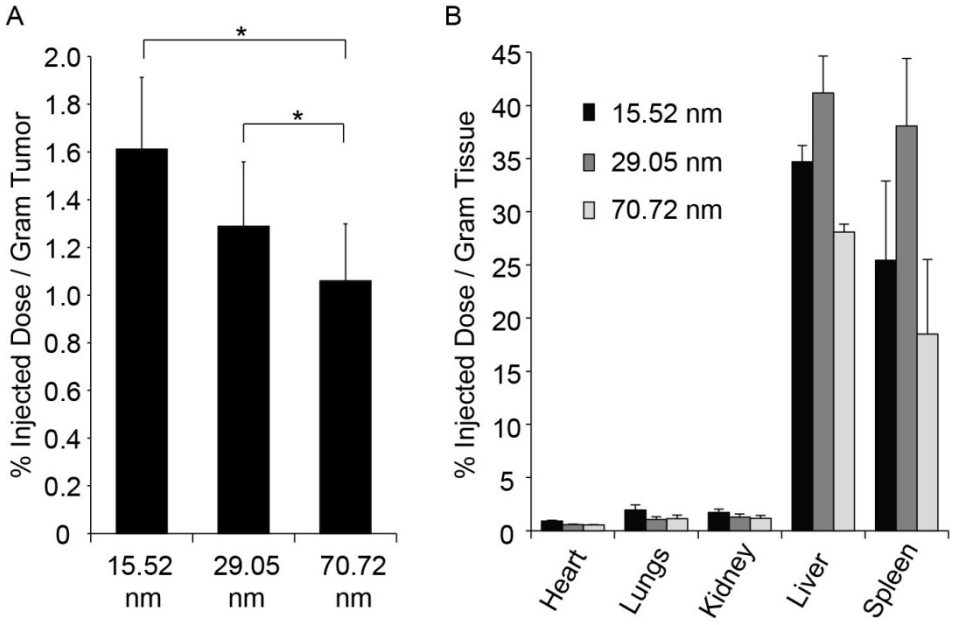


**Figure 2.9**. Effect of SPIO hydrodynamic diameter on tumor delivery and biodistribution. (A) Passive nanoparticle delivery to T6-17 flank tumors for three distinct SPIO size distributions. (B) Nanoparticle uptake in other organs as a function of size.

The blood clearance of the three different sizes tested proved especially interesting (Figure 2.10). While the 29.05 nm, -20.7 mV nanoparticle exhibited a similar circulation profile as it did in the previous cohort of animals, both the smaller nanoparticle (15.52 nm) and the larger nanoparticle (70.72 nm) exhibited more prolonged circulation.

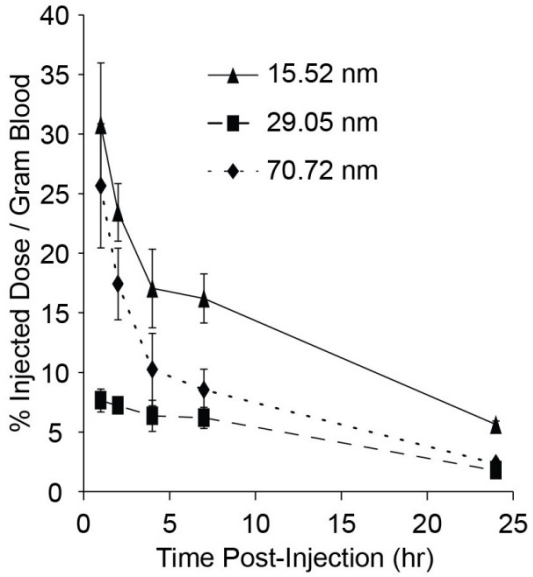


**Figure 2.10** Effect of SPIO hydrodynamic diameter on blood clearance.

Previous studies have shown that there is a window, roughly between 5 nm and 100 nm, in which nanoparticle blood circulation time and passive tumor delivery by EPR is maximized.[12-15] If the construct is too small, it can be rapidly and efficiently cleared through the kidneys, but if too large (>200 nm), it is efficiently trapped by cells of RES organs.[16] All three SPIO sizes tested were comfortably above the renal filtration threshold, so it was not surprising to observe an inverse relationship between nanoparticle size and tumor delivery.

However, unlike in the zeta potential studies, the tumor delivery was not observed to be strictly correlated to circulation time (the largest SPIO, at 70.72 nm, demonstrated the lowest tumor delivery, despite having intermediate circulation time). It is possible that the 70.72 nm SPIO exhibit greater blood concentrations (especially at early time points) because their larger size makes extravasation into tissue (including the tumor) more difficult, but the size is not yet large enough to result in excessive interaction with cells of the RES. It has also been demonstrated that diffusion-based penetration into tumors is strongly dependent on nanoparticle size.[17] It is likely the larger, 70.72 nm formulation, was not able to efficiently diffuse through the tumor tissue and, therefore, experienced a greater "wash out" effect over the 24 hours of the study.

## 2.5 Improved Statistical Power of Multiplex (Ratiometric) Data

One of the most promising aspects of this multiplex ICP-MS approach to measuring biodistribution and blood clearance is the robust statistical power inherent in injecting all nanoparticle formulations one wishes to compare into a single animal. *In vivo* studies often exhibit a high degree of experimental variability (e.g. differences in tumor size, subject weight, and physiology). When each nanoparticle formulation is injected alone, comparison between formulations must be made with unpaired statistical tests, which often necessitates a larger number of animals in order to detect statistically significant differences in the performance of two or more nanoparticles. However, when each nanoparticle is simultaneously administered to all animals, subject-to-subject variability is effectively removed by the use of paired statistics. For example, the absolute tumor delivery of two particular nanoparticle formulations might be highly variable between three animals, confounding attempts to compare the formulations. However, if in

each given subject, one nanoparticle is observed to have higher tumor delivery than the other, one can more easily conclude that formulation is superior.

Looking at the statistical analysis of the experimental cohort (3 animals) investigating the effect of nanoparticle size, between the 6 organs investigated for 3 sizes, there were 18 head-to-head statistical comparisons that could be made. Treating the data as unpaired, using $P < 0.05$ as the criterion, 6 of the comparisons were statistically significant; treating the data as paired, 15 of the possible 18 comparisons demonstrated statistical significance. To highlight a particular data set, the average kidney delivery of the 15.52 nm, 29.05 nm, and 70.72 nm sizes were 1.74, 1.29, and 1.16 % ID/g, respectively, each with a standard deviation of 0.26 – 0.29 % ID/g. These small differences in nanoparticle concentration could not be deemed statistically different (P values ranging from 0.06 to 0.59) from one another if the data are treated as unpaired. However, given that in a given animal, the 15.52 nm nanoparticle always had the greatest concentration, followed by 29.05 nm, and then 70.72 nm, paired statistics indicated that each concentration was statistically different (P values ranging from 0.002 to 0.022). However, it should not be assumed that paired statistics (compared to unpaired) always necessarily result in a lower P value. In the experimental cohort investigating the effect of nanoparticle surface charge, there were several instances in which unpaired statistics would have produced P values less than 0.05 (which can always occur by chance when such a large number of comparisons are made) but paired analysis resulted in a P value greater than 0.05. The consequence of using paired statistics, therefore, is simply an increase in statistic power (i.e. a more accurate estimation of whether the difference is "real" can be obtained with a smaller sample size).

## 2.6 Conclusion

A synthetic protocol to stably incorporate lanthanide metals into the core of SPIO nanoparticles, without abolishing their magnetic properties, has been developed. The lanthanide dopant can be used as a unique tracer atom, allowing the sensitive and quantitative detection of the nanoparticles by ICP-MS, both *in vitro* and *in vivo*, without interference from endogenous signals. When distinct lanthanide metals are incorporated into nanoparticles with distinct physicochemical properties, ICP-MS allows for the concentration of each nanoparticle formulation to be measured independently of other formulations that may be present in the solution or tissue of interest. As a proof of principle, this ICP-MS multiplex approach was used to evaluate the effect of nanoparticle size and surface charge on tumor delivery, biodistribution, and blood clearance *in vivo*. The results obtained were consistent with the general literature consensus about these properties and only required a small number of experimental animals, due to the inherent and robust statistical power of a multiplex (ratiometric) approach. Furthermore, it is envisioned that the ICP-MS multiplex analysis described could prove to be a powerful future research tool in the investigation of other nanoparticle formulations with diverse physicochemical properties and active targeting capabilities, while allowing for nanoparticle standardization.

## 2.7 References


1. Matson, M. L.; Wilson, L. J., Nanotechnology and MRI contrast enhancement. *Future Med Chem* **2010,** 2, (3), 491-502.

2. Solomon, M.; D'Souza, G. G., Recent progress in the therapeutic applications of nanotechnology. *Curr Opin Pediatr* **2011,** 23, (2), 215-20.

3. Tan, S. J.; Kiatwuthinon, P.; Roh, Y. H.; Kahn, J. S.; Luo, D., Engineering Nanocarriers for siRNA Delivery. *Small* **2011,** 7, (7), 841-56.

4. Crayton, S. H.; Chen, A. K.; Cheng, Z.; Tsourkas, A., Molecular Imaging. In *Comprehensive Biomaterials*, Ducheyne, P.; Healy, K.; Hutmacher, D.; Kirkpatrick, J., Eds. Elsevier: 2010.

5. Thorek, D. L.; Chen, A. K.; Czupryna, J.; Tsourkas, A., Superparamagnetic iron oxide nanoparticle probes for molecular imaging. *Ann Biomed Eng* **2006,** 34, (1), 23-38.

6. Muzykantov, V. R.; Puchnina, E. A.; Atochina, E. N.; Hiemish, H.; Slinkin, M. A.; Meertsuk, F. E.; Danilov, S. M., Endotoxin reduces specific pulmonary uptake of radiolabeled monoclonal antibody to angiotensin-converting enzyme. *J Nucl Med* **1991,** 32, (3), 453-60.

7. Cahouet, A.; Denizot, B.; Hindre, F.; Passirani, C.; Heurtault, B.; Moreau, M.; Le Jeune, J.; Benoit, J., Biodistribution of dual radiolabeled lipidic nanocapsules in the rat using scintigraphy and gamma counting. *Int J Pharm* **2002,** 242, (1-2), 367-71.

8. Thorek, D. L.; Tsourkas, A., Size, charge and concentration dependent uptake of iron oxide particles by non-phagocytic cells. *Biomaterials* **2008,** 29, (26), 3583-90.

9. Moghimi, S. M.; Davis, S. S., Innovations in avoiding particle clearance from blood by Kupffer cells: cause for reflection. *Crit Rev Ther Drug Carrier Syst* **1994,** 11, (1), 31-59.

10. Moghimi, S. M.; Hunter, A. C.; Murray, J. C., Long-circulating and target-specific nanoparticles: theory to practice. *Pharmacol Rev* **2001,** 53, (2), 283-318.

11. Chouly, C.; Pouliquen, D.; Lucet, I.; Jeune, J. J.; Jallet, P., Development of superparamagnetic nanoparticles for MRI: effect of particle size, charge and surface nature on biodistribution. *J Microencapsul* **1996,** 13, (3), 245-55.

12. Enochs, W. S.; Harsh, G.; Hochberg, F.; Weissleder, R., Improved delineation of human brain tumors on MR images using a long-circulating, superparamagnetic iron oxide agent. *J Magn Reson Imaging* **1999,** 9, (2), 228-32.

13. Moore, A.; Marecos, E.; Bogdanov, A., Jr.; Weissleder, R., Tumoral distribution of long-circulating dextran-coated iron oxide nanoparticles in a rodent model. *Radiology* **2000,** 214, (2), 568-74.

14. Zimmer, C.; Weissleder, R.; Poss, K.; Bogdanova, A.; Wright, S. C., Jr.; Enochs, W. S., MR imaging of phagocytosis in experimental gliomas. *Radiology* **1995,** 197, (2), 533-8.

15. Zimmer, C.; Wright, S. C., Jr.; Engelhardt, R. T.; Johnson, G. A.; Kramm, C.; Breakefield, X. O.; Weissleder, R., Tumor cell endocytosis imaging facilitates delineation of the glioma-brain interface. *Exp Neurol* **1997,** 143, (1), 61-9.

16. McNeil, S. E., Nanotechnology for the biologist. *J Leukoc Biol* **2005,** 78, (3), 585-94.

17. Perrault, S. D.; Walkey, C.; Jennings, T.; Fischer, H. C.; Chan, W. C., Mediating tumor targeting efficiency of nanoparticles through design. *Nano Lett* **2009,** 9, (5), 1909-15.

# Chapter 3: Generalization of ICP-MS Analytical Method to Other Nanoparticle Formulations and Validation of Multiplex Data

## 3.1 Abstract

The previous chapter outlined an analytical protocol for stably incorporating lanthanide metals into the iron core of superparamagnetic iron oxide (SPIO) nanoparticles and then using ICP-MS to quantify of the biodistribution and blood clearance of multiple lanthanide-doped SPIO simultaneously administered to a single animal. The method used for lanthanide incorporation (i.e. co-precipitation of iron and lanthanide) was unique to SPIO. However, much greater utility can be gained if lanthanide multiplex analysis could be applied to a wider range of nanoparticle formulations. In this chapter, liposomes, polymersomes, dendrimers, and gold nanoparticles were examined. With the exception of gold nanoparticles, incorporation of the metal was accomplished using the chelator DTPA. In the case of the nanovesicles, the lanthanide was chelated to DTPA and then encapsulated within the aqueous core. For the dendrimers, DTPA was covalently conjugated to the nanoparticle surface. The gold nanoparticles do not require an additional dopant, since the gold itself serves as an orthogonal, non-endogenous tracer. Given that the most commonly used methods to radiolabel macropharmaceuticals and nanoparticles exploit radionuclide-chelate complexes, the successful use of chelators to incorporate the tracer lanthanide demonstrates that the ICP-MS multiplex approach can be conveniently substituted for radiolabeling in biodistribution and clearance studies.

## 3.2 Introduction

Given the variety and versatility of nanoparticle based carrier systems, it is not surprising that there is tremendous research interest to develop nanoparticles into imaging and therapeutic agents. Radionuclides play a major role in such studies since they provide quantitative information and have very high sensitivity. For example, gamma emitters such as $^{111}$In and $^{99m}$Tc or positron emitters such as $^{18}$F and $^{64}$Cu can be used as the source of signal when designing nanoparticle based contrast agents for SPECT[1-3] and PET[4-6] studies, respectively. For therapeutic studies of drug carrying nanoparticles, these and other radionuclides such as $^{125}$I can also serve as tracers, in order to determine the level of payload delivery to the site of interest as well as assess off-target toxicity. Furthermore, radionuclides such as $^{188}$Re,[7, 8] $^{90}$Y,[9] $^{131}$I,[10] and $^{225}$Ac[11, 12] can themselves provide the therapeutic effect (*i.e.* radiopharmaceutical nanoparticles).

Within the nanoparticle field, as well as the larger research community, there is a great deal of experience working with radionuclides for imaging, tracing, and radiotherapy. There are two very common ways to associate radionuclides with nanoparticles. One is encapsulation, where a metal or non-metal radionuclide is non-covalently confined to the interior of the nanoparticle. For example, liposomes and polymersomes possess and aqueous core capable of confining radionuclides[13, 14] (as well as many other materials including fluorophores and pharmaceuticals). The other common approach is to covalently attach a chelator, such as DTPA or DOTA, to the nanoparticle and then bind a metal radionuclide to the chelator.[15, 16] Less commonly, nanoparticles are formed using radiolabeled precursors.[17]

Radiolabeling is the “gold standard” for evaluating an agent’s pharmacokinetics and biodistribution and the incorporation of metal radionuclides into nanoparticles and

other macromolecules is well established practice. We sought to employ the same common methods (*i.e.* encapsulation and chelation) to incorporate lanthanide tracers into nanoparticles, thereby allowing for quantitative measurement of blood clearance and tumor delivery using ICP-MS. However, unlike radiolabeling, an ICP-MS based approach should allow for high level multiplexing of these measurements in single animals. For further validation, we sought to confirm that the blood clearance profiles and tumor delivery data obtained with the ICP-MS multiplex injection approach was both reproducible across a range of injection pools and agreed with data obtained for conventional single agent injection.

## 3.3 Materials and Methods

*Synthesis of PAMAM (G3)−DOTA−Ho and PAMAM (G5)-DOTA-Pr*

10 mg of PAMAM G3 dendrimer (ethylenediamine core, generation 3, Dendritech, Midland, MI, USA) was dissolved in 4 mL of sodium bicarbonate buffer (0.1 M, pH 9.5) and reacted with 35 mg of DOTA-NHS-ester (Macrocyclics, Dallas, TX, USA) for 10 hours. The pH of the solution was maintained at 9.5 over the course of the reaction by addition of NaOH. The PAMAM−DOTA was purified by centrifugal filter devices (Amicon Ultra-4, 5000 MWCO, Millipore, Billerica, MA). The purified PAMAM−DOTA conjugates were mixed with 18 mg of $HoCl_3 \bullet 6H_2O$ in 0.1 M citrate buffer (pH 5.6) overnight at 42°C. Finally, the dendrimer was purified from free $Ho^{3+}$ with 5000 MWCO centrifugal filter devices. PAMAM (G5)-DOTA-Pr was prepared using an analogous procedure, substituting PAMAM-G5 in the place of PAMAM-G3 and $PrCl_3 \bullet 6H_2O$ for $HoCl_3 \bullet 6H_2O$. In order to ensure the two dendrimer formulations were

negatively charged, each was reacted overnight with 1 M succinic anhydride in 0.1 M sodium bicarbonate buffer and then purified by centrifugal filtration.

*Preparation of DOTA−Ce Encapsulating Polymersomes*

DOTA-Ce was prepared by dissolving 303 mg of DOTA (Macrocyclics) in 3 mL of citrate buffer (0.1 M, pH 5.6) and reacting with 223.8 mg of $CeCl_3 \bullet 7H_2O$ for 10 hours. The reaction solution was maintained at pH 6.0 with NaOH. Polymersomes were prepared by dissolving 20 mg of PEO-PBD block copolymer (polyethyleneoxide[600 Da]-*block*-polybutadiene[1200 Da], Polymer Source, Dorval, Quebec, Canada) in chloroform in a glass vial and then evaporating the solvent using a stream of $N_2$ gas. After further drying under vacuum overnight, the residual polymer film was hydrated with 1 mL DOTA-Ce aqueous solution in a 65 °C water bath for 30 min and then sonicated for another 1 h at the same temperature. Polymersomes were subjected to ten freeze–thaw–vortex cycles in liquid nitrogen and warm $H_2O$ (65 °C), followed by extrusion 21 times through two stacked 100 nm Nuclepore polycarbonate filters using a stainless steel extruder (Avanti Polar Lipids, Alabaster, AL). Unencapsulated DOTA-Ce was removed via size-exclusion chromatography using Sepharose CL-4B (Sigma-Aldrich, St. Louis, MO, USA) and polymersomes were further purified through repeated washing on centrifugal filter devices (Amicon Ultra-4, 100K MWCO, Millipore). Any remaining positively-charged surface amino groups were then blocked by carboxylation with succinic anhydride.

*Preparation of DOTA−Dy Encapsulating Liposomes*

DOTA-Dy was prepared by dissolving 303 mg of DOTA in 3 mL of citrate buffer (0.1 M, pH 5.6) and reacting with 226.2 mg of $DyCl_3 \bullet 6H_2O$ for 10 hours. The reaction solution was maintained at pH 6.0 with NaOH. For liposome synthesis, hydrogenated soy phosphatidylcholine (HSPC), cholesterol, and 1,2-distearoyl-sn-glycero-3-phosphoethanolamine-N-[methoxy-(polyethylene glycol)-2000] (mPEG2000-DSPE) were obtained from Avanti Polar Lipids. 10 mg of 55□mol% HSPC/40□mol% CHOL/5□mol% mPEG2000-DSPE mixture was dissolved in chloroform in a glass vial, followed by evaporation of the solvent with a stream of $N_2$ gas and further drying under vacuum for at least 4 hours. DOTA-Dy encapsulating liposomes were then synthesized and purified with a procedure analogous to the preparation of DOTA-Ce encapsulating polymersomes.

*Preparation of PEG-coated Gold Nanoparticles*

Gold nanoparticles were prepared according to a protocol established by Turkevich.[18] Briefly, 200 ml of aqueous 0.01% (w/v) $HAuC1_4$ was brought to a boil and then 7 ml of aqueous 1% (w/v) sodium citrate was added. The color of the solution initially changed to a grayish-black and then to red within a few minutes. The solution was allowed to cool at room temperature and then filtered through a 0.2 µm pore size nylon filter system. The AuNPs were then coordinated with HS – PEG (5K) – $OCH_3$ (Sigma Aldrich) at a mass ratio of 8:1 HS – PEG - $OCH_3$:Au. After 2 hours of constant stirring, the AuNP solution was then purified from excess reactants using 50K MWCO centrifugal filter devices.

*Nanoparticle Physicochemical Characterization*

Stock samples of dendrimers, polymersomes, liposomes, and gold nanoparticles were diluted into pH 7.4 phosphate buffered saline for determination of the hydrodynamic diameter by dynamic light scattering (DLS). Measurements were acquired with a Zetasizer Nano-ZS (Malvern Instruments, Worcestershire, UK) using the non-invasive back-scatter (NIBS) mode. For zeta potential measurements, stock samples were diluted into phosphate buffered saline at pH 7.4 and then mean nanoparticle zeta potential was measured using a Zetasizer Nano-ZS.

*Nanoparticle Stability Assays*

The stability of the nanoparticles was measured as the amount of lanthanide leakage that could be observed in serum. Nanoparticles were incubated in 100% fetal bovine serum (FBS) at 37°C with shaking. Aliquots were removed at 1, 2, 4, 6, and 24 hours and applied to a 4,000 MWCO centrifugal filter device to collect any free metal in the filtrate. Lanthanide concentrations were measured by ICP-MS in the original nanoparticle stock and in the filtrates, allowing for calculation of percent of lanthanide leakage.

*Cell Culture and Tumor Model*

T6-17 murine fibroblasts (a derivative of the NIH/3T3 line and kindly provided by Mark Greene, PhD, FRCP, University of Pennsylvania) were cultured and maintained in Dulbecco's modified Eagle's medium (DMEM), supplemented with 10% fetal bovine serum (FBS), 1% penicillin/streptomycin at 37°C and 5% $CO_2$. Approximately 6-week

old female nu/nu nude mice (Charles River Laboratory, Charles River, MA, USA) were maintained in accordance with the Institutional Animal Care and Use Committee of the University of Pennsylvania. Mice were anesthetized via isoflurane and T6-17 cells were injected subcutaneously into the back right flank (2 x $10^6$ cells in 0.2 mL PBS). Tumors were grown until the longest dimension was approximately 8 mm.

*Quantitation of Tumor Delivery, Biodistribution, and Blood Concentration by ICP-MS*

Two animal cohorts, each containing 3 animals, were used for multiplex experiments, as outlined in Table 3.1. In the first experimental groups, which investigated a single type of SPIO, the nanoparticles were injected at a dose of 10 mg Fe / kg body weight in 200 μL of injected volume. In the second experimental group, which included a variety of additional nanoparticle platforms, the SPIO was injected at 10 mg Fe / kg body weight and the other formulations were injected at concentrations so that all tracer metal concentrations (lanthanide or gold) were approximately equal to that of the SPIO samples, ≈ 34 ppm, in 200 μL of injected solution.

**Table 3.1.** Summary of animal injection groups (n=3 for each groups).

| **Experimental Cohort** | **Number of Particles Co-injected** | **Description** |
|---|---|---|
| Single Particle | 1 | -20.8 mV, 29.8 nm SPIO |
| Additional Platforms | 7 | Gd-DTPA, G3 and G5 dendrimers, AuNP, SPIO, liposome, polymersome |

For each experimental group, prior to injection, a nanoparticle aliquot was saved for inductively coupled plasma mass spectrometry (ICP-MS) determination of lanthanide concentration in the injected material. Following nanoparticle injection, 10 μL blood samples were collected from each animal, using the tail-nick method, at times of 1, 2, 4, 7, and 24 hours post-injection. After the final blood draw, the animals were sacrificed and the tumors, livers, spleens, kidneys, hearts, and lungs excised.

For ICP-MS analysis, analytical standards were purchased from SCP (Champlain, NY, USA) and trace metal grade nitric acid and aqua regia was purchased from Fisher Scientific (Pittsburg, PA, USA). All dilutions were done using in-house deionized water (≥18 MΩ-cm) obtained from a Millipore water purification system.

The pre-injection solutions, blood, tumor, and organ samples were analyzed for $^{158}$Gd (gadolinium), $^{147}$Sm (samarium), $^{153}$Eu (europium), $^{165}$Ho (holmium), $^{166}$Er (erbium), $^{161}$Dy (dysprosium), $^{140}$Ce (cerium), $^{141}$Pr (praseodymium), and $^{197}$Au (gold) using an Elan 6100 ICP-MS (Perkin Elmer, Shelton, CT, USA) at the New Bolton Center Toxicology Laboratory, University of Pennsylvania, School of Veterinary Medicine, Kennett Square, PA, USA. The samples were weighed into Teflon PFA vials (Savillex, Minnetonka, MN, USA) and digested overnight with 70% nitric acid (or aqua regia for gold containing samples) at 70° C. 0.1 mL of 2 ppm $^{159}$Tb (terbium) was added to each of the digested samples and the mixtures were diluted with deionized water to a final volume of 10 mL. The lanthanide (or gold) concentration of each sample was measured using a calibration curve of aqueous standards at 0.01, 0.1, 1.0, and 10 ppb for each metal.

The performance of the instrument and accuracy of the results were monitored by analyzing a reagent blank and bovine serum control serum (Sigma) prior to analysis of the samples. Also, standard reference material (Peach Leaves 1547) obtained from National Institute of Standards and Technology (NIST, Gaithersburg, MD, USA) with known values of iron and rare earth elements was analyzed with each batch of samples.

For each nanoparticle formulation, the percent injected dose per gram of tissue, was calculated as $[Ln]_{sample} / ([Ln]_{inj} * M_{inj})$ where $[Ln]_{sample}$ is the lanthanide concentration in the sample (blood, tumor, or organ tissue), $[Ln]_{inj}$ is the lanthanide concentration in the injected nanoparticle solution, and $M_{inj}$ is the mass of nanoparticle solution injected (0.2 grams).

## 3.4 Results and Discussion

*Generalization of ICP-MS Multiplex Method with Additional Nanoparticle Platforms*

In order to demonstrate the generalizability and versatility of the ICP-MS multiplex approach, orthogonal metals were incorporated into a wide range of nanoparticle platforms and their tumor delivery and blood clearance was examined. Specifically, the small molecule Gd-DTPA, PAMAM dendrimers of generation 3 and 5, PEG coated gold nanoparticles, SPIO, a polymersome, and a liposome were all synthesized and conjugated to or encapsulated with orthogonal metals (Table 3.2).

**Table 3.2** Size and zeta potential of the nanoparticles used in the multiplatform study.

| Particle | Tracer Metal | Hydrodynamic Diameter (nm) | Zeta Potential (mV), PBS, pH 7.4 |
|---|---|---|---|
| Gd-DTPA | Gd | -- | -- |
| G3 Dendrimer | Ho | 4.2 | -0.38 |
| G5 Dendrimer | Pr | 6.1 | -7.58 |
| Gold NP | Au | 26.0 | -1.31 |
| SPIO | Er | 33.3 | -9.55 |
| Polymersome | Ce | 82.5 | -4.08 |
| Liposome | Dy | 93.8 | -1.35 |

The hydrodynamic diameter of these formulations was then measured in PBS, along with their surface charge (zeta potential), using DLS and electrophoretic mobility. Due to its very small size, the individual Gd-DTPA complex, however, is not amenable to DLS measurement. These results are reported in Table 3.2. All nanoparticle formulations possessed a neutral to moderately negative surface charge, making them compatible for co-injection. This group of nanoparticles spanned a wide range of sizes, from approximately 4 to 95 nm (Figure 3.1).

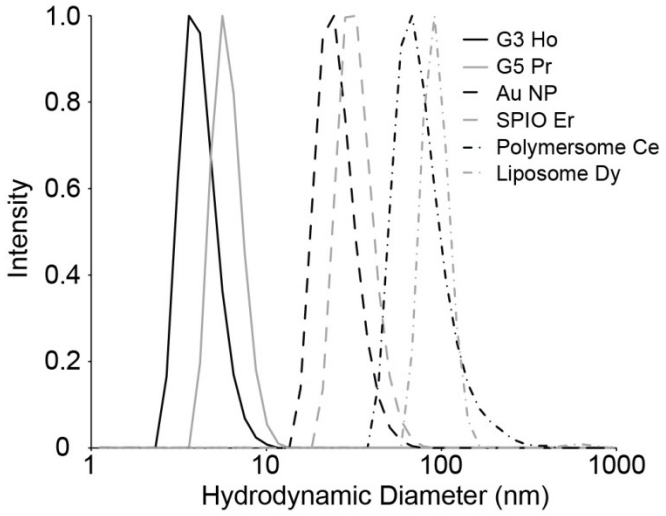


**Figure 3.1**. Size distributions of the nanoparticles (G3 and G5 dendrimer, gold (Au), SPIO, polymersome, and liposome) used in the multiplatform study.

The stability of the dendrimer chelates and nanovesicle formulations was also confirmed by incubation in 100% serum for 24 hours at 37°C. It was found that less than 0.4% of the lanthanide metal was released from the dendrimer chelates into the bulk solution, and less than 1.5% of the lanthanide metal encapsulated within the liposome and polymersome was released into the bulk solution (Figure 3.2).

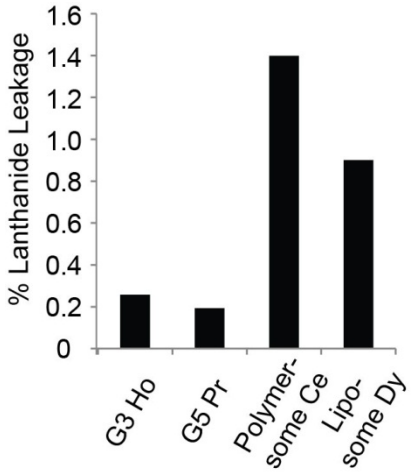


**Figure 3.2** Stability of various lanthanide doped nanoparticles, assayed by percent of lanthanide leakage observed after 24 hours of incubation in 100% serum at 37°C.

These 7 formulations were simultaneously injected and their tumor delivery (Figure 3.3 A) and blood clearance (Figure 3.3 B) were evaluated. The small molecule Gd-DTPA and smallest particle (G3 dendrimer, 4.2 nm) had tumor delivery at or below the detection limit of 0.17% ID/g at 24 hours, and were entirely cleared from circulation in the first hour post-injection. Interestingly, the G5 dendrimer, with a size only slightly larger than the G3 dendrimer (6.1 nm) exhibited the greatest tumor delivery at 4.36% ID/g and a prolonged circulation time, with 5.83% ID/g still circulating at 24 hours post-injection. The significantly larger PEG-coated gold nanoparticle also demonstrated very robust tumor delivery at 4.00% ID/g and significantly lower clearance than any other

formulation tested, with 15.20% ID/g remaining in circulation 24 hours post-injection. The SPIO nanoparticle had tumor delivery and blood circulation times comparable to the studies in the previous chapter. The polymersome and liposome yielded lower tumor delivery (0.35% ID/g and 1.00% ID/g, respectively), and correspondingly, faster blood clearance.

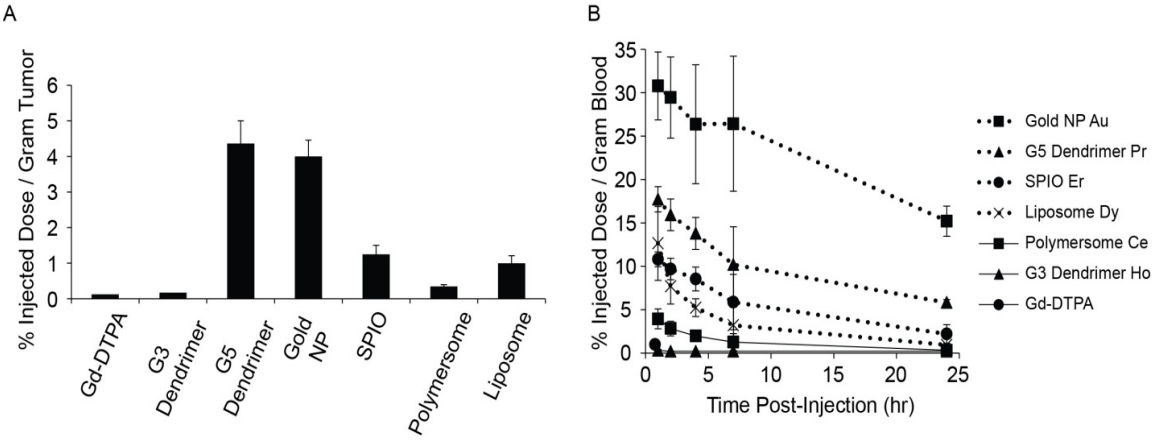


**Figure 3.3** ICP-MS multiplex analysis of biodistribution and blood clearance for seven different compounds injected simultaneously. (A) Tumor delivery and (B) blood clearance profiles for a variety of lanthanide doped nanoparticle formulations, spanning a range of sizes, including small molecules, dendrimers, gold nanoparticles, SPIO nanoparticles, polymersomes, and liposomes.

The small molecule Gd-DTPA and the G3 dendrimer both had undetectable tumor delivery at 24 hours post-injection and had been cleared from circulation in the first hour post-injection. This is consistent with previous reports of G3 dendrimer's rapid clearance.[19] Since both of these formulations are less than 5 nm in diameter, they are efficiently removed from circulation by renal filtration, and while they may display dynamic wash-in at the tumor site, their small size allows for efficient wash-out and, subsequently, poor tumor delivery at the 24 hour time point.

It has been reported that G5 dendrimer exhibits a significantly longer circulation time compared to G3,[20] as the G5 dendrimer's small increase in size begins to impair renal filtration. In this study, the addition of the chelator DOTA, and surface modification with succinate (to neutralize the positive charge of a native PAMAM dendrimer) also contributes to increased size for the G5 formulation. The long circulation time observed in this study, and consequent high tumor delivery, was likely due to the formulation being too large for renal clearance, but still being small enough to avoid significant RES interaction.

The PEG-coated gold nanoparticle also exhibited very long circulation time and high tumor delivery. This was not unexpected since a PEG coating often confers "stealth" properties to nanoparticles[21] and many gold nanoparticle formulations have been reported to have relatively long circulation times.[22] The ≈ -20 mV, ≈ 30 nm SPIO demonstrated similar clearance and tumor delivery as it did in the previous experimental cohorts. Compared to the SPIO nanoparticles, the liposome and polymersome each displayed more rapid clearance and, consequently, lower tumor delivery.

*Validation of Multiplex Approach across Multiple Experimental Cohorts*

A central assumption for all of the multiplex injection experiments is that the different nanoparticle formulations do not interact with each other, so that tumor delivery, biodistribution, and blood clearance observed in a multiplex injection are the same as they would be if each formulation were injected separately. The experimental cohorts used in this investigation, as well as the previous chapter, were specifically designed to test and validate this assumption (see table 3.3). A specific form of SPIO nanoparticle (≈

30 nm hydrodynamic diameter and ≈ -20 mV zeta potential, represented with bold text in table 3.3) was present in the multiplex injection of 3 different animal cohorts (negative zeta potential, size, and additional platforms), allowing for comparison of clearance and tumor delivery for this nanoparticle across a range of injection conditions. It should be noted that the zeta potential reported for the SPIO nanoparticle in Table 3.2 (-9.55 mV) was measured in isotonic phosphate buffered saline; zeta potential measured in 10 mM HEPES yielded ≈ -20 mV. Also, this formulation of SPIO was injected alone, in order to explicitly compare tumor delivery and clearance to the values obtained in the different multiplex injections.

**Table 3.3** Summary of animal injection groups from this and previous chapter that all contain a specific SPIO formulation (n=3 for all groups).

| **Experimental Cohort** | **Number of Particles Co-injected** | **Description** |
|---|---|---|
| Single Particle | 1 | **-20.8 mV, 29.8 nm SPIO** |
| Negative Zeta Potential | 3 | **-20.8 mV**, -12.2 mV, -5.2 mV SPIO (**all ≈ 28 nm**) |
| Size | 3 | 15.52 nm, **29.05 nm**, 70.72 nm SPIO (**all ≈ -20 mV**) |
| Additional Platforms | 7 | Gd-DTPA, G3 and G5 dendrimers, AuNP, **33 nm, ≈ -20 mV SPIO**, liposome, polymersome |

The tumor delivery of this SPIO formulation conserved across animal cohorts is summarized in Figure 3.4. For each injection condition tested, the tumor delivery was very similar (1.09 – 1.29 % ID/g), and no two conditions were statistically different (P values ranging from 0.33 to 0.85).

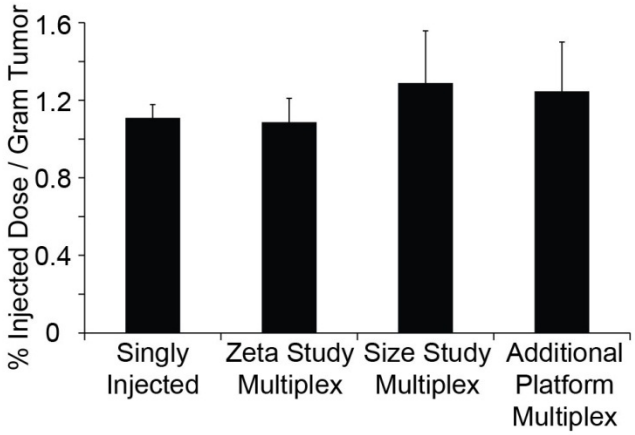


**Figure 3.4** Comparison of tumor delivery of a single SPIO nanoparticle formulation (≈ 29 nm, ≈ -20 mV) that was injected across multiple studies. No statistical difference is found between tumor delivery obtained when the same SPIO formulation is injected alone, with SPIO of other charges, with SPIO of other sizes, or with various other nanoparticle platforms.

Blood circulation profiles are compared in Figure 3.5; again, the four injection conditions tested resulted in similar clearances, with overlapping error bars.

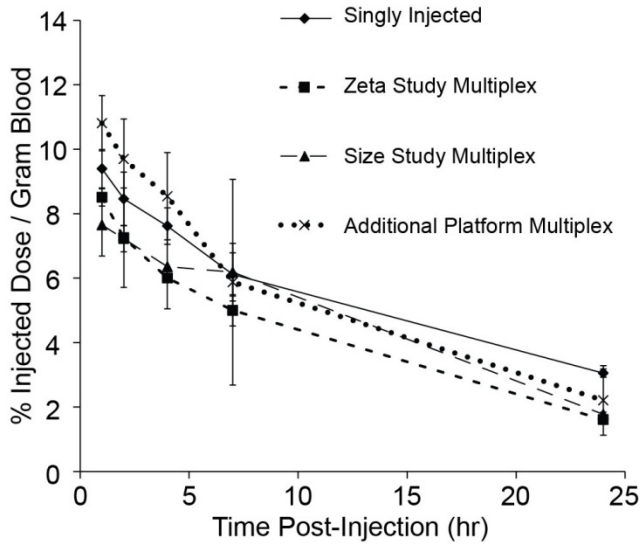


**Figure 3.5** Validation of the ICP-MS multiplex method by comparing blood clearance of a single SPIO nanoparticle formulation (≈ 29 nm, ≈ -20 mV) injected alone, with SPIO of other charges, with SPIO of other sizes, or with various other nanoparticle platforms.

As previously stated, in order for the ICP-MS multiplex method to provide reliable data, it is important that the particular formulations that are co-injected together do not exhibit interactions with each other, so that in the co-injection they behave as they otherwise would if injected alone. In general, three potential sources of nanoparticle interaction should be considered: hydrophobic interactions, electrostatic interactions, and molecular specific interactions. For this particular investigation, all nanoparticle formulations possessed a significantly hydrophilic surface, and no nanoparticles possessed any specific ligands or receptors. In order to avoid electrostatic interactions, when the effect of nanoparticle surface charge was evaluated, the study was split into two separate injections (one with the three negatively charged particles, and one with the three positively charged particles). It is also worth noting that at no time, for any of the experimental groups, was any aggregation visibly observed when the individual formulations were combined to form the multiplex solution. Given that each nanoparticle would be “multivalent” for any possible type of interaction, macroscopic aggregation or precipitation would be expected if nanoparticle interaction had occurred.

## 3.5 Conclusion

In addition to precipitating lanthanide metals into the core of SPIO nanoparticles, it is also possible to incorporate lanthanides into liposomes, polymersomes, and dendrimeric formulations using either encapsulation or chelation. Therefore, it is envisioned that any nanoparticle formulation amenable to labeling with a metal radionuclide would also be suitable for labeling with an ICP-MS lanthanide tracer. Some other types of nanoparticles (*e.g.* gold and silver nanoparticles) inherently contain an ICP-MS metal tracer, without any further need for labeling. In addition to providing a quantitative method of detection with high sensitivity, ICP-MS tracers provide two potential befits over conventional radiolabeling. Namely, they have the ability to easily multiplex a large number of signals in a single fluid or tissue sample while avoiding the hazards of handling radioactivity. Consequently, ICP-MS based multiplex analysis can be applied to a very wide variety of nanoparticle and macropharmaceutical formulations and allows for “higher throughput” evaluation of the pharmacokinetics and biodistribution of such agents in animals models.

## 3.6 References


1. Boerman, O. C.; Laverman, P.; Oyen, W. J.; Corstens, F. H.; Storm, G., Radiolabeled liposomes for scintigraphic imaging. *Prog Lipid Res* 2000, 39, 461-75.

2. Kleiter, M. M.; Yu, D.; Mohammadian, L. A.; Niehaus, N.; Spasojevic, I.; Sanders, L.; Viglianti, B. L.; Yarmolenko, P. S.; Hauck, M.; Petry, N. A.; Wong, T. Z.; Dewhirst, M. W.; Thrall, D. E., A tracer dose of technetium-99m-labeled liposomes can estimate the effect of hyperthermia on intratumoral doxil extravasation. *Clin Cancer Res* 2006, 12, 6800-7.

3. Phillips, W. T., Delivery of gamma-imaging agents by liposomes. *Adv Drug Deliv Rev* 1999, 37, 13-32.

4. Cai, W.; Chen, K.; Li, Z. B.; Gambhir, S. S.; Chen, X., Dual-function probe for PET and near-infrared fluorescence imaging of tumor vasculature. *J Nucl Med* 2007, 48, 1862-70.

5. Chen, K.; Li, Z. B.; Wang, H.; Cai, W.; Chen, X., Dual-modality optical and positron emission tomography imaging of vascular endothelial growth factor receptor on tumor vasculature using quantum dots. *Eur J Nucl Med Mol Imaging* 2008, 35, 2235-44.

6. Lee, H. Y.; Li, Z.; Chen, K.; Hsu, A. R.; Xu, C.; Xie, J.; Sun, S.; Chen, X., PET/MRI dual-modality tumor imaging using arginine-glycine-aspartic (RGD)-conjugated radiolabeled iron oxide nanoparticles. *J Nucl Med* 2008, 49, 1371-9.

7. Chang, C. H.; Stabin, M. G.; Chang, Y. J.; Chen, L. C.; Chen, M. H.; Chang, T. J.; Lee, T. W.; Ting, G., Comparative dosimetric evaluation of nanotargeted (188)Re-(DXR)-liposome for internal radiotherapy. *Cancer Biother Radiopharm* 2008, 23, 749-58.

8. Chen, L. C.; Chang, C. H.; Yu, C. Y.; Chang, Y. J.; Wu, Y. H.; Lee, W. C.; Yeh, C. H.; Lee, T. W.; Ting, G., Pharmacokinetics, micro-SPECT/CT imaging and therapeutic efficacy of (188)Re-DXR-liposome in C26 colon carcinoma ascites mice model. *Nucl Med Biol* 2008, 35, 883-93.

9. Li, L.; Wartchow, C. A.; Danthi, S. N.; Shen, Z.; Dechene, N.; Pease, J.; Choi, H. S.; Doede, T.; Chu, P.; Ning, S.; Lee, D. Y.; Bednarski, M. D.; Knox, S. J., A novel antiangiogenesis therapy using an integrin antagonist or anti-Flk-1 antibody coated 90Y-labeled nanoparticles. *Int J Radiat Oncol Biol Phys* 2004, 58, 1215-27.

10. Emfietzoglou, D.; Kostarelos, K.; Sgouros, G., An analytic dosimetry study for the use of radionuclide-liposome conjugates in internal radiotherapy. *J Nucl Med* 2001, 42, 499-504.

11. Chang, M. Y.; Seideman, J.; Sofou, S., Enhanced loading efficiency and retention of 225Ac in rigid liposomes for potential targeted therapy of micrometastases. *Bioconjug Chem* 2008, 19, 1274-82.

12. Sofou, S.; Kappel, B. J.; Jaggi, J. S.; McDevitt, M. R.; Scheinberg, D. A.; Sgouros, G., Enhanced retention of the alpha-particle-emitting daughters of Actinium-225 by liposome carriers. *Bioconjug Chem* 2007, 18, 2061-7.

13. Ballot, S.; Noiret, N.; Hindre, F.; Denizot, B.; Garin, E.; Rajerison, H.; Benoit, J. P., 99mTc/188Re-labelled lipid nanocapsules as promising radiotracers for imaging and therapy: formulation and biodistribution. *Eur J Nucl Med Mol Imaging* 2006, 33, 602-7.

14. Bao, A.; Goins, B.; Klipper, R.; Negrete, G.; Phillips, W. T., 186Re-liposome labeling using 186Re-SNS/S complexes: in vitro stability, imaging, and biodistribution in rats. *J Nucl Med* 2003, 44, 1992-9.

15. Sun, G.; Xu, J.; Hagooly, A.; Rossin, R.; Li, Z.; Moore, D. A., Strategies for optimized radiolabeling of nanoparticles for in vivo PET imaging. *Adv Mater* 2007, 19, 3157-62.

16. Xu, J.; Sun, G.; Rossin, R.; Hagooly, A.; Li, Z.; Fukukawa, K. I.; Messmore, B. W.; Moore, D. A.; Welch, M. J.; Hawker, C. J.; Wooley, K. L., Labeling of Polymer Nanostructures for Medical Imaging: Importance of crosslinking extent, spacer length, and charge density. *Macromolecules* 2007, 40, 2971-2973.

17. Bourrinet, P.; Bengele, H. H.; Bonnemain, B.; Dencausse, A.; Idee, J. M.; Jacobs, P. M.; Lewis, J. M., Preclinical safety and pharmacokinetic profile of ferumoxtran-10, an ultrasmall superparamagnetic iron oxide magnetic resonance contrast agent. *Invest Radiol* 2006, 41, 313-24.

18. Turkevich, J.; Stevenson, P. C.; Hillier, J., A study of the nucleation and growth processes in the synthesis of colloidal gold. *Discuss Faraday Soc* 1951, 11, 55-75.

19. Kobayashi, H.; Kawamoto, S.; Jo, S. K.; Bryant, H. L., Jr.; Brechbiel, M. W.; Star, R. A., Macromolecular MRI contrast agents with small dendrimers: pharmacokinetic differences between sizes and cores. *Bioconjug Chem* 2003, 14, 388-94.

20. Sato, N.; Kobayashi, H.; Hiraga, A.; Saga, T.; Togashi, K.; Konishi, J.; Brechbiel, M. W., Pharmacokinetics and enhancement patterns of macromolecular MR contrast agents with various sizes of polyamidoamine dendrimer cores. *Magn Reson Med* 2001, 46, 1169-73.

21. Jokerst, J. V.; Lobovkina, T.; Zare, R. N.; Gambhir, S. S., Nanoparticle PEGylation for imaging and therapy. *Nanomedicine (Lond)* 2011, 6, 715-28.

22. De Jong, W. H.; Hagens, W. I.; Krystek, P.; Burger, M. C.; Sips, A. J.; Geertsma, R. E., Particle size-dependent organ distribution of gold nanoparticles after intravenous administration. *Biomaterials* 2008, 29, 1912-9.

# Chapter 4: Extension of ICP-MS Multiplex Method to Compare Actively Targeted SPIO Nanoparticles

## 4.1 Abstract

Given the rapidly expanding library of pathology biomarkers (*e.g.* tumor receptors) and targeting scaffolds (*e.g.* antibodies, single chain antibody fragments, small affinity peptides, *etc.*), the number of actively targeted nanoparticle formulations is growing exponentially. In most studies, the goal is to maximize the concentration of diagnostic or therapeutic nanoparticle payload delivered to a site of interest *in vivo*, while minimizing delivery in other locations. Given the difficulty and expense of *in vivo* animal testing, it is generally not feasible to examine a large number of specific nanoparticle candidates *in vivo*. This often leads to the investigation of only the single formulation that performed best *in vitro*. However, nanoparticle delivery *in vivo* is dependent on many variables, many of which cannot be adequately assessed with *in vitro* cell-based assays. Consequently, the development of actively targeted nanoparticles could be greatly facilitated and expedited by a method that allows for many formulations (including control formulations) to be evaluated in a single animal. It is hypothesized that the ICP-MS multiplex approach developed in chapters 2 and 3 to examine passive nanoparticle delivery could be naturally extended to fill this role.

## 4.2 Introduction

Rapid advancements in nanotechnology have resulted in the development of nanoparticle formulations for a myriad of biological applications extending from diagnostic cell tracking to improved delivery of therapeutic agents. Given the limitless ability to modify the physicochemical properties of nanoparticles to fit specific areas of interest, it is expected that their utility will only continue to increase. Recently, there has been especially significant growth in the application of nanoparticles to cancer diagnostics and drug delivery. This growth is a direct result of the numerous advantages that nanoparticles provide to this field; including, but not limited to: the ability of nanoparticles to extravasate at a tumor, the high therapeutic and diagnostic "payloads" that can be incorporated into nanoparticles, and their favorable toxicity profiles resulting from reduced agent accumulation in healthy tissue.[1-3]

So far, the majority of clinical trials for nanoparticles have focused on passive delivery to the tumor. That is, a nanoparticle's physicochemical properties are optimized for long blood residence time, which allows for a high percentage of uptake into tumors via the enhanced permeability and retention (EPR) effect.[4] While this strategy has demonstrated that nanoparticle-encapsulated drug has improved efficacy and reduced side-effects (compared to free drug), an increased focus has recently been placed on further improving these nanoparticles with active targeting strategies. Indeed, many studies have shown that active targeting of nanoparticles can increase the dose of therapeutic delivered to a tumor and also improve the intra-tumoral localization of delivered nanoparticles.[5, 6] Furthermore, a nanoparticle's surface may display multiple copies of a particular targeting ligand (multivalency), and this has been shown to increase

binding avidity, increase the rate of internalization, and ultimately improve therapeutic efficacy and/or image contrast.[7-11]

One particular class of nanoparticles that has become increasingly dependent on targeted delivery is superparamagnetic iron oxide (SPIO) nanoparticles (NPs). SPIO NPs are an attractive magnetic resonance (MR) contrast agent, providing T2*-weighted contrast enhancement in MR imaging applications. Due to their good biocompatibility, strong contrast enhancement, and their ability to generate functional data concomitant with anatomic information, SPIO are avidly being evaluated as molecular imaging agents. In this role, they are used to report the expression level of target cell-surface receptors in order to improve the specificity of disease detection. To date, affinity ligands have been used to deliver SPIO NPs to a range of different sites including tumor cells,[12,13] tumor vasculature,[14,15] atherosclerotic lesions,[16-18] and many others.[19-24] However, while SPIO NPs have seen extensive biological applications, their full transition to the clinic as molecular imaging agents has been slow to develop, due to the relatively high concentrations of SPIO NPs needed to generate detectable MR contrast in an area of interest.

Often, pathologies present with several possible biomarkers that may be viable targets. For example, breast cancers may overexpress the estrogen receptor, progesterone receptor, and/or the Her2/neu (ErbB2) receptor.[25] As nanoparticles continue to progress toward greater clinical use, it is important to identify which molecular targets result in the best *in vivo* tumor delivery (for a particular tumor type). Importantly, the optimal molecular target and nanoparticle composition for nanoparticle delivery *in vivo* may not be accurately reflected in assays conducted *in vitro*. For example, it has been shown that

affinity ligands with very high affinity do not necessarily result in the best tumor targeting, since tight binding at the tumor periphery slows diffusion of the agent within the tumor and can block extravasation of additional agent.[26] Furthermore, the addition of targeting ligands to a nanoparticle's surface can alter its physicochemical properties, thus potentially altering its circulation properties and affecting its ability to reach a tumor.

Despite the large potential for incongruity between nanoparticle performance *in vitro* and *in vivo*, most often investigators choose the identity of the active targeting ligand and then optimize the ligand surface density, along with other nanoparticle physicochemical properties, based on *in vitro* data. Subsequently, this "optimal" formulation is generally evaluated in one cohort of subjects, while one or more negative control (non-targeted) nanoparticle formulations are examined in other cohorts. However, when nanoparticles are evaluated in separate animal cohorts, the large animal-to-animal variability characteristic of *in vivo* studies makes nanoparticle improvement more difficult to observe. The primary reason for the lack of optimization at the *in vivo* stage, and the use of a large number of animals, is the lack of a feasible "higher throughput" method for accurately comparing different nanoparticles *in vivo.* In chapters two and three, we introduced a non-radiative, quantitative, and multiplex method for assessing nanoparticle pharmacokinetics and biodistribution, demonstrating its ability to compare passive delivery for a wide range of nanoparticle types and physicochemical properties. Herein, this method is extended to include the evaluation of actively targeted SPIO NPs.

For this work, we have selected three targets of interest: the HER2/neu receptor, heat shock protein 47 (HSP47) and $\alpha_V\beta 3$ integrin. Each of these receptors has been shown to have a high association with cancer, and each has been used as a target in therapeutic

studies.[27-30] Additionally, each of these targets has ligands that can be used to actively target SPIO NPs. Specifically, HER2 affibody, cyclic RGD, and the LDS affinity peptide were selected as ligands for targeting HER2/neu, αvβ3 integrin, and HSP47 respectively.[31-36] As described in chapter 2, a set of four lanthanide-doped SPIO nanoparticles (Ho, Sm, Gd, and Eu) were synthesized. HER2 affibody, cyclic RGD, and LDS peptide were conjugated to the Ho-, Sm-, and Gd-SPIO, respectively. The Eu-SPIO lacked a targeting ligand and served as a negative control nanoparticle formulation. ICP-MS multiplex analysis can then be used to trace each actively targeted formulation simultaneously in a single sample.

## 4.3 Materials and Methods

*Materials*

Azido-dPEG$_4$-NHS ester was purchased from Quanta BioDesign Ltd. (Powell, OH). NIH/3T3 cells that were engineered to stably express the Her2/neu receptor (T6-17) were kindly provided by Dr. Mark Greene, MD/PhD (University of Pennsylvania). All other reagents were purchased from Thermo Fisher Scientific (Waltham, MA) unless otherwise noted.

*Synthesis of Dextran Stabilized Lanthanide Doped SPIO*

Dextran coated, lanthanide doped, SPIO nanoparticles were prepared though the coprecipitation of ferrous, ferric, and lanthanide ions in the presence of dextran [37]. Briefly, 25 g of dextran T-10 (Pharmacosmos A/S, Holbaek, Denmark), was dissolved in 500 mL d$H_2O$ and heated to 80°C for 1 hour. The solution was then allowed to cool to

room temperature and continued to mix overnight. Subsequently, a solution of 1.85 g $FeCl_3$, 0.73 g $FeCl_2$, and 0.125 g $LnCl_3 \cdot 6H_2O$ (Ln = Ho, Eu, Sm, or Gd) in 25 mL $dH_2O$ was prepared and decanted into the dextran solution. The combined solution was cooled on ice and degassed with $N_2$ for 90 min. While keeping the solution stirring on ice and under $N_2$, an automated syringe pump was then used to introduce 15 mL of concentrated $NH_4OH$ to the solution over 5 hours. The resulting black viscous solution was removed from the $N_2$ atmosphere, heated to 90°C for 1 hour, cooled overnight, and centrifuged at 20,000 RCF for 30 minutes to remove large aggregates. Free iron, lanthanide, and dextran were removed by diafilitration across a 100 kDa membrane and the Ln-SPIO were brought to a final volume of ≈40 mL at 10 mg Fe/mL.

This 40 mL of dextran SPIO at an iron concentration of 10 mg/mL was then combined with an equal volume of 10 M NaOH and mixed for 10 minutes. 80 mL of epichlorohydrin was then added and the solution was vigorously stirred at room temperature overnight. Epichlorohydrin crosslinks the dextran coating within the Ln-SPIO particle and chemically activates the dextran surface for conjugation. The solution was then briefly centrifuged to allow phase-separation into an aqueous black SPIO layer and a clear layer of unreacted epichlorohydrin, which was removed. The SPIO layer was quickly purified via extraction in isopropanol. Specifically, the Ln-SPIO material was combined with 5 volumes of isopropanol and the mixture was vigorously shaken. Brief centrifugation of the mixture resulted in a layer of precipitated salt, an Ln-SPIO layer, and an isopropanol layer (containing any remaining epichlorohydrin). The SPIO layer was then isolated and combined with an equal volume of concentrated $NH_4OH$ and gently stirred for 24 hours at room temperature, resulting in an aminated nanoparticle

surface. After the reaction, the Ln-SPIO was purified by diafiltration across a 100 kDa membrane and was 0.2 μm filtered to remove any oversized material. Finally, to ensure complete purification of the Ln-SPIO from excess salt and lanthanide ions, the nanoparticles were magnetically purified on MACS LS columns using a MidiMACS magnet (Miltenyi Biotec, Auburn, CA, USA).

*Cloning of HER2-Affibody and LDS Recombinant Protein into pTXB1 Vector*

The nucleotide and corresponding amino acid sequences for the HER2 affibody and LDS affinity peptide are provided in Figures 4.1 and 4.2, respectively. Complementary oligonucleotides comprising the HER2-Affibody or LDS coding sequence flanked at both ends by 15 base sequences homologous to the desired restriction sites of the destination vector were ordered from Integrated DNA Technologies (Coralville, IA). To improve subsequent affinity column cleavage, an additional 9 base pairs encoding a "MRM" amino acid sequence were included in the oligonucleotides at the C-terminal end of both sequences. The full nucleotide and amino acid sequence for the HER2-Affibody and AHNP can be found in Figure x. Oligonucleotides were incubated together at a final concentration of 5 μM and hybridized at room temperature for 30 minutes. The resulting sequence was agarose gel purified and directly ligated with gel-purified *Nde*I-*Xho*I double digested pTXB1 vector (New England Biolabs, Inc) via the CloneEZ kit (Genscript). Insertion of the HER2-Affibody and AHNP sequences was verified by DNA sequencing using the T7 promoter as the sequencing primer.

GTG GAT AAC AAA TTT AAC AAA GAA ATG CGC AAC GCG TAT TGG GAA ATT
Val Asp Asn Lys Phe Asn Lys Glu Met Arg Asn Ala Tyr Trp Glu Ile

GCG CTG CTG CCG AAC CTG AAC AAC CAG CAG AAA CGC GCG TTT ATT CGC
Ala Leu Leu Pro Asn Leu Asn Asn Gln Gln Lys Arg Ala Phe Ile Arg

AGC CTG TAT GAT GAT CCG AGC CAG AGC GCG AAC CTG CTG GCG GAA GCG
Ser Leu Tyr Asp Asp Pro Ser Gln Ser Ala Asn Leu Leu Ala Glu Ala

AAA AAA CTG AAC GAT GCG CAG GCG CCG AAA **ATG CGC ATG**
Lys Lys Leu Asn Asp Ala Gln Ala Pro Lys **Met Arg Met**

**Figure 4.1** Nucleotide and corresponding amino acid sequence of the HER2-Affibody. The additional base pairs added to improve affinity column cleavage are shown in bold.

CTG GAT AGC CGC TAT AGC CTG CAG GCG GCG ATG TAT **ATG GCG ATG**
Leu Asp Ser Arg Tyr Ser Leu Gln Ala Ala Met Tyr **Met Arg Met**

**Figure 4.2** Nucleotide and corresponding amino acid sequence of the LDS peptide. The additional base pairs added to improve affinity column cleavage are shown in bold.

*Expression and Purification of HER2-Affibody and LDS Recombinant Protein*

The pTXB1-HER2-Affibody vector was transformed in Rosetta™ 2(DE3)pLysS Competent Cells (Novagen). Bacterial cell cultures were initially grown overnight in an air shaker (225 rpm) at 37 °C in 3 mL of LB medium. Cultures were scaled up to fifty mL of LB medium and grown overnight under the same conditions, and then inoculated into 1 L LB containing 50 mg/L of ampicillin. At $OD_{600\ nm}$ = 0.6, IPTG was added at a final concentration of 0.5 mM to induce T7 RNA polymerase-based expression. Cultures were allowed to express for 2 hours at 37 °C. Bacterial cultures were centrifugally pelleted at 10,000 x g for 5 minutes, resuspended in 5 mL of column buffer (20 mM Na-

HEPES, 0.5 M NaCl, 1 mM EDTA, pH 8.5) containing 0.75 g/L lysozyme and 50 mM phenylmethylsulfonyl fluoride. Cells were lysed by pulse sonication on ice. Cells were centrifuged at 15,000 g for 30 minutes at 4 °C. Supernatant was collected and stored at -20 °C. For the following purification steps, all procedures were run at 4 °C. One mL of the supernatant was incubated for 10 minutes in a 10 mL Poly-Prep chromatography column (Bio-Rad, Hercules, CA) packed with 1 mL of chitin beads (New England Biolabs, Inc). Supernatant was allowed to pass through the column and chitin beads were washed with 50 mL of column buffer at a flow rate of approximately 2 mL/min. Three mL of 50 mM MESNA was quickly passed through the column in order to evenly distribute the MESNA throughout the chitin beads, and flow was stopped. The column was incubated for 16 hours at 4 °C. HER2-Affibody proteins, now containing a C-terminal thioester, were eluted from the column in a total 4 mL buffer (0.1 M Tris-HCl, pH 8.5) and concentrated to a volume of 500 μL using an Ultracell 3,000 (Millipore, Billerica, MA). An analogous experimental protocol was used for the production and purification of LDS peptides, with the exception of the IPTG concentrations used for induction, which were lowered from 0.5 mM to 0.4 mM final concentration.

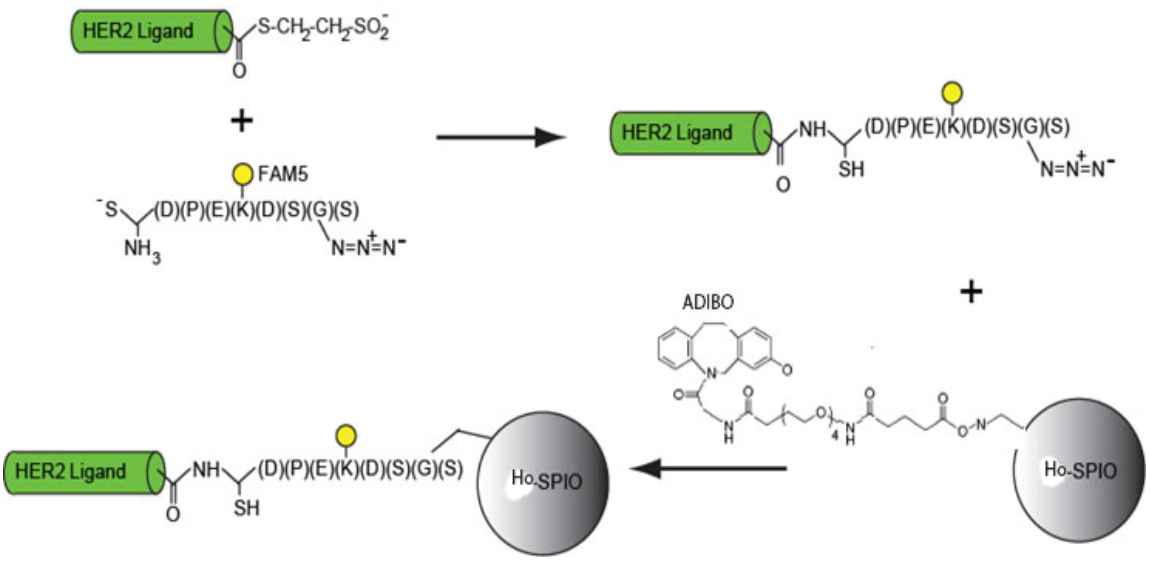


**Figure 4.3** Schematic of EPL-Click conjugation strategy, illustrated with HER2 affibody conjugation to Ho-SPIO. Upon cleavage from the chitin affinity purification column, the HER2 affibody displays a C-terminal reactive thioester. This C-terminal thioester reacts with the N-terminal cysteine of a fluorescent linker peptide (AFP). Towards the C-terminus of the linker peptide is an azide group. Subsequently a chemoselective "click" reaction is carried out between Ho-SPIO displaying alkyne functional groups (ADIBO) and the azide group of the HER2-linker adduct.

*Expressed Protein Ligation*

Expressed protein ligation was carried about between the thioester containing HER2-Affibody/LDS peptide and an azido-fluorescent peptide (AzFP) with an N-terminal cysteine. The sequence of the AzFP was $NH_2$-CDPEK(5-FAM)DSGK(N3)S-OH. The K(5-FAM) represents a lysine with a fluorescein covalently attached to its ε-amino group and the K(N3) represents a lysine with an azido group attached to its ε-amino group. The AzFP (0.1 mM) was incubated with approximately 0.01 mM HER2-

Affibody or LDS. The EPL reaction was mixed overnight at room temperature. For the HER2-Affibody, the EPL product and excess AzFPs were separated on a Superdex 30 chromatography column. For the LDS-peptide, several rounds of washing using Ultracell 3,000 filtration columns were used to remove unreacted AzFP peptides.

*Azide functionalization of Cyclic-RGD*

Cyclic-RGD was incubated with Azido-dPEG12-NHS at 10:1 molar ratios of Azide:RGD in DMSO at a final volume of 30 µL. Reactions were incubated at room temperature overnight and purified via RGD precipitation in 10x volumes of tert-butyl methyl ether followed by centrifugation at 16,000x g for 1 minute. These precipitations were performed in triplicate and the resulting conjugate was suspended in a final volume of 30 µL DMSO.

*ADIBO Modification of SPIO NPs for Click Chemistry*

Surface amines on SPIO NPs were reacted with the amine-reactive ADIBO-dPEG$_4$-NHS in 0.1 M sodium phosphate buffer, pH 9. ADIBO is an alkyne-containing moiety suitable for click conjugation to the azide-containing ligand preparations. Specifically, a 138 mM stock of ADIBO-dPEG$_4$-NHS was diluted 100-fold into a 50 µM solution of SPIO NPs. All nanoparticle solutions were mixed overnight at room temperature. SPIO NPs were purified via superdex 200 chromatography columns (GE Healthcare, Piscataway, NJ). The resulting ADIBO-SPIO NPs were incubated with 100 times molar excess of succinic anhydride to convert all remaining amines to carboxyl groups. ADIBO-SPIO NPs were subsequently purified on superdex200 chromatography

columns, equilibrated with PBS. For RGD-SPIO and unlabeled SPIO used in flow cytometry experiments, SPIO NPs were first labeled with a FITC fluorophore (10:1 molar ratio of FITC:SPIO) and purified via PD-10 purification columns before being labeled with ADIBO.

*Copper-Free Click Conjugation*

ADIBO-SPIO NPs (1 mg/mL) were mixed with fixed concentrations of HER2-AzFP ligand (2.5 20 µM) and LDS-AzFP (30 µM) in PBS, pH 7.4 at a final volume of 100 µL. For RGD-N3, 60 µM of the peptide was incubated with ADIBO-SPIO NPs (1 mg/mL) in a final volume of 100 µL. Reactions were mixed overnight at room temperature and then purified on Superdex 200 chromatography columns equilibrated with PBS.

*Nanoparticle Physicochemical Characterization*

Stock samples of Ln-SPIO nanoparticles were diluted into pH 7.4 phosphate buffered saline for determination of the hydrodynamic diameter by dynamic light scattering (DLS) both before and after conjugation to active targeting ligands. Measurements were acquired with a Zetasizer Nano-ZS (Malvern Instruments, Worcestershire, UK) using the non-invasive back-scatter (NIBS) mode. For zeta potential measurements, stock samples of Ln-SPIO were diluted into phosphate buffered saline at pH 7.4 and then mean nanoparticle zeta potential was measured, both before and after conjugation to targeting ligands, using a Zetasizer Nano-ZS. For Ln-SPIO nanoparticles,

the transverse ($r_2$) and longitudinal ($r_1$) relaxivities were measured using a Bruker mq60 tabletop MR relaxometer operating at 1.41 T (60 MHz).

*Cell Culture*

T6-17 murine fibroblasts (a derivative of the NIH/3T3 line and kindly provided by Mark Greene, PhD, FRCP, University of Pennsylvania) and HeLa cells (purchased from ATTC) were cultured and maintained in Dulbecco's modified Eagle's medium (DMEM), supplemented with 10% fetal bovine serum (FBS), 1% penicillin/streptomycin at 37°C and 5% $CO_2$.

*Western Blots*

T6-17 and HeLa cells were grown to 80% confluence on 10 cm plate. The plate was washed twice with PBS and then incubated on ice for five minutes in 1mL RIPA Buffer (Sigma-Aldrich) supplemented with 6M urea. Cells were scraped off the plate and clarified by centrifugation. 47 mg of solid tumor was solubilized in 3mL Western Lysis Buffer (12.5mM Tris, 4% SDS, pH 8) with a mortar and pestle. Lysate was boiled for 30min and clarified by centrifugation. Total protein concentrations were determined by BCA Assay (Pierce). Concentrations of Hsp47, integrin, and ErbB2 were quantified by Western blot. Specifically, 12.5 uL of each sample was loaded into an Any kD TGX gel (Bio-Rad) along with four 1:3 serial dilutions. These were quantified on the LiCor Odyssey and compared against a standard curve ranging from 800 ng to 10 ng of purified Hsp47 (AbCam), Integrin $\alpha_V\beta_3$ (R&D Systems), or ErbB2 (OriGene).

*Flow Cytometric Analysis*

Cells (T6-17s or HeLas) were dissociated from culture flasks using PBS-based enzyme free dissociation buffer and transferred to sterile 96-well plates at a final concentration of 50,000 cells per well. Targeted SPIO conjugates were added to the wells for 30 minutes at 37°C at a final concentration 75 µg Fe/mL. Cells were transferred to 1.5 mL centrifuge tubes and washed in triplicate by pelleting cells at 1000 RCF for 3 minutes and then resuspending in PBS. Cells were resuspended in 250 µL of PBS and transferred to a 96-well plate (50,000 cells per well) and analyzed using a Guava Easycyte Plus system (Guava Technologies, Hayward, CA). Flow cytometry data were analyzed using *FlowJo* software (TreeStar Inc., San Francisco, CA).

*Cell Relaxation Studies*

T6-17 and HeLa cells were dissociated using PBS-based enzyme free dissociation buffer and transferred to sterile 48-well plates at a concentration of $3 \times 10^6$ cells per well. Actively targeted SPIO conjugates and unlabeled SPIO were incubated with these cells in the 48-well plate at a final concentration of 75 µg Fe/mL for 1 hour at 37°C (n=3 for each targeting agent). Cells were transferred to 1.5 mL centrifuge tubes and washed in triplicate by pelleting cells at 1,000 RCF for 3 minutes and then resuspending in PBS. Cells were suspended in a final volume of 300 µL PBS and T2 measurements were taken using the benchtop relaxometer. The reciprocal of the T2 relaxation time constant, which represents the MR signal of the cell pellet, was calculated, and the reciprocal of the T2 for cells incubated without nanoparticles (background) was subtracted off. Finally, since each Ln-SPIO formulation has a different R2 relaxivity value, the MR signal for each cell

pellet was normalized by dividing by the R2 value of the particular Ln-SPIO used, resulting in a metric that is proportional to nanoparticle cellular association.

*In Vitro ICP-MS Multiplex Assessment of Cell Labeling*

T6-17 and HeLa cells were dissociated and incubated with actively targeted SPIO conjugated and unlabeled SPIO in the same manner as in previous the cell relaxation studies, with the notable exception that all SPIO formulations were incubated together with cells, rather than each SPIO formulation being incubated separately. Following washing to remove unbound nanoparticles, the pellet was resuspended in 100 μL of PBS. The lanthanide concentration of Ho, Sm, Gd, and Eu was then determined in each pellet and compared to the concentration present in the incubating medium. Data are plotted as the ratio of $[Ln]_{pellet}$ / $[Ln]_{incubation\ medium}$.

*In Vivo Studies*

Approximately 6-week old female nu/nu nude mice (Charles River Laboratory, Charles River, MS, USA) were maintained in accordance with the Institutional Animal Care and Use Committee of the University of Pennsylvania. Mice were anesthetized via isoflurane and T6-17 cells were injected subcutaneously into the back right flank ($2 \times 10^6$ cells in 0.2 mL PBS). Tumors were grown until the diameter was approximately 8 mm. Ln-SPIO (Ho, Gd, Sm, and Eu) were pooled and injected intravenously at a dose of 3.75 mg Fe / kg body weight. Prior to injection, an aliquot was saved for ICP-MS determination of lanthanide concentration in injected material. 24 hours after nanoparticle injection, the animals were sacrificed and the tumors were excised. For each nanoparticle

formulation, the tumor delivery was calculated as a percent injected dose per gram of tissue as $[Ln]_{tumor}$ / ($[Ln]_{inj}$*$M_{inj}$), where $[Ln]_{tumor}$ is the lanthanide concentration in the tumor, $[Ln]_{inj}$ is the lanthanide concentration in the injected nanoparticle solution, and $M_{inj}$ is the mass of nanoparticle solution injected (0.2 grams). For evaluation of "base" nanoparticles prior to ligand conjugation, one way ANOVA analysis was used to assess similarity in tumor delivery for the different Ln-SPIO.

## 4.4 Results and Discussion

*Nanoparticle Physicochemical Characterization*

Because the size of a nanoparticle formulation influences its pharmacokinetics and biodistribution, as examined in chapter 2, it was important to ensure that the four Ln-SPIO formulations exhibit very similar size profiles prior to targeting ligand conjugation. Therefore, the hydrodynamic diameter of each Ln-SPIO formulation was determined by DLS prior to conjugation of active targeting ligands. It was found that the peak of the distribution lay between 27.00 nm and 29.07 nm for all four formulations (Table 4.1). Furthermore, the size distributions have a very high degree of overlap (Figure 4.4), suggesting that the "base" nanoparticles to which the active targeting ligands were attached are very similar populations.

**Table 4.1** Physicochemical properties (hydrodynamic diameter and zeta potential) of Ln-SPIO formulations before and after conjugation to targeting ligands. Relaxivity values were measured prior to conjugation and assumed to be unaffected to conjugation.

| Dopant | Ligand | Pre-Conj. Size nm | Post-Conj. Size nm | Pre Conj. Zeta mV | Post Conj. Zeta mV | R1 | R2 |
|---|---|---|---|---|---|---|---|
| **Eu** | None | 27.00 | 33.54 | -5.63 | -10.01 | 6.2 | 262.9 |
| **Ho** | HER2-Aff | 28.07 | 33.47 | -4.47 | -10.53 | 10.3 | 135.2 |
| **Sm** | RGD | 27.77 | 35.57 | -6.09 | -6.48 | 9.2 | 158.5 |
| **Gd** | LDS | 29.07 | 34.84 | -5.77 | -8.61 | 8.1 | 172.6 |

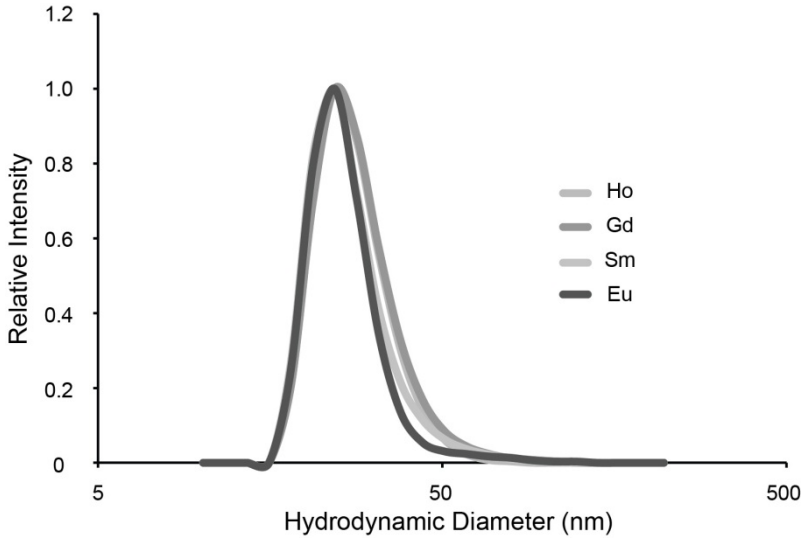


**Figure 4.4** Dynamic light scattering profiles of Ho, Gd, Sm, and Eu doped SPIO nanoparticles, prior to conjugation with any targeting ligands.

The hydrodynamic diameter of each formulation was subsequently rechecked after conjugation of active targeting ligands (Figure 4.5). It was found that each formulation increased in size by approximately 5 nm, so that the post-conjugation sizes ranged from 33.54 to 35.57. It is likely that the increase in size is due to the addition of the various functional groups required for conjugation (*i.e.* ADIBO, linker peptide, and targeting ligand itself). Again, as before ligand conjugation, the size profiles showed a

very high degree of overlap, indicating the populations are very similar in size. This means it is unlikely that any difference in nanoparticle pharmacokinetics or biodistribution observed for the actively targeted agents is the result of size alterations secondary to conjugation.

Next, since it is critical for the ICP-MS multiplex method that the co-injected nanoparticles do not associate or aggregate with one another prior to injection (as discussed in chapter 3), DLS measurements were used to rule out the possibility of nanoparticle aggregation. Specifically, all four Ln-SPIO formulations (post-conjugation) were mixed together in equal amounts and allowed to incubate together for one hour. The DLS profile of the mixed solution was then acquired (Figure 4.5). Since the peak size for the mixed sample was 38.15 nm and the distribution was very similar to that of each individual formulation, it was concluded that no significant association or aggregation occurs between the actively targeted formulations prior to injection.

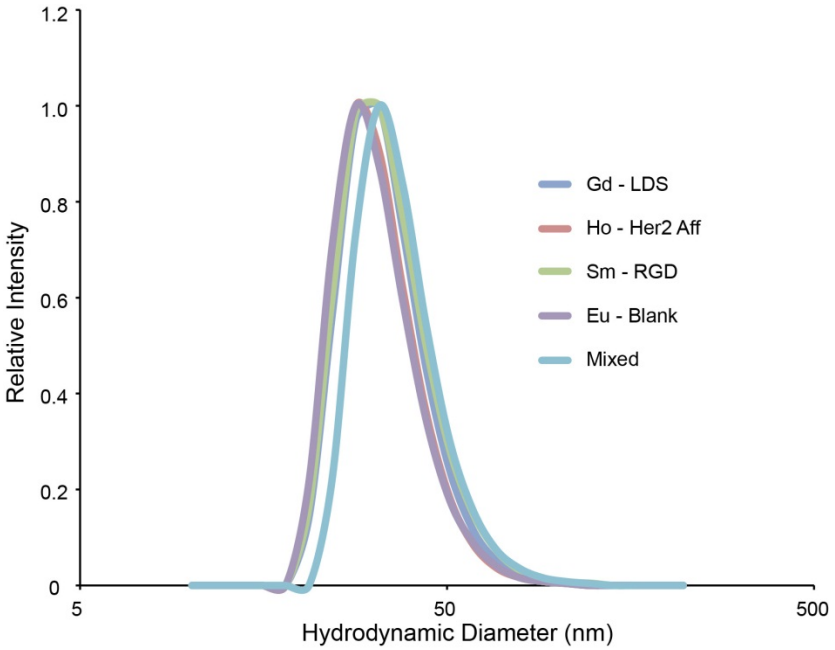


**Figure 4.5** Dynamic light scattering profiles of each nanoparticle formulation after conjugation to its respective targeting ligand. The size profile was also examined in a sample where all formulations were combined into a single sample (mixed).

The zeta potential (surface charge) of a nanoparticle formulation also plays a significant role in the pharmacokinetics and biodistribution of nanoparticle platforms (see chapter 2). Therefore, the zeta potential of each Ln-SPIO was determined both before and after conjugation with active targeting ligands. For the "base" nanoparticles, the aminated nanoparticles (which would display a positive surface charge) were first carboxylated using succinic anhydride in order to generate a negatively charged surface suitable for use in the *in vivo* check on "base" particle similarity (see below). It was found that the carboxylated "base" nanoparticles had zeta potentials ranging from -4.47 mV to -6.09 mV, which were considered to be very close in value. A slightly greater degree of surface charge variation was observed in the nanoparticles after conjugation, however (Table 4.1). This is a reasonable expectation, since a number of factors influence what the final

charge will be (*e.g.* percentage of amino groups that have undergone conjugation, percentage of amino groups that have been carboxylated, and the inherent charge of the targeting ligands). It is worth noting that the inherent charges of the targeting ligands does not, in itself, explain the small variation seen in surface charge, since at physiologic pH the charges on the HER2 affibody, RGD, and LDS are expected to be +3, 0, and 0, respectively. It is possible that these differences in nanoparticle surface charge may influence the formulations' blood circulation times, and consequently their tumor delivery. However, since this small variation in surface charge was introduced through the process of conjugation, it falls within the realm of what we desire to test: how does the presence of active targeting ligand effect each nanoparticle's pharmacokinetics and biodistribution.

The longitudinal and transverse relaxivities of each Ln-SPIO formulation was also determined (prior to ligand conjugation) and is reported in Table 4.1. There is significant variation in the magnetic properties for the four Ln-SPIO formulations, which is not unexpected since the batch-to-batch variation in magnetic properties is significant for traditional dextran SPIO without lanthanide dopant. While it is important to know the R2 value for each Ln-SPIO in order to normalize its MR signal during *in vitro* cell association assays (see below), agreement between R2 values is not necessary, since MR imaging is not a primary goal of this investigation. Nevertheless, it is noteworthy that, as seen in the SPIO synthesized in chapter 2, each Ln-SPIO formulation has significant magnetic activity. This is helpful since it means that once a set of nanoparticles is investigated using the ICP-MS multiplex approach, and a particular formulation that results in greatest tumor delivery has been identified, that specific formulation can then

be directly administered as a single injection and evaluated for its ability to generate MR contrast.

*In Vivo Equivalence of Nanoparticle Formulations Prior to Conjugation*

In order to conclude that differences in tumor accumulation are not due to any small differences in the physicochemical properties of the SPIO nanoparticles, it is important to demonstrate that the "base" nanoparticles, prior to ligand conjugation result in identical tumor delivery. Accordingly, each Ln-SPIO formulation was carboxylated to confer an equal negative charge to all formulations (see Table 4.1) and the set of nanoparticles was administered intravenously as a single multiplex injection to T6-17 tumor bearing mice (Figure 4.6).

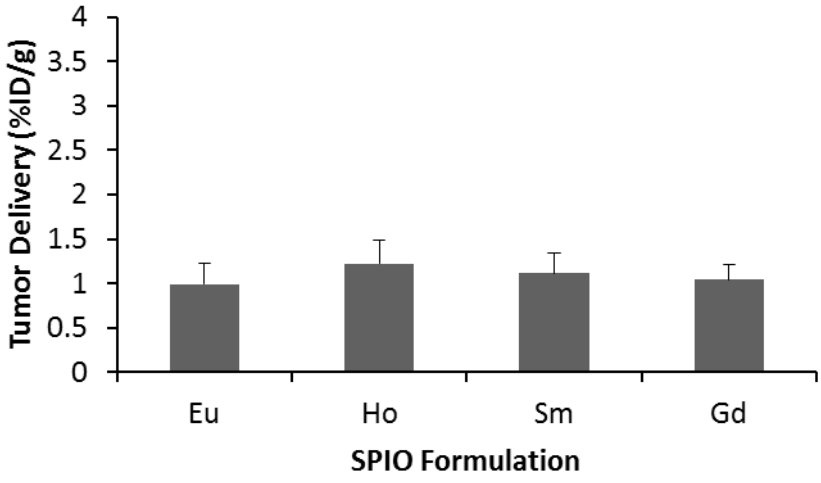


**Figure 4.6** In vivo multiplex ICP-MS analysis of nanoparticle accumulation in T6-17 tumors (expressed as percent injected dose / gram of tumor tissue) for carboxylated Ln-SPIO before conjugation to active targeting ligands. ANOVA analysis yielded an F ratio of 0.594, corresponding to a P value of 0.636

It was found that the tumor delivery for the four Ln-SPIO formulations ranged from 0.99 to 1.22 percent injected dose / gram of tumor tissue. One way analysis of variance (ANOVA) statistical testing demonstrated a P value of 0.594, indicating that there is no evidence of any meaningful difference in tumor delivery for any formulation within the set. Since ANOVA testing does not utilize the pairing information contained in multiplex data, a simple t-test (with pairing) was also conducted between the nanoparticle with lowest accumulation (Eu) and the one with highest accumulation (Ho). This yielded a P value of 0.16; again suggesting that even with the improved statistical power of paired analysis, there is no significant difference between the nanoparticle formulations at "baseline".

*Assessment of Biomarker Expression by Western Blot*

In order to assess the level of receptor expression for the three biomarkers investigated in this study, Western blots were conducted on T6-17 cells, HeLa cells, and excised T6-17 tumors. The blot images are provided in Figure 4.7.

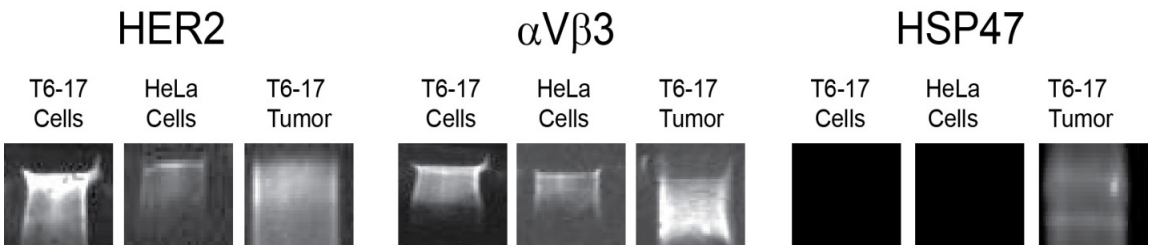


**Figure 4.7** Western Blots of T6-17 cells, HeLa cells, and excised T6-17 tumor tissue, probing for HER2, $\alpha_V\beta_3$ integrin, and Hsp47.

First, it was found that the level of HER2 (ErbB2) expression on T6-17 cells was very high and significantly greater than the level of expression on HeLa cells. Given that T6-17 cells are NIH-3T3 murine fibroblasts engineered to constitutively overexpress HER2, this result is expected. The relative abundance of HER2 protein in the excised T6-17 tumor appears lower than T6-17 cells *in vitro*. It is possible that this is due to an alteration of HER2 expression of the T6-17 cells once organized into a tumor, but it is more likely that the relative abundance of HER2 is lower as a result of the large amount of non-T6-17 cell derived protein in the tumor (*e.g.* stromal cells and extracellular matrix proteins). Nevertheless, HER2 expression was still clearly evident in the excised T6-17 tumor lysate.

Next, the level of $\alpha_V\beta_3$ integrin was examined. It was found that the level of expression of this biomarker was again higher in T6-17 cells compared to HeLa cells, although the degree of difference was much less than with the HER2 receptor. Studies have shown integrin $\alpha_V\beta_3$ expression in NIH/3T3 cells and this expression appears to be conserved in T6-17 cells.[38, 39] Interestingly, unlike the HER2 receptor relative abundance, which drops once the entire tumor is examined, the $\alpha_V\beta_3$ integrin levels are higher in the excised T6-17 tumor compared to the individual cells. This is likely because $\alpha_V\beta_3$ integrin is highly overexpressed on activated endothelial cells associated with the neovascularization of tumors.[40-42] In fact, previous reports have shown that in tumor xenograft models $\alpha_V\beta_3$ integrin can be overexpressed both on the malignant cells, themselves, and on host-derived proliferating endothelial cells.[43] This makes $\alpha_V\beta_3$ integrin a particularly interesting biomarker to compare with HER2. Specifically, even though HER2 is more abundant on tumor cells than $\alpha_V\beta_3$ integrin, targeting $\alpha_V\beta_3$ integrin

might result in increased tumor delivery, since it is expressed elsewhere in the tumor tissue. Importantly, this is a comparison that can only be adequately made *in vivo*, demonstrating the utility of being able to use ICP-MS for multiplex analysis *in vivo*.

Finally, levels of Hsp47 were examined. In this case, the expression of this biomarker was below the level of detection for both T6-17 and HeLa cells. Although there is little literature regarding the expression of Hsp47 on these two cells lines, it is not surprising to observe very low levels of expression since Hsp47 is most commonly associated with head and neck or gastrointestinal malignancies.[27, 29, 44, 45] Interestingly, however, Hsp47 expression was clearly detectable in the excised T6-17 tumor. There are two potential possibilities to account for this observation. First, it is known that Hsp47 expression is upregulated during a cellular stress response to noxious stimuli including high temperature, heavy metal exposure, and oxidative stress.[46] Since the establishment of a rapidly growing xenograft tumor is likely to be associated with a hostile local environment, it is possible that the T6-17 cells themselves are upregulating their expression of Hsp47. Alternatively, cell populations within the tumor other than the T6-17 cells themselves may be displaying the biomarker. In either case, this again illustrates the idea that evaluating active targeting of Hsp47 directed nanoparticles is best done fully at the *in vivo* stage, since expression profiles of the tumor are not the same as those *in vitro*.

*Flow Cytometric Analysis of Targeted Ln-SPIO*

The functionality of HER2-SPIO, LDS-SPIO and RGD-SPIO was subsequently assessed by conducting cell-binding assays with the broadly "receptor high" T6-17 cells and broadly "receptor low" HeLa cells. Flow cytometric analysis revealed that each targeted SPIO formulation successfully labeled T6-17 cells to varying extents, with the HER2-SPIO showing the highest degree of cell labeling and the LDS-SPIO showing the lowest (Figure 4.8 A). This is generally consistent with the results of the Western blots in that strong labeling was observed for the highly expressed HER2 receptor, and a lower level of labeling was observed for the less highly expressed $\alpha_V\beta_3$ integrin. Although Hsp47 expression was not detectable on Western blots of T6-17 cells, flow analysis is likely to be more sensitive given that each nanoparticle carries multiple fluorophores, thereby amplifying the signal. Eu-SPIO nanoparticles that have been reacted with ADIBO and carboxylated with succinic anhydride, but have no targeting ligand conjugated to them, showed no cell binding when incubated with T6-17 cells (Figure 4.8 B).

Based on the relative level of receptor expression between T6-17 and HeLa cells, a lower level of cell binding for each ligand is expected on HeLa cells, compared to T6-17 cells. The flow cytometric data bear this out in the most general sense, with undetectable cell binding of each targeted SPIO formulation to the broadly "receptor low" control HeLa cells (Figure 4.8 C). However, since flow cytometric measurements should have high sensitivity, we would expect that at least a low level of cell binding should be observed. Additionally, as expected, no cell binding was detected when unlabeled SPIO nanoparticles were incubated with HeLa cells (Figure 4.8 D).

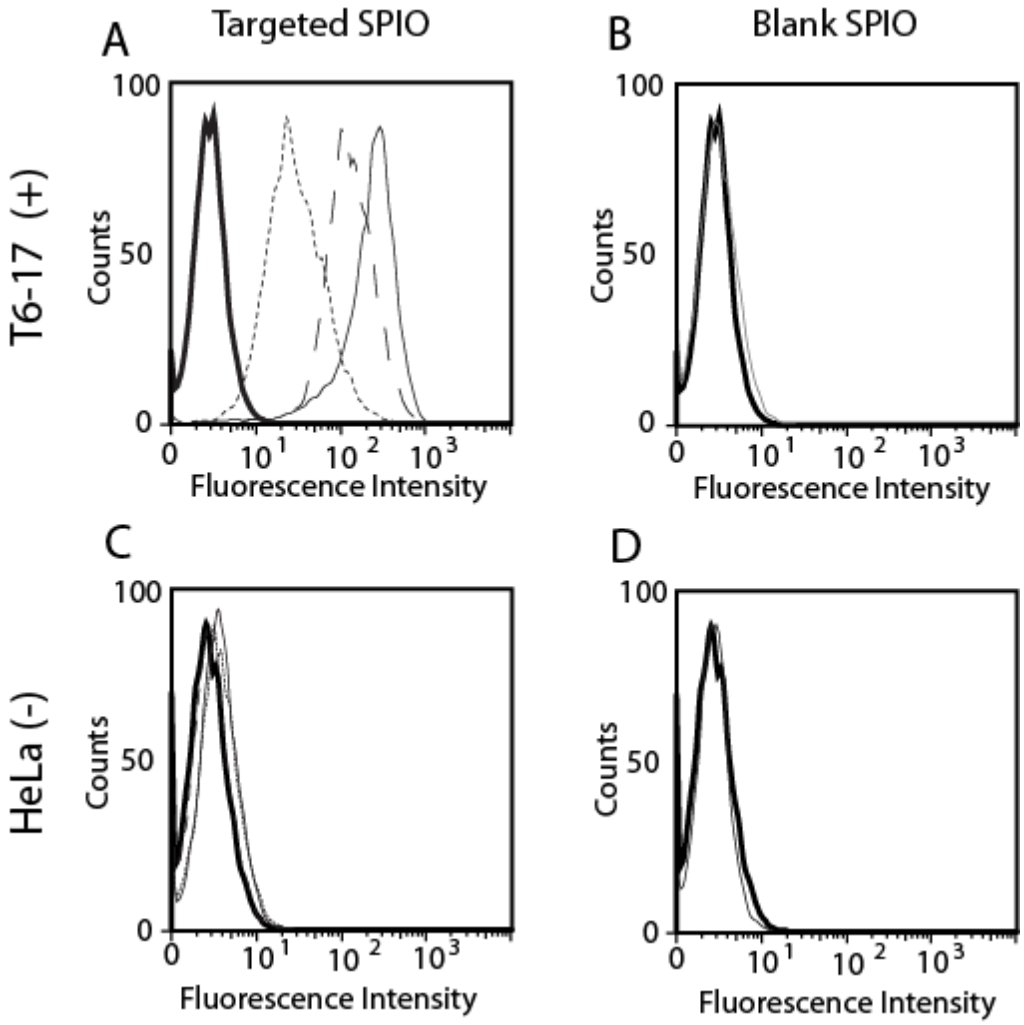


**Figure 4.8** Flow cytometric analysis of "receptor positive" (T6-17) and "receptor high" (HeLa) cells incubated with SPIO nanoparticles. T6-17 cells were incubated with HER2-SPIO (light solid line), RGD-SPIO (dashed line), and LDS-SPIO (dotted line), with varying degrees of cell labeling observed for each ligand (A). No cell labeling is evident for the "receptor low" HeLa cells for any of the ligands (C). Additionally, flow cytometric analysis was performed for both cell lines incubated with non-targeted SPIO and no cell labeling was detected (B and D).

*MR Comparison of Cell Binding*

*In vitro* cell binding assays were also carried out by incubating targeted SPIO conjugates with T6-17 or HeLa cells for 1 hour at a final concentration of 75 μg/mL Fe and examining the T2 relaxivity of cell pellets. This assay provided a more reliable measurement for the comparison of cell binding between ligands than flow cytometry does, since the fluorescence signal per nanoparticle is not expected to be the same for each formulation. For the MR assay, comparison of the level of cell labeling was made by using the reciprocal of the T2 relaxation time of the cell pellet as a measure of MR signal. The signal was adjusted by the R2 of the particular Ln-SPIO formulation used (*e.g.* Ho-SPIO for the affibody) to yield a normalized MR signal.

These data follow the same general trend as observed with the flow cytometric analysis. HER2 affibody conjugated SPIO exhibit an extremely high level of cell labeling on T6-17 cells and much lower labeling on HeLa cells (Figure 4.9). Again, it was not surprising that the HER2-SPIO displayed the highest degree of cell binding, since T6-17 cells have been transfected to overexpress the HER2/neu receptor.[47] RGD-SPIO exhibit approximately half the level of cell labeling (compared to HER2-SPIO) on T6-17 cells, but the level of labeling is clearly well above baseline nonspecific interactions observed with blank-SPIO. This level of labeling is also statistically greater than the very low level of labeling observed for RGD-SPIO of HeLa cells. Finally, while both cell lines exhibited a very low level labeling with LDS-SPIO, although even this low level of cell binding can be distinguished from the nonspecific binding of blank-SPIO.

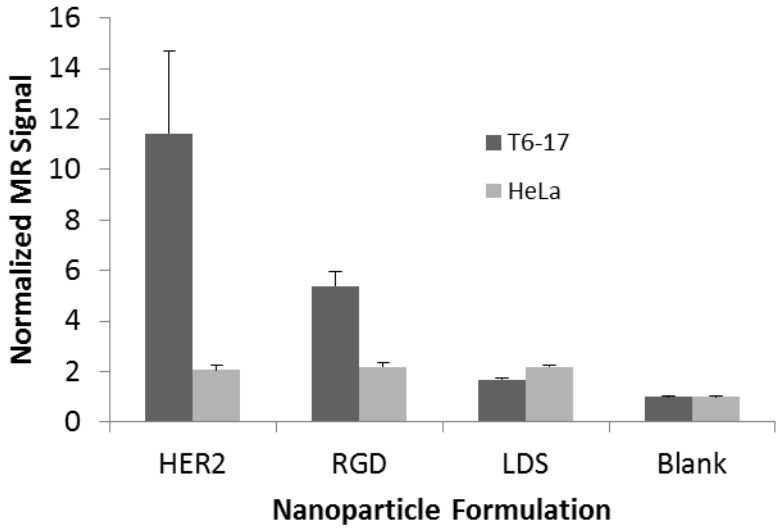


**Figure 4.9** Labeling of T6-17 and HeLa cells with Ho-HER2-SPIO, Sm-RGD-SPIO, Gd-LDS-SPIO and Eu-blank-SPIO, as assessed by MR relaxometry. Since each Ln-SPIO has different magnetic relaxivity, the T2 relaxation signal obtained for each cell pellet was normalized by the R2 value of the SPIO formulation and reported as a relative value to the signal of the blank formulation.

*ICP-MS Comparison of Cell Binding*

Finally, an ICP-MS *in vitro* cell binding assay was conducted by simultaneously incubating all targeted SPIO conjugates with T6-17 or HeLa cells for 1 hour at a final concentration of 75 µg/mL Fe and analyzing the lanthanide concentration of the washed cell pellets versus the lanthanide concentration in the incubating medium (Figure 4.10). This assay is expected to provide the most reliable data for making comparisons, both between ligands and between cell lines, for three reasons. First, each nanoparticle formulation's binding can be quantitatively normalized to the amount of material applied to the cells in the assay. Secondly, unlike the MR based assay, the "signal" detected by

ICP-MS is linear over a very large dynamic range of nanoparticle concentrations. This is especially important at low levels of nanoparticle binding, when ICP-MS can detect differences in binding that would not translate into a difference in MR signal. Thirdly, since this assay multiplexes the measurement of cell binding, many sample-to-sample variations (such as non-specific uptake by dead cells) are eliminated.

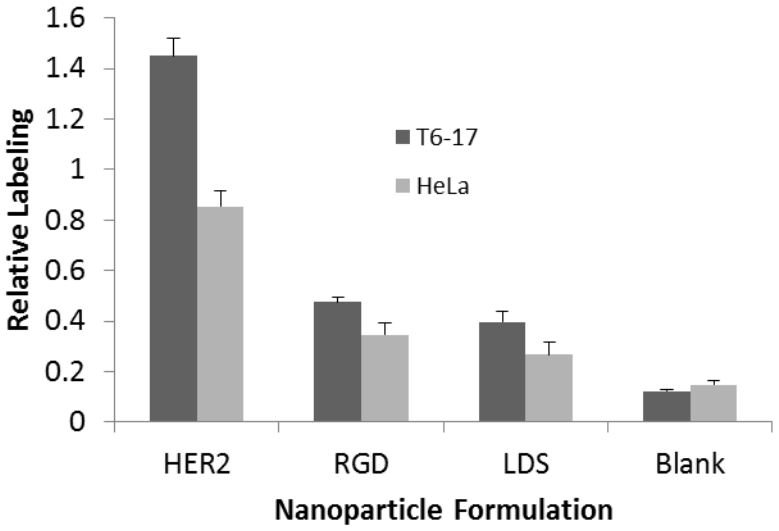


**Figure 4.10** Labeling of T6-17 and HeLa cells with Ho-HER2-SPIO, Sm-RGD-SPIO, Gd-LDS-SPIO and Eu-blank-SPIO, as assessed by ICP-MS multiplex analysis. All targeted nanoparticle formulations were pooled together and incubated with either T6-17 or HeLa cells in the presence of serum supplemented culture medium.

The ICP-MS multiplex data again bear out the same general conclusions as the flow cytometric and MR-based assays. First, for each ligand, the level of binding to the "receptor high" T6-17 cells is greater than the level of binding to the "receptor low" HeLa cells. Secondly, with respect to T6-17 cell binding, HER2-SPIO demonstrate the greatest level of cell labeling, followed by RGD-SPIO, and LDS-SPIO, all of which are

distinguishable from the non-specific of blank-SPIO. The major difference that the ICP-MS cell labeling data suggest is with regard to the absolute level of nanoparticle binding to HeLa cells. In the flow cytometric and MR analysis, there was very little cell binding observed for any of the ligands to HeLa cells. However, based on the Western blots, it can be concluded that while the HeLa cells are “receptor low” compared to T6-17 cells, they do not appear to be “receptor negative”. This discrepancy may be partly accounted for by the differences in sensitivity and signal linearity between the different modalities. Nevertheless, it appears that the flow cytometric results, which should provide a high level of sensitivity, will require further investigation in order to ensure the four sets of *in vitro* measurements are all properly reconciled.

## 4.5 Conclusion

It is possible to synthesize SPIO nanoparticles, doped with a variety of lanthanide tracer metals, each with an overlapping size distribution, so that they exhibit equal levels of passive tumor accumulation. These Ln-SPIO formulations can then be subsequently functionalized with active targeting ligands, such that each targeting ligand is associated with a specific lanthanide tracer. ICP-MS analysis can quantify the concentration of each lanthanide metal independently and with very high sensitivity, in a single fluid or tissue sample. Therefore, it becomes feasible to collect nanoparticle blood residence time, tumor delivery, and biodistribution for many actively targeted and negative control formulations in a single animal. This represents a powerful tool for nanotechnology investigators to more thoroughly evaluate a greater number of nanoparticle formulations *in vivo*, while reducing experiment time, cost, and number of animals.

## 4.6 References


1. Engels, F. K.; Mathot, R. A.; Verweij, J., Alternative drug formulations of docetaxel: a review. *Anticancer Drugs* 2007, 18, 95-103.

2. Power, S.; Slattery, M. M.; Lee, M. J., Nanotechnology and its relationship to interventional radiology. Part II: Drug Delivery, Thermotherapy, and Vascular Intervention. *Cardiovasc Intervent Radiol* 2011, 34, 676-90.

3. Vyas, S. P.; Gupta, S., Optimizing efficacy of amphotericin B through nanomodification. *Int J Nanomedicine* 2006, 1, 417-32.

4. Arias, J. L., Drug targeting strategies in cancer treatment: an overview. *Mini Rev Med Chem* 2011, 11, 1-17.

5. Choi, C. H.; Alabi, C. A.; Webster, P.; Davis, M. E., Mechanism of active targeting in solid tumors with transferrin-containing gold nanoparticles. *Proc Natl Acad Sci U S A* 2010, 107, 1235-40.

6. Davis, M. E., The first targeted delivery of siRNA in humans via a self-assembling, cyclodextrin polymer-based nanoparticle: from concept to clinic. *Mol Pharm* 2009, 6, 659-68.

7. Jiang, W.; Kim, B. Y.; Rutka, J. T.; Chan, W. C., Nanoparticle-mediated cellular response is size-dependent. *Nat Nanotechnol* 2008, 3, 145-50.

8. Chiu, G. N.; Edwards, L. A.; Kapanen, A. I.; Malinen, M. M.; Dragowska, W. H.; Warburton, C.; Chikh, G. G.; Fang, K. Y.; Tan, S.; Sy, J.; Tucker, C.; Waterhouse, D. N.; Klasa, R.; Bally, M. B., Modulation of cancer cell survival pathways using multivalent liposomal therapeutic antibody constructs. *Mol Cancer Ther* 2007, 6, 844-55.

9. Gindy, M. E.; Ji, S.; Hoye, T. R.; Panagiotopoulos, A. Z.; Prud'homme, R. K., Preparation of poly(ethylene glycol) protected nanoparticles with variable bioconjugate ligand density. *Biomacromolecules* 2008, 9, 2705-11.

10. Gu, F.; Zhang, L.; Teply, B. A.; Mann, N.; Wang, A.; Radovic-Moreno, A. F.; Langer, R.; Farokhzad, O. C., Precise engineering of targeted nanoparticles by using self-assembled biointegrated block copolymers. *Proc Natl Acad Sci U S A* 2008, 105, 2586-91.

11. Elias, D. R.; Cheng, Z.; Tsourkas, A., An intein-mediated site-specific click conjugation strategy for improved tumor targeting of nanoparticle systems. *Small* 6, 2460-8.

12. Fan, C.; Gao, W.; Chen, Z.; Fan, H.; Li, M.; Deng, F., Tumor selectivity of stealth multi-functionalized superparamagnetic iron oxide nanoparticles. *Int J Pharm* 404, 180-90.

13. Simberg, D.; Duza, T.; Park, J. H.; Essler, M.; Pilch, J.; Zhang, L.; Derfus, A. M.; Yang, M.; Hoffman, R. M.; Bhatia, S.; Sailor, M. J.; Ruoslahti, E., Biomimetic amplification of nanoparticle homing to tumors. *Proc Natl Acad Sci U S A* 2007, 104, 932-6.

14. Kiessling, F.; Huppert, J.; Zhang, C.; Jayapaul, J.; Zwick, S.; Woenne, E. C.; Mueller, M. M.; Zentgraf, H.; Eisenhut, M.; Addadi, Y.; Neeman, M.; Semmler, W., RGD-labeled USPIO inhibits adhesion and endocytotic activity of alpha v beta3-integrin-expressing glioma cells and only accumulates in the vascular tumor compartment. *Radiology* 2009, 253, 462-9.

15. Fang, C.; Veiseh, O.; Kievit, F.; Bhattarai, N.; Wang, F.; Stephen, Z.; Li, C.; Lee, D.; Ellenbogen, R. G.; Zhang, M., Functionalization of iron oxide magnetic nanoparticles with targeting ligands: their physicochemical properties and in vivo behavior. *Nanomedicine (Lond)* 5, 1357-69.

16. Morishige, K.; Kacher, D. F.; Libby, P.; Josephson, L.; Ganz, P.; Weissleder, R.; Aikawa, M., High-resolution magnetic resonance imaging enhanced with superparamagnetic nanoparticles measures macrophage burden in atherosclerosis. *Circulation* 122, 1707-15.

17. Tsourkas, A.; Shinde-Patil, V. R.; Kelly, K. A.; Patel, P.; Wolley, A.; Allport, J. R.; Weissleder, R., In vivo imaging of activated endothelium using an anti-VCAM-1 magnetooptical probe. *Bioconjug Chem* 2005, 16, 576-81.

18. Kelly, K. A.; Allport, J. R.; Tsourkas, A.; Shinde-Patil, V. R.; Josephson, L.; Weissleder, R., Detection of vascular adhesion molecule-1 expression using a novel multimodal nanoparticle. *Circ Res* 2005, 96, 327-36.

19. Thorek, D. L.; Tsao, P. Y.; Arora, V.; Zhou, L.; Eisenberg, R. A.; Tsourkas, A., In vivo, multimodal imaging of B cell distribution and response to antibody immunotherapy in mice. *PLoS One* 5, e10655.

20. Lewin, M.; Carlesso, N.; Tung, C. H.; Tang, X. W.; Cory, D.; Scadden, D. T.; Weissleder, R., Tat peptide-derivatized magnetic nanoparticles allow in vivo tracking and recovery of progenitor cells. *Nat Biotechnol* 2000, 18, 410-4.

21. Zhao, M.; Beauregard, D. A.; Loizou, L.; Davletov, B.; Brindle, K. M., Non-invasive detection of apoptosis using magnetic resonance imaging and a targeted contrast agent. *Nat Med* 2001, 7, 1241-4.

22. Mouli, S. K.; Zhao, L. C.; Omary, R. A.; Thaxton, C. S., Lymphotropic nanoparticle enhanced MRI for the staging of genitourinary tumors. *Nat Rev Urol* 7, 84-93.

23. Branca, R. T.; Cleveland, Z. I.; Fubara, B.; Kumar, C. S.; Maronpot, R. R.; Leuschner, C.; Warren, W. S.; Driehuys, B., Molecular MRI for sensitive and specific detection of lung metastases. *Proc Natl Acad Sci U S A* 107, 3693-7.

24. Guzman, R.; Uchida, N.; Bliss, T. M.; He, D.; Christopherson, K. K.; Stellwagen, D.; Capela, A.; Greve, J.; Malenka, R. C.; Moseley, M. E.; Palmer, T. D.; Steinberg, G. K., Long-term monitoring of transplanted human neural stem cells in developmental and pathological contexts with MRI. *Proc Natl Acad Sci U S A* 2007, 104, 10211-6.

25. Irshad, S.; Ellis, P.; Tutt, A., Molecular heterogeneity of triple-negative breast cancer and its clinical implications. *Curr Opin Oncol* 2011, 23, 566-77.

26. Rudnick, S. I.; Lou, J.; Shaller, C. C.; Tang, Y.; Klein-Szanto, A. J.; Weiner, L. M.; Marks, J. D.; Adams, G. P., Influence of affinity and antigen internalization on the uptake and penetration of Anti-HER2 antibodies in solid tumors. *Cancer Res* 2011, 71, 2250-9.

27. Araki, K.; Mikami, T.; Yoshida, T.; Kikuchi, M.; Sato, Y.; Oh-ishi, M.; Kodera, Y.; Maeda, T.; Okayasu, I., High expression of HSP47 in ulcerative colitis-associated carcinomas: proteomic approach. *Br J Cancer* 2009, 101, 492-7.

28. Gaertner, F. C.; Schwaiger, M.; Beer, A. J., Molecular imaging of alphavss3 expression in cancer patients. *Q J Nucl Med Mol Imaging* 2010, 54, 309-26.

29. Hirai, K.; Kikuchi, S.; Kurita, A.; Ohashi, S.; Adachi, E.; Matsuoka, Y.; Nagata, K.; Watanabe, M., Immunohistochemical distribution of heat shock protein 47 (HSP47) in scirrhous carcinoma of the stomach. *Anticancer Res* 2006, 26, 71-8.

30. Lee, S. S.; Tseng, L. H.; Li, Y. C.; Tsai, C. H.; Chang, Y. C., Heat shock protein 47 expression in oral squamous cell carcinomas and upregulated by arecoline in human oral epithelial cells. *J Oral Pathol Med* 2011, 40, 390-6.

31. Beer, A. J.; Schwaiger, M., Imaging of integrin alphavbeta3 expression. *Cancer Metastasis Rev* 2008, 27, 631-44.

32. Dijkgraaf, I.; Beer, A. J.; Wester, H. J., Application of RGD-containing peptides as imaging probes for alphavbeta3 expression. *Front Biosci* 2009, 14, 887-99.

33. Lee, S. B.; Hassan, M.; Fisher, R.; Chertov, O.; Chernomordik, V.; Kramer-Marek, G.; Gandjbakhche, A.; Capala, J., Affibody molecules for in vivo characterization of HER2-positive tumors by near-infrared imaging. *Clin Cancer Res* 2008, 14, 3840-9.

34. Li, D.; Guang, W.; Abuzeid, W. M.; Roy, S.; Gao, G. P.; Sauk, J. J.; O'Malley, B. W., Jr., Novel adenoviral gene delivery system targeted against head and neck cancer. *Laryngoscope* 2008, 118, 650-8.

35. Orlova, A.; Tolmachev, V.; Pehrson, R.; Lindborg, M.; Tran, T.; Sandstrom, M.; Nilsson, F. Y.; Wennborg, A.; Abrahmsen, L.; Feldwisch, J., Synthetic affibody molecules: a novel class of affinity ligands for molecular imaging of HER2-expressing malignant tumors. *Cancer Res* 2007, 67, 2178-86.

36. Sauk, J. J.; Coletta, R. D.; Norris, K.; Hebert, C., Binding motifs of CBP2 a potential cell surface target for carcinoma cells. *J Cell Biochem* 2000, 78, 251-63.

37. Thorek, D. L.; Tsourkas, A., Size, charge and concentration dependent uptake of iron oxide particles by non-phagocytic cells. *Biomaterials* 2008, 29, 3583-90.

38. Sakamoto, Y.; Ogita, H.; Hirota, T.; Kawakatsu, T.; Fukuyama, T.; Yasumi, M.; Kanzaki, N.; Ozaki, M.; Takai, Y., Interaction of integrin alpha(v)beta3 with nectin. Implication in cross-talk between cell-matrix and cell-cell junctions. *J Biol Chem* 2006, 281, 19631-44.

39. White, D. P.; Caswell, P. T.; Norman, J. C., alpha v beta3 and alpha5beta1 integrin recycling pathways dictate downstream Rho kinase signaling to regulate persistent cell migration. *J Cell Biol* 2007, 177, 515-25.

40. Albelda, S. M.; Mette, S. A.; Elder, D. E.; Stewart, R.; Damjanovich, L.; Herlyn, M.; Buck, C. A., Integrin distribution in malignant melanoma: association of the beta 3 subunit with tumor progression. *Cancer Res* 1990, 50, 6757-64.

41. Bello, L.; Francolini, M.; Marthyn, P.; Zhang, J.; Carroll, R. S.; Nikas, D. C.; Strasser, J. F.; Villani, R.; Cheresh, D. A.; Black, P. M., Alpha(v)beta3 and alpha(v)beta5 integrin expression in glioma periphery. *Neurosurgery* 2001, 49, 380-9; discussion 390.

42. Felding-Habermann, B.; Mueller, B. M.; Romerdahl, C. A.; Cheresh, D. A., Involvement of integrin alpha V gene expression in human melanoma tumorigenicity. *J Clin Invest* 1992, 89, 2018-22.

43. Zitzmann, S.; Ehemann, V.; Schwab, M., Arginine-glycine-aspartic acid (RGD)-peptide binds to both tumor and tumor-endothelial cells in vivo. *Cancer Res* 2002, 62, 5139-43.

44. Nikitakis, N. G.; Rivera, H.; Lopes, M. A.; Siavash, H.; Reynolds, M. A.; Ord, R. A.; Sauk, J. J., Immunohistochemical expression of angiogenesis-related markers in oral

squamous cell carcinomas with multiple metastatic lymph nodes. *Am J Clin Pathol* 2003, 119, 574-86.

45. Maitra, A.; Iacobuzio-Donahue, C.; Rahman, A.; Sohn, T. A.; Argani, P.; Meyer, R.; Yeo, C. J.; Cameron, J. L.; Goggins, M.; Kern, S. E.; Ashfaq, R.; Hruban, R. H.; Wilentz, R. E., Immunohistochemical validation of a novel epithelial and a novel stromal marker of pancreatic ductal adenocarcinoma identified by global expression microarrays: sea urchin fascin homolog and heat shock protein 47. *Am J Clin Pathol* 2002, 118, 52-9.

46. Morimoto, R. I.; Kline, M. P.; Bimston, D. N.; Cotto, J. J., The heat-shock response: regulation and function of heat-shock proteins and molecular chaperones. *Essays Biochem* 1997, 32, 17-29.

47. Cheng, L. S.; Liu, A. P.; Yang, J. H.; Dong, Y. Q.; Li, L. W.; Wang, J.; Wang, C. C.; Liu, J., Construction, expression and characterization of the engineered antibody against tumor surface antigen, p185(c-erbB-2). *Cell Res* 2003, 13, 35-48.

# Chapter 5: pH Titratable Superparamagnetic Iron Oxide for Improved Nanoparticle Accumulation in Acidic Tumor Microenvironments

## 5.1 Abstract

A wide variety of nanoparticle platforms are being developed for both the diagnosis and treatment of malignancy. While many of these are either passively targeted or rely on specific receptor-ligand interactions, metabolically directed nanoparticles can provide a complementary approach. It is known that both primary and secondary events in tumorigensis alter the metabolic profile of developing and metastatic cancers. One highly conserved metabolic phenotype is a state of up-regulated glycolysis and reduced use of oxidative phosphorylation, even when oxygen tension is not limiting. This metabolic shift, termed the Warburg effect, creates a "hostile" tumor microenvironment with increased levels of lactic acid and low extracellular pH. In order to exploit this phenomenon to improve the delivery of nanoparticle platforms to a wide variety of tumors, a pH-responsive iron oxide nanoparticle was designed. Specifically, glycol chitosan (GC), a water-soluble polymer with pH titratable charge, was conjugated to the surface of superparamagnetic iron oxide nanoparticles (SPIO) to generate a $T_2$* weighted MR contrast agent that responds to alterations in its surrounding pH. When compared to control nanoparticles that lack sensitivity to pH, these GC-SPIO nanoparticles demonstrated potent pH-dependent cellular association and MR contrast *in vitro*. In murine tumor models GC-SPIO also generated robust $T_2$* weighted tumor contrast, which correlated with increased delivery of the agent to the tumor site, as measured

quantitatively by inductively coupled plasma mass spectrometry. Importantly, the increased delivery of GC-SPIO nanoparticles cannot be attributed to the commonly observed enhanced permeability and retention effect alone, since these nanoparticles have similar physical properties and blood circulation times as control agents.

## 5.2 Introduction

Tumor targeting mechanisms that exploit the altered metabolic profile of malignancy have been the subject of intense investigation[1] since the development of the metabolite analogue 2-fluorodeoxy-D-glucose (2FDG) and its use in positron emission tomography (PET) imaging over three decades ago.[2] One of the attractions of metabolic imaging is the ability to detect and target a wide variety of cancers, since many human solid tumors, and especially rapidly growing aggressive malignancies, have a unique metabolic profile that distinguishes them from normal tissue.[3] This altered metabolic state, consistent with the Warburg effect, is characterized by increased glucose uptake, up-regulated glycolytic metabolism, increased production of lactic acid, and subsequent derangements in cellular pH.[4, 5] More specifically, the extracellular pH of normal tissue is approximately 7.4, but human and animal tumors can often exhibit an extracellular pH lower than 7.0, even reaching as low as 6.3.[6, 7]

In recent years, numerous methods have been developed that allow for the non-invasive assessment of tissue pH, most of which are based on magnetic resonance.[6] For example, magnetic resonance spectroscopy (MRS) using endogenous inorganic phosphate ($P_i$) and exogenously administered 3-aminopropylphosphate (3-APP) can be used to simultaneously measure intra- and extracellular pH, respectively.[8, 9] Major drawbacks of this method are the reliance on the relatively less abundant $^{31}P$ nucleus and the inability to simultaneously acquire the high resolution anatomical information that is the hallmark of magnetic resonance (MR) imaging. More recently, exogenous agents with pH-dependent proton resonances have been developed.[10] While this eliminates the need for specialized $^{31}P$ hardware, the pH sensitive resonance can be difficult to fully distinguish from other endogenous signals. Even more recently, pH-sensitive lanthanide

chelates have allowed for measurement of pH with a proton resonance completely distinct from endogenous signals.[11, 12] Even these agents, however, have limited sensitivity since the exogenous agent contains the resonance being detected. Greater sensitivity could be obtained using a contrast agent that generates signal by interacting with many bulk water molecules. Superparamagnetic iron oxide (SPIO) nanoparticles have emerged as an attractive class of MR contrast agent that provides $T_2$*-weighted contrast enhancement in both active and passive MR imaging applications by accelerating the de-phasing of nearby bulk water.[13] SPIO nanoparticles could, therefore, serve as a strong signal-generating foundation to which pH sensitivity could be imparted. Such pH-responsive SPIO nanoparticles would constitute an $^1$H MR contrast agent that exhibits differential localization based on local pH and could facilitate the detection of acidic pathologies, including but not limited to malignancy, on conventional high resolution anatomic MR images, without the need for specialized hardware. Such regions of suspected acidity, detected with pH-responsive SPIO on large field-of-view anatomic images, could then be probed by MRS or chemical exchange saturation transfer (CEST) methods to generate an absolute pH map.

pH-responsive polymers, including chitosan,[14] poly-amino ester,[15] poly-caprolactone,[16] and poly-histidine,[17] have been successfully used to generate pH-mediated drug release in a variety of nanoparticle carriers. Furthermore, SPIO nanoclusters coated with a pH-responsive hydrogel have recently yielded nanoparticles with pH-dependent relaxivity.[18] Therefore, pH-titratable polymers are attractive candidates for imparting such functionality to nanoparticles. Accordingly, in this investigation, the pH-responsive polymer glycol chitosan (GC, Figure 5.1 A), a polymer

of glucosamine with increased water solubility and amino groups with a $pK_a \approx 6.5$,[19] was covalently grafted to the surface of dextran stabilized SPIO nanoparticles, to generate native GC-SPIO. Sized matched pH-unresponsive SPIO nanoparticles were prepared as control agents to distinguish pH-mediated nanoparticle delivery from the enhanced permeability and retention (EPR) effect that is commonly observed for nanoparticle agents.[20-23] Specifically, GC-coated SPIO nanoparticles were chemically modified with glycidol (Figure 5.1 B) to block the pH-responsive amino groups, and inherently pH-unresponsive dextran SPIO nanoparticles (Figure 5.1 C) were also used.

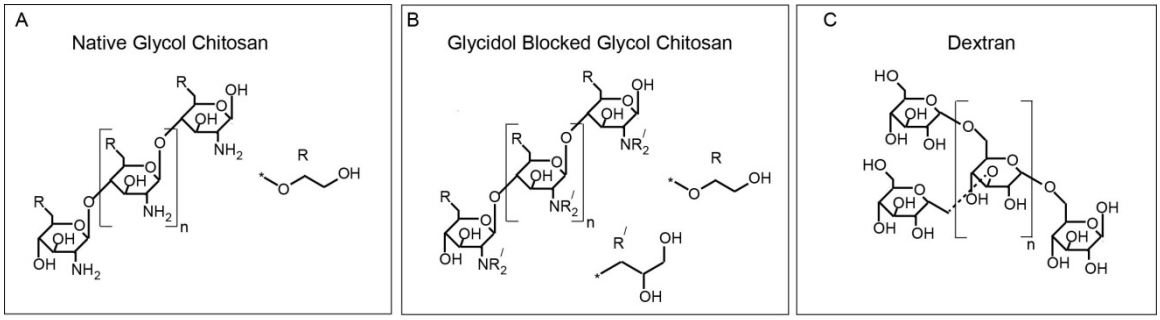


**Figure 5.1** Molecular structures of nanoparticle polymeric surface coatings. (A) Native GC is a linear polymer of D-glucosamine with β-1-4 linkages. The repeated amino groups have aggregate pKa ≈ 6.5. (B) Glycidol blocked GC is formed by reaction of native GC with glycidol. Alkylation of the amino groups renders them no longer titratable near physiologic pH. (C) Dextran is a branched polymer of glucose with both α-1-3 and α-1-3 linkages. It does not possess any functional groups that are titratable near physiologic pH.

All nanoparticle formulations included a lanthanide metal tracer that allowed the distribution of the nanoparticles to be tracked quantitatively *in vivo*. Specifically, during the synthesis of the SPIO nanoparticles, a trace amount of lanthanide was doped into the iron oxide cores (Gd for the two GC-containing SPIO formulations and Sm for the dextran-only SPIO). Energy-dispersive X-ray spectroscopy (EDS) has previously been used to confirm the presence and stability of the lanthanide dopant within the iron oxide cores of SPIO synthesized in this manner.[24] Here, inductively coupled plasma mass spectrometry (ICP-MS) was used to assess the biodistribution of the lanthanide tracer (and the corresponding SPIO nanoparticle) in a mouse tumor model.

Numerous studies have shown that nanoparticles (including SPIO) complexed with cationic agents such as polylysine, protamine, or cell penetrating peptides (CPPs) are rapidly and efficiently internalized by a wide range of cell types.[25-28] However, positively charged nanoparticles are rapidly cleared from circulation,[29] resulting in poor tumor delivery. Therefore, positive charge could be used to improve retention in a desired microenvironment, provided that the positive charge is not displayed until that microenvironment is reached. Accordingly, both the native GC-SPIO and control agents exhibit a neutral or negative surface charge at physiologic pH, affording them a lower level of cellular interaction and improving blood residence time.[30, 31] (Figure 5.2 A). Upon exposure to an acidic mircroenvironment, the pH-responsive polymer surface of the native GC-SPIO becomes protonated and the surface charge becomes increasingly positive. Therefore, it was hypothesized that native GC-SPIO nanoparticles would be preferentially retained in acidic microenvrionments compared with analogous pH-

unresponsive agents, as a result of electrostatic interactions with surrounding tissue (Figure 5.2 B).

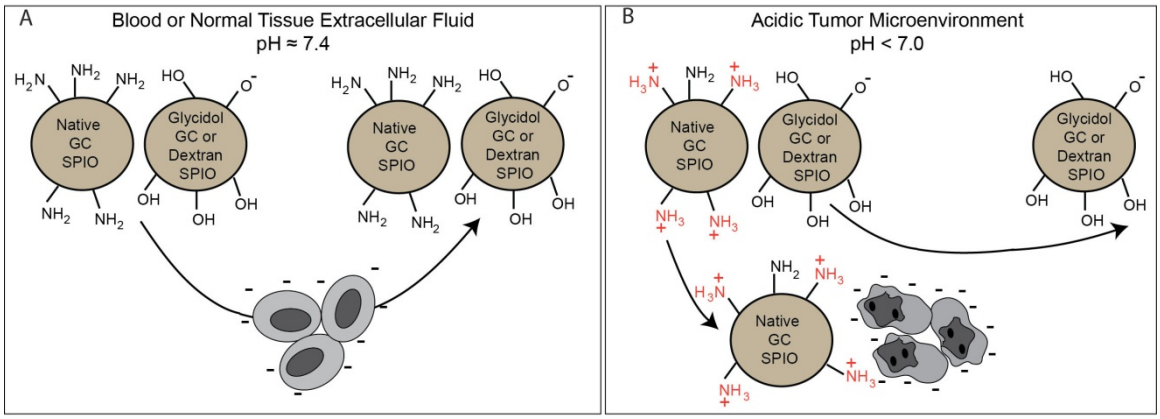


**Figure 5.2** Mechanism of enhanced nanoparticle retention in acidic microenvironments. (A) Both native GC-SPIO and control nanoparticles exhibit neutral to negative surface charge at physiologic pH due to abundant surface hydroxyl groups. For clarity, the hydroxyl groups are not depicted on the native GC-SPIO particle. Presence of neutral or negative surface charge diminishes nanoparticle association with blood components and normal tissue. (B) Upon exposure to acidic microenvironments, the amino groups of native GC-SPIO titrate to yield a positive charge. The newly cationic nanoparticles exhibit electrostatic interactions with negatively charged cell membranes and extracellular matrix components in the acidic microenvironment, leading to enhanced retention in these areas.

## 5.3 Materials and Methods

*Materials*

The two SPIO coating polymers dextran T10 and glycol chitosan were purchased from Pharmacosmos A/S (Holbaek, Denmark) and Wako Chemicals (Richmond, VA, USA), respectively. T6-17 murine fibroblasts (a derivative of the NIH/3T3 line) were kindly provided by Mark Greene, PhD, FRCP, at the University of Pennsylvania. The 35

mm volume coil used for radiofrequency transmission and reception was purchased from Insight Neuroimaging Systems, LLC (Worcester, MA). All other reagents were purchased from Sigma Aldrich USA unless otherwise noted.

*Synthesis of Dextran Stabilized Lanthanide Doped SPIO*

Dextran coated, lanthanide doped, SPIO nanoparticles were prepared though the coprecipitation of ferrous, ferric, and lanthanide ions in the presence of dextran.[24, 28] Briefly, 50 g of dextran T-10, was dissolved in 100 mL $dH_2O$ and heated to 80°C for 1 hour. The solution was then allowed to cool to room temperature and continued to mix overnight. Subsequently, a solution of 3.70 g $FeCl_3$, 1.46 g $FeCl_2$, and 0.25 g $GdCl_3 \cdot 6H_2O$ or $SmCl_3 \cdot 6H_2O$ in 50 mL $dH_2O$ was prepared and decanted into the dextran solution. The combined solution was cooled on ice and degassed with $N_2$ for 90 min. While keeping the solution stirring on ice and under $N_2$, an automated syringe pump was then used to introduce 15 mL of concentrated $NH_4OH$ to the solution over 5 hours. The resulting black viscous solution was removed from the $N_2$ atmosphere, heated to 90°C for 1 hour, cooled overnight, and centrifuged at 20,000 RCF for 30 minutes to remove large aggregates. Free iron, lanthanide, and dextran were removed by diafilitration across a 100 kDa membrane and the dextran SPIO were brought to a final volume of 40 mL.

*Surface Conjugation of Glycol Chitosan*

High molecular weight glycol chitosan was degraded and prepared for grafting to dextran SPIO as follows: 10 g of ≈600 kDa GC was dissolved in 200 mL 6M HCl and heated to 80°C for 20 minutes. Following incubation, the material was cooled on ice and immediately neutralized with the addition of solid sodium carbonate to terminate

degradation. Excess solid sodium carbonate was removed by centrifugation and diafiltration membranes were used to de-salt the material and discard any GC polymer greater than 100 kDa or less than 3 kDa.

Native glycol chitosan (GC)-SPIO was then prepared as follows: 40 mL of dextran SPIO at an iron concentration of 10 mg/mL was combined with an equal volume of 10 M NaOH and mixed for 10 minutes. 80 mL of epichlorohydrin was then added and the solution was vigorously stirred at room temperature overnight. Epichlorohydrin crosslinks dextran chains within a SPIO particle and chemically activates the dextran surface for grafting of glycol chitosan. The solution was then briefly centrifuged to allow phase-separation into an aqueous black SPIO layer and a clear layer of unreacted epichlorohydrin, which was removed. The SPIO layer was quickly purified via extraction in isopropanol. Specifically, the SPIO material was combined with 5 volumes of isopropanol and the mixture was vigorously shaken. Brief centrifugation of the mixture resulted in a layer of precipitated salt, a SPIO layer, and an isopropanol layer (containing any remaining epichlorohydrin). The SPIO layer was then isolated and combined with an equal volume of 150 mg/mL GC (3 – 100 kDa) in PBS, and gently stirred for 72 hours at room temperature. After the reaction, free GC was removed by diafiltration across a 100 kDa membrane and the final native GC-SPIO was 0.2 μm filtered to remove any oversized material. Finally, to ensure complete purification of the GC-SPIO from excess GC and to enhance the material's magnetic properties, the nanoparticles were magnetically purified on MACS LS columns using the MidiMACS magnet (Miltenyi Biotec, Auburn, CA, USA).

*Generation of Control SPIO Nanoparticles*

Glycidol GC-SPIO control nanoparticles were produced by direct chemical modification of the native GC-SPIO nanoparticle surface. Briefly, native GC-SPIO at 5 mg Fe/mL in 10 mM pH 5.0 HEPES buffer was combined with an equal volume of glycidol and stirred at room temperature overnight. GC-SPIO was then precipitated from the solution by the addition of 4 volumes of isopropanol. Since the blocking was incomplete after only one round of reaction with glycidol, the addition at 0.2 volumes of 7.5% sodium bicarbonate was sometimes required to neutralize remaining positive charge on the nanoparticle surface and induce precipitation. The solution was centrifuged, the supernatant discarded, and the GC-SPIO pellet was resuspended with sonication in the original volume of HEPES buffer. Reaction with glycidol was repeated as above 2 more times to exhaustively block pH responsive amino groups (subsequent reactions do not require bicarbonate to induce precipitation in isopropanol). Finally, sized matched dextran SPIO were used as a second pH-unresponsive control nanoparticle formulation. In order to best match the size of the dextran SPIO control nanoparticles to the GC grafted nanoparticles, the dextran SPIO nanoparticles used as a control were not from the same synthesis as the dextran SPIO upon which the GC grafted nanoparticles were constructed. Specifically, the rate of $NH_4OH$ addition was increased in order to produce somewhat larger size dextran SPIO.

*Native GC-SPIO and Control Nanoparticle Physicochemical Characterization*

Each nanoparticle formulation was diluted to a final concentration of 100 μg Fe/mL in pH 7.4 phosphate buffered saline for determination of the hydrodynamic diameter by dynamic light scattering (DLS). Measurements were acquired with a

Zetasizer Nano-ZS (Malvern Instruments, Worcestershire, UK) using the non-invasive back-scatter (NIBS) mode. Samples were further diluted in water and deposited on 200-mesh carbon coated copper grids (Polysciences, Warrington, PA, USA) for TEM imaging with a JEOL 1010 transmission electron microscope operating at 80 kV. Mean iron core size was determined by measuring 100 individual nanoparticles. The transverse ($R_2$) and longitudinal ($R_1$) relaxivities of the nanoparticle formulations were calculated by plotting the reciprocal of the relaxation time (measured using a Bruker mq60 tabletop MR relaxometer operating at 1.41 T) versus the iron concentration. For elemental analysis, nanoparticles were precipitated with isopropanol, dried under vacuum, and submitted to Intertek Analytical Laboratories (Whitehouse, NJ, USA). Since glycol chitosan is the only nitrogen containing component of the nanoparticles, the %N of the sample can be scaled to %GC, using the empirical formula of glycol chitosan, $C_8H_{15}O_5N$. Similarly, since dextran is the only carbon containing component (after the carbon content of GC is accounted for), the %dextran can be calculated using its empirical formula, $C_6H_{10}O_5$. For zeta potential pH titrations, 10 mM HEPES buffered water was prepared with pH values ranging from 5.90 to 7.65 in 0.25 unit increments. Each nanoparticle formulation was diluted to a final concentration of 100 μg Fe/mL in the buffer at each pH and mean nanoparticle zeta potential was measured using a Zetasizer Nano-ZS. Stocks of native GC-SPIO, glycidol GC-SPIO, and dextran SPIO were synthesized several times throughout the course of the study, each time yielding similar physicochemical properties.

*Cell Culture*

T6-17 murine fibroblasts were cultured and maintained in Dulbecco's modified Eagle's medium (DMEM), supplemented with 10% fetal bovine serum (FBS), 1% penicillin/streptomycin at 37°C and 5% $CO_2$.

*In Vitro Cellular Association Studies*

For *in vitro* pH studies, cell culture medium was supplemented with 25 mM HEPES buffer and prepared with pH values ranging from 5.90 to 7.65 in 0.25 unit increments. Each nanoparticle formulation was incubated in suspension at a concentration of 25 μg Fe/mL with 4 x $10^6$ of freshly trypsinized T6-17 cells for 1 hour at 37°C in a total volume of 0.5 mL buffered medium. Following incubation, unassociated nanoparticles were removed by triplicate low-speed centrifugal washes with nanoparticle free medium of matching pH. The cell samples were then resuspended in 0.3 mL of PBS at pH 7.4 and the $T_2$ relaxation time of the suspensions were measured on the tabletop relaxometer.

*Cell Pellet MR Imaging*

Following relaxation measurements, the triplicate samples at each pH were combined to form a single cell pellet for each pH and nanoparticle formulation. The samples were transferred to a 384-well plate and the cells were pelleted to the bottom of each well with brief, low-speed centrifugation. The plate was then imaged on a 9.4-T magnet interfaced to a Varian INOVA console using a 70 mm inner diameter volume coil for radiofrequency transmission and reception. T2*-weighted gradient echo (GEMS) MR

images were collected using parameters as follows: repetition time (TR) = 200 ms, echo time (TE) = 5 ms, flip angle = 20°, slice thickness = 0.5 mm, field of view (FOV) = 4 cm x 4 cm, number of acquisitions = 8, resolution = 256 x 256.

*Contrast Enhanced In Vivo MR Imaging*

Approximately 6-week old female nu/nu nude mice (Charles River Laboratory, Charles River, MS, USA) were maintained in accordance with the Institutional Animal Care and Use Committee of the University of Pennsylvania. Mice were anesthetized via isoflurane and T6-17 cells were injected subcutaneously into the back right flank ($2 \times 10^6$ cells in 0.2 mL PBS). Tumors were grown until the diameter was approximately 8 mm and pre-contrast tumor images were acquired using a 9.4-T magnet interfaced to a Varian INOVA console. $T_2$*-weighted GEMS images were collected using the same parameters as for plate images, except slice thickness = 1 mm. Immediately following the pre-contrast image acquisition, native GC-SPIO or control nanoparticles were administered by retro-orbital injection (10 mg/kg Fe in 0.2 mL; Native GC-SPIO n=4, glycidol GC-SPIO n=4, dextran SPIO n=3). Post-contrast images were collected 24 hours post-injection under the same imaging parameters used for pre-contrast images.

*MR Image Analysis*

For each animal's pre- and post-contrast image, three corresponding axial slices were selected for analysis. To account for signal variations between images due to mouse or RF coil positioning, the relative signal intensity (RSI) of the tumor in each slice was calculated by dividing the MR signal of the operator defined tumor region of interest (ROI) by that of the adjacent paraspinal muscle. Nanoparticle induced tumor contrast was then determined as the RSI ratio for each animal, calculated as the quotient of the post-

contrast tumor RSI to the pre-contrast tumor RSI. Following statistically significant ANOVA analysis for the three nanoparticles' contrast, individual t-tests were performed.

*Quantitation of Tumor Delivery and Blood Concentration by ICP-MS*

Prior to nanoparticle injection, an aliquot of nanoparticles from each group of mice was saved for inductively coupled plasma mass spectrometry (ICP-MS) determination of lanthanide concentration (Gd for native and glycidol GC-SPIO and Sm for dextran SPIO). Following nanoparticle injection, 10 μL blood samples were collected from each animal, using the tail-nick method, at times of 1, 2, 4, 7, and 24 hours post-injection. Following post-contrast MR imaging, the animals were sacrificed and the tumors, livers, and kidneys excised.

For ICP-MS analysis, analytical standards were purchased from SCP (Champlain, NY, USA) and trace metal grade nitric acid was purchased from Fisher Scientific (Pittsburg, PA, USA). All dilutions were done using in-house deionized water (≥18 MΩ-cm) obtained from a Millipore water purification system.

The pre-injection solutions, blood, and tumor samples were analyzed for $^{158}$Gd (gadolinium), or $^{147}$Sm (samarium) using an Elan 6100 ICP-MS (Perkin Elmer, Shelton, CT, USA) at the New Bolton Center Toxicology Laboratory, University of Pennsylvania, School of Veterinary Medicine, Kennett Square, PA, USA. The samples were weighed into Teflon PFA vials (Savillex, Minnetonka, MN, USA) and digested overnight with 70% nitric acid at $70^0$ C. 0.1 mL of 2 ppm $^{159}$ Tb (terbium) was added to each of the digested samples and the mixtures were diluted with deionized water to a final volume of 10 mL. The lanthanide concentration of each sample was measured using a calibration curve of aqueous standards at 0.01, 0.1, 1.0, and 10 ppb for each lanthanide.

The performance of the instrument and accuracy of the results were monitored by analyzing a reagent blank and bovine serum control serum prior to analysis of the samples. Also, standard reference material (Peach Leaves 1547) obtained from National Institute of Standards and Technology (NIST, Gaithersburg, MD, USA) with known values of iron and rare earth elements was analyzed with each batch of samples.

The percent injected dose per gram of tissue, was calculated as $[Ln]_{sample}$ / ($[Ln]_{inj}$*$M_{inj}$) where $[Ln]_{sample}$ is the lanthanide concentration in the sample (blood or tumor tissue), $[Ln]_{inj}$ is the lanthanide concentration in the injected nanoparticle solution, and $M_{inj}$ is the mass of nanoparticle solution injected (0.2 grams). For tumor, kidney, and liver accumulation, ANOVA analysis was performed for the three nanoparticle formulations. Where differences were detected (tumor and kidney), individual t-tests were performed.

## 5.4 Results and Discussion

*Characterization of Native GC-SPIO and Control Nanoparticles*

Since previous studies have identified that the blood circulation times[20-23] and, consequently, tumor delivery is highly dependent on the size of SPIO nanoparticles, the hydrodynamic diameter of the native GC-SPIO and control nanoparticles (i.e. glycidol GC-SPIO, and dextran SPIO) was characterized by dynamic light scattering (DLS). Also, because of the need to distinguish pH-mediated delivery from a background level of EPR delivery, it was necessary to ensure that the native GC-SPIO and control nanoparticles had very similar size profiles. The peak sizes of the native GC-SPIO, glycidol GC-SPIO, and dextran SPIO were found to be 33.6 nm, 36.1 nm, and 29.8 nm, respectively. Since

the glycidol GC-SPIO particles were synthesized by direct chemical blockade of the pH sensitive amino groups of the native GC-SPIO, the glycidol GC-SPIO are necessarily slightly larger (2.5 nm). Although the size of dextran SPIO can be marginally tuned with varied synthetic conditions, these particles are necessarily slightly smaller (3.8 nm) than the native GC-SPIO, owing to the latter's additional GC coating. Given the close agreement in peak sizes and DLS size distributions (Figure 5.3) for the three nanoparticle formulations, it is assumed that differences in tumor delivery can be attributed to differences in the chemistry of their surface coat, as opposed to their hydrodynamic diameter.

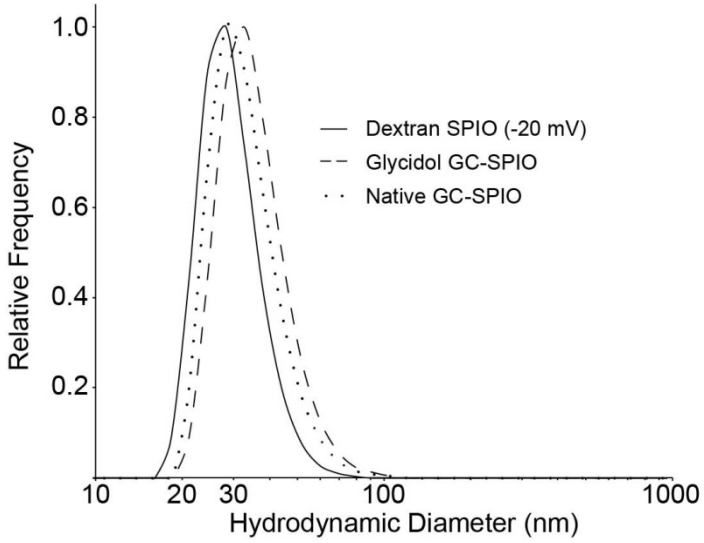


**Figure 5.3** Dynamic light scattering profiles of native GC-SPIO, glycidol GC-SPIO, and dextran SPIO nanoparticles in phosphate buffered saline, pH 7.4.

In order to examine the morphology of the iron cores of the nanoparticle formulations, and ensure their similarity, transmission electron micrographs (TEM) were obtained (Figure 2B). The average core sizes of the GC-based SPIO and dextran SPIO were found to be 19.8 ± 3.6 nm, and 19.4 ± 3.9 nm, respectively. Since only the surface coating was modified between the native GC-SPIO and glycidol GC-SPIO, these two formulations have matching core size characteristics. The morphology of iron cores appears similar for all three nanoparticle formulations and similar to previously published dextran SPIO images.[28]

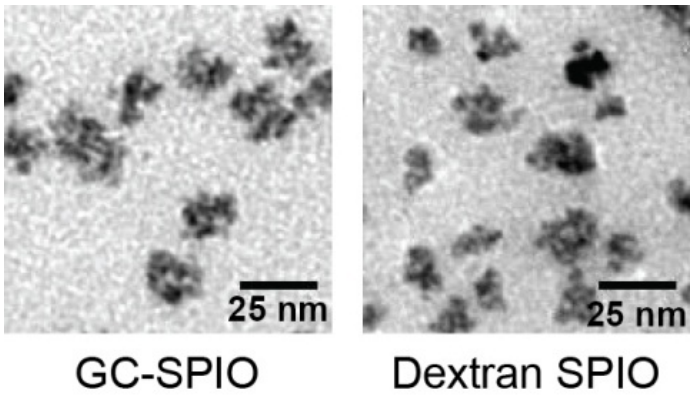


**Figure 5.4** Transmission electron microscopy (TEM) images of GC-SPIO and dextran SPIO demonstrating iron core size and morphology.

The metal and polymer composition of the native GC-SPIO nanoparticles was further examined by elemental analysis. Dried nanoparticles were 37.05% C, 2.87% N, 6.09% Fe, and 0.17% Gd by weight. Since only GC contains nitrogen, these data and the known molecular structure of dextran and GC allow for calculation of nanoparticle composition. The native GC-SPIO nanoparticles are, therefore, 6.09% iron, 0.17% gadolinium, 39.08% dextran, and 42.02% glycol chitosan. The remainder of the nanoparticles (12.67%) is a combination of oxygen in the nanoparticle core and any electrostatically associated salts.

Although comparison of tumor delivery via ICP-MS measurements is not influenced by the nanoparticles' magnetic properties, the comparison of *in vivo* MR tumor contrast certainly is. Therefore, it was important to ensure all three nanoparticle formulations had similar values for their relaxivities, especially the $R_2$ relaxivity, which is responsible for contrast enhancement on $T_2$* weighted MR images. $R_2$ values (pH 7.4, PBS) for the native GC-SPIO, glycidol GC-SPIO and dextran SPIO were measured as 146.5, 152.3, and 150.4 Fe $mM^{-1}$ $s^{-1}$, respectively. The native GC-SPIO demonstrated only a minor increase in R2 relaxivity (≈ 5%) as the pH decreased to 5.9, while the glycidol GC and dextran SPIO had no pH dependence to their R2 values. Although improved relaxivity for the native GC-SPIO at low pH values can further improve pH mediated contrast, this is not the primary mechanism by which contrast is generated. Rather, titration of the native GC-SPIO surface coat leads to greater accumulation of nanoparticles at the tumor. Given the R2 values for all three formulations were very similar at physiologic pH, it was concluded that there is no contrast bias for the native GC-SPIO.Finally, the surface charge (zeta potential), and its pH dependence, was examined for each of the nanoparticle formulations (Figure 5.5). The native GC-SPIO nanoparticle was found to have a near-neutral zeta potential (+0.3 mV) at physiologic pH = 7.4. It is important for tumor delivery that the native GC-SPIO have little or no positive surface charge at normal blood pH, since cationic materials are rapidly cleared from circulation, due to local electrostatic interactions, before they could reach a tumor.[29] Next, as the pH was lowered, the zeta potential continually increased and reached a value of +4.1 mV at pH = 6.65 and +8.2 mV at pH = 6.15. Therefore, it was confirmed that the native GC-SPIO nanoparticles had a surface coat capable of meaningfully sensing a pH

drop of 1.0 unit or less. Since a wide variety of cationic materials have been found to electrostatically associate with cells[25-28], it was expected that the surface properties of the native GC-SPIO nanoparticles would allow them to adhere to cells or negatively charged cellular matrix components in a pH-dependent manner that is favorable for detection of acidic environments.

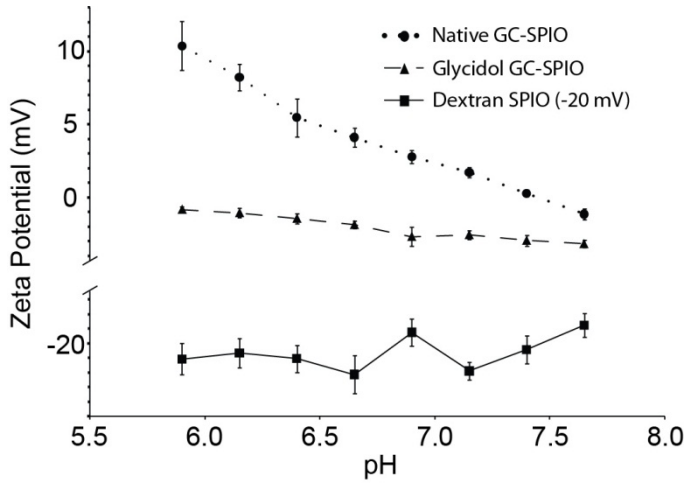


**Figure 5.5.** Zeta potential (surface charge) titration of native GC-SPIO, glycidol GC-SPIO and dextran SPIO nanoparticles at 100 μg/mL nanoparticle concentration in 10 mM HEPES buffer at various pH.

The pH-dependence of the surface charge was similarly investigated for the glycidol GC-SPIO and dextran SPIO nanoparticles (Figure 5.5). At physiologic pH = 7.4, the zeta potentials were -2.9 mV and -20.4 mV for the glycidol GC-SPIO and dextran SPIO, respectively. Upon lowering of the pH to 6.15, the zeta potentials changed to -1.0 mV and -20.7 mV. These results indicate that the surface charge of the control nanoparticles does not have significant pH dependence; under conditions that lead to an increase in the zeta potential of the native GC-SPIO by 7.9 mV, the glycidol GC-SPIO increased only 1.9 mV, and the dextran SPIO zeta potential dropped by 0.3 mV (a difference within the standard deviation of a given measurement). It should be noted that

the zeta potential of both control nanoparticles remains below 0 mV under every pH condition, such that not even an extremely acidic tumor environment would be able to induce electrostatic adherence of these nanoparticles.

It should be noted that the two GC-based nanoparticle formulations have similar (close to neutral) surface charge at physiologic pH = 7.4. In fact, their surface charges proved similar enough to give them overlapping blood circulation profiles (see below). The glycidol GC-SPIO control formulation, therefore, specifically isolates the EPR component of tumor delivery from the native GC-SPIO formulation, so that pH-mediated improvement can be assessed. The -20 mV dextran nanoparticles, along with dextran formulations investigated at other charges,[24] have zeta potentials encompassing the charge of native GC-SPIO at physiologic pH. Variations in surface charge can lead to differences in blood circulation times, and therefore, tumor delivery by EPR. Therefore, the dextran formulations make it possible to see if the delivery of native GC-SPIO compares favorably to the delivery obtainable by EPR alone, at any surface charge.

**Table 5.1** Summary of the physicochemical properties of native GC-SPIO, glycidol GC-SPIO, and dextran SPIO nanoparticles.

| Particle Surface | Tracer Lanthanide | Mean Hydrodynamic Diameter (nm) | Mean Core Size (nm)* | Zeta (mV) at pH = 7.4 | Zeta (mV) at pH = 6.15 | $R_2$ ($mM^{-1}s^{-1}$) | $R_1$ ($mM^{-1}s^{-1}$) |
|---|---|---|---|---|---|---|---|
| Native GC | Gd | 33.6 | 19.8 ± 3.6 | +0.3 | +8.2 | 146.5 | 7.5 |
| Glycidol GC | Gd | 36.1 | 19.8 ± 3.6 | -2.9 | -1.0 | 152.3 | 7.9 |
| Dextran | Sm | 29.8 | 19.4 ± 3.9 | -20.4 | -20.7 | 150.4 | 10.0 |

*Since the glycidol GC-SPIO was generated by direct surface modification of native GC-SPIO, core sizes for these formulations are identical.

*In Vitro pH Dependent Association of Native GC-SPIO*

Following the successful synthesis of the native GC-SPIO, possessing a favorably pH-dependent surface charge, as well as size and relaxivity matched pH-independent control nanoparticles, the ability of each formulation to label tumor cells *in vitro* and generate *in vitro* MR contrast was investigated under various pH conditions. Specifically, each nanoparticle formulation was incubated in triplicate with T6-17 tumor cells in culture medium at a concentration of 25 μg Fe/mL at pH values ranging from 5.9 to 7.65, in 0.25 unit increments. Following triplicate washing to remove unassociated nanoparticles, the $T_2$ relaxation times of the cell suspensions were measured to access the extent of cell association (Figure 5.6).

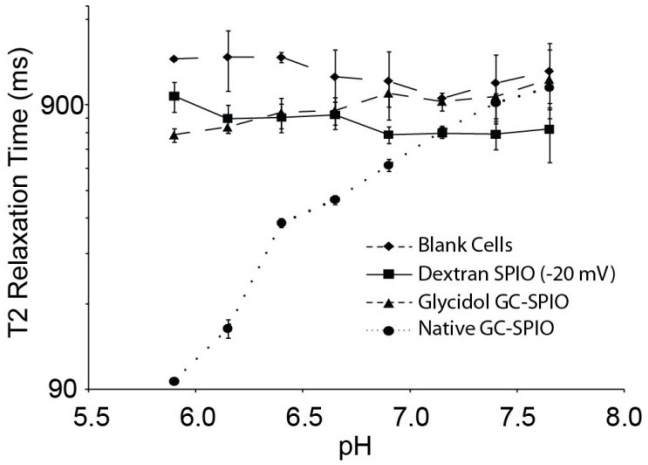


**Figure 5.6** *In-vitro* association of native GC-SPIO, glycidol GC-SPIO, and dextran SPIO nanoparticles with T6-17 cells. Nanoparticles were incubated in triplicate at 25 μg Fe/mL with 4 x $10^6$ T6-17 cells in culture medium buffered by 25 mM HEPES. After removal of unassociated nanoparticles, T2 relaxation times were collected for each cellular suspension.

Interestingly, it was found that cells incubated with native GC-SPIO nanoparticles exhibited a pronounced pH-dependence to their $T_2$ relaxation times. At physiologic pH = 7.4, the native GC-SPIO cells had an average $T_2$ relaxation time of 917 ms that was not statistically different from the $T_2$ relaxation times of cells incubated with either control nanoparticle or blank cells incubated without nanoparticles. However, when the pH was dropped only one quarter of a pH unit to 7.15, the average $T_2$ relaxation time of native GC-SPIO incubated cells dropped to 728 ms. Although not a particularly robust $T_2$ value, 728 ms was statistically different from the values of 950 ms and 927 ms observed for cells incubated without nanoparticles or glycidol GC-SPIO control nanoparticles, respectively. These results suggest that, under ideal conditions, the pH-titratable native GC-SPIO nanoparticles can differentially label cells in microenvironments only 0.25 pH units below physiologic value. After another 0.25 unit drop in pH to 6.90, the native GC-SPIO nanoparticle incubated cells obtained an average $T_2$ value of 553 ms, which was statistically different from blank cells and cells incubated with both control nanoparticle formulations. With further reductions in the incubation pH, the average $T_2$ value for cells incubated with native GC-SPIO continued to decrease, ultimately reaching values of 147 ms at pH 6.15 and 96 ms at pH 5.90.

Appropriately, neither the glycidol GC nor dextran SPIO control nanoparticles exhibited any meaningful pH-dependence in their cellular association. Although the glycidol GC-SPIO cells incubated at very low pH values (5.90 and 6.15) yielded $T_2$ relaxation times that were statistically different from the value at physiologic pH = 7.4, the $T_2$ values at low pH were still greater than 700 ms, indicating a weak signal. Recall that native GC-SPIO incubated cells had already reached this relaxation level at pH 7.15.

The statistically detectable difference in relaxation for the glycidol GC-SPIO incubated cells at the two extremes of pH is likely due to a small population of titratable amino groups remaining despite chemical blockade. For the dextran SPIO, there was no statistically detectable difference in cell association between the two ends of the pH spectrum.

It is also noteworthy that native GC-SPIO nanoparticles are able to produce $T_2$ relaxation times under 200 ms in these cell pellet studies at concentrations of only 25 μg Fe/mL. For comparison, actively targeted SPIO nanoparticles relying on receptor – ligand interactions have been tested under similar conditions and yielded similar $T_2$ relaxation times when incubated at concentrations of 150 μg Fe/mL.[32] Although such a comparison is not exact, these results indicate native GC-SPIO nanoparticles may be able to generate contrast of a magnitude similar to receptor targeted SPIO nanoparticles.

Following measurement of their $T_2$ relaxation times, the cell pellets were transferred to a well plate and a $T_2$* weighted MR image was acquired (Figure 4B). For the cells incubated with native GC-SPIO, signal loss can already be discerned at a pH of 7.15, only 0.25 units below physiologic pH. The signal loss becomes more pronounced as the incubation pH drops to 6.65 and at pH 6.15 and below the signal is lost entirely under these imaging parameters. Importantly, the cells incubated with glycidol GC and dextran SPIO control nanoparticles do not exhibit any marked pH-dependence in their MR signal intensity.

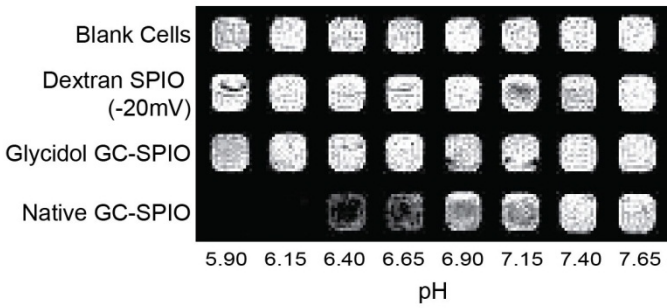


**Figure 5.7** Triplicate samples at each pH were combined into a single well of a 384-well plate and a T2* weighted MR image was obtained. Pellets with low T2 relaxation times, resulting from the presence of nanoparticles, appear with reduced signal intensity in the image.

*In Vivo MR Contrast Enhancement of Native GC-SPIO*

The ability of native GC-SPIO to generate MR contrast significantly greater than the background EPR effect was confirmed with an *in vivo* murine tumor model. Specifically, T6-17 flank tumors were grown in nude mice to a diameter of approximately 8 mm and then either native GC-SPIO or control nanoparticles at a dose of 10 mg Fe/kg body weight (approximately 0.2 mg of iron per animal) was administered intravenously. $T_2$* weighted MR images were acquired immediately prior to injection of nanoparticles and 24 hours after injection (Figure 5.8). The post contrast images of the native GC-SPIO nanoparticle demonstrated striking relative signal loss in the tumor. In the pre-contrast image shown, the tumor is located between iso-intense paraspinal and thigh muscles and is not clearly delineated. In the post-contrast image, however, the tumor is revealed as a hypo-intense heterogeneous region, with well-defined margins, exerting a mass effect against the adjacent paraspinal muscle. The heterogeneity of

intensity in the tumor is likely caused by impaired SPIO diffusion and penetration once they encounter a micro-region of sufficient acidity, either at the negatively charged vascular endothelium or within the tumor interstitium. Alternatively, the heterogeneity may reflect variations in extracellular pH within the tumor.[33] Neither the glycidol GC nor dextran SPIO control nanoparticles yielded significantly visible contrast enhancement between pre- and post-contrast images.

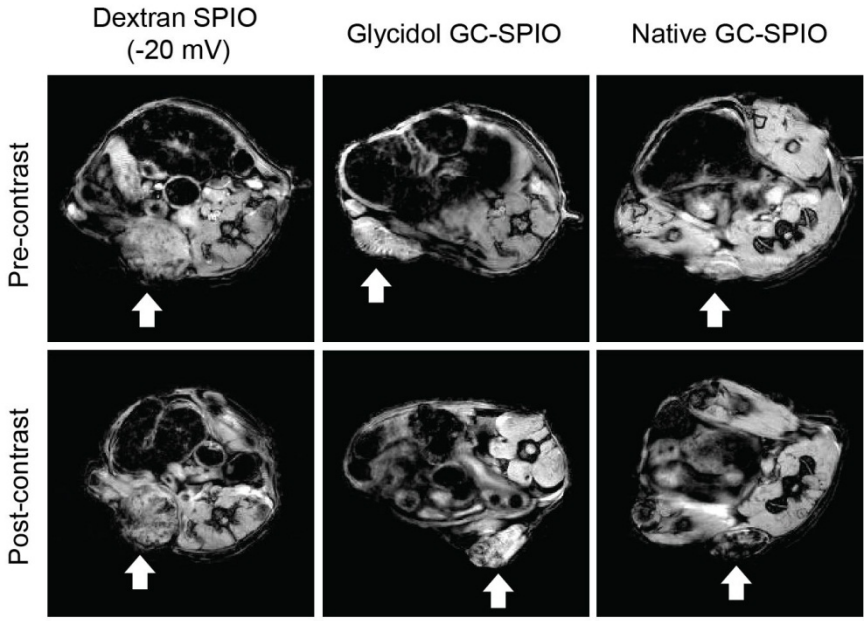


**Figure 5.8** *In vivo* pre- and post-contrast MR images of nu/nu nude mice with T6-17 flank tumors. Representative T2* weighted MR images in the axial plane prior to injection (pre-contrast) and 24 hours after injection (post-contrast) of native GC-SPIO (n=4), glycidol GC-SPIO (n=4) and dextran SPIO (n=3) nanoparticles. Tumor location is indicated by white arrows.

The MR signal in the tumor regions of interest (ROIs) were also analyzed quantitatively (Figure 5B). For each animal, three matching axial slices were examined pre- and post-contrast. Variations in absolute signal from slice to slice, due to mouse or RF coil positioning, were accounted for by normalizing the tumor signal to that of

adjacent paraspinal muscle on a slice by slice basis. The native GC-SPIO nanoparticles yielded a contrast enhancement (relative signal intensity ratio) of 0.50. In this scale, lower values indicate greater contrast, with 1.0 corresponding to no contrast and 0 indicating perfect contrast. Importantly, the contrast enhancement observed for native GC-SPIO nanoparticles was statistically different from that of glycidol GC and dextran SPIO, which had RSI ratios of 0.86 and 0.84, respectively.

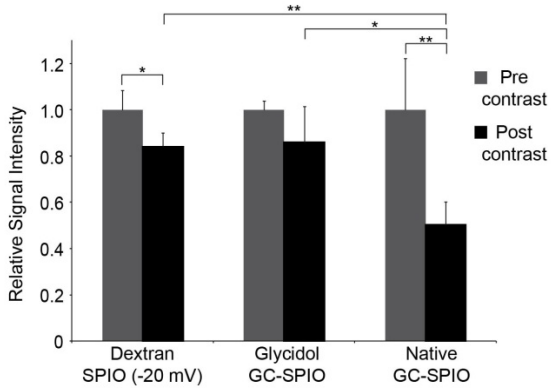


**Figure 5.9** Quantitative analysis of MR images of native GC-SPIO (n=4), glycidol GC-SPIO (n=4) and dextran SPIO (n=3). Signal intensity of each tumor was normalized to adjacent paraspinal muscle. For contrast measurement, the relative signal intensity, RSI, was calculated as the quotient of the post-contrast to pre-contrast normalized tumor intensity. For t-test statistical analysis of the groups, statistically significant values of $p<0.05$ are indicated with single asterisk and $p<0.005$ with double asterisk.

Interestingly, the RSI ratio obtained for these native GC-SPIO nanoparticles was comparable to that obtained in a study of actively targeted SPIO nanoparticles injected at the same concentration and directed against the same tumor cell line.[32] While many variables influence the contrast enhancement observed *in vivo*, it is encouraging to see that the pH-titratable native GC-SPIO nanoparticles can deliver contrast enhancement on the same order as actively targeted agents.

*Tumor Delivery and Blood Circulation*

To specifically examine the amount of nanoparticle delivery to the tumor, as well as investigate blood circulation profiles, the nanoparticle formulations were designed with unique lanthanide metal tracers that can be detected by ICP-MS. Immediately after the post-contrast images were acquired, each animal was sacrificed and the flank tumors removed. By comparing the amount of lanthanide tracer present in the excised tumors to the amount of lanthanide present in the original intravenous injection, the amount of nanoparticle delivery can be quantified as a percent of injected dose per gram of tumor tissue (Figure 5.10). Also, these data can be converted into absolute iron concentrations since the amount of injected material is known. The nanoparticle iron concentrations in the tumor were thus calculated as 2.5, 4.2, and 6.7 μg/mL for dextran, glycidol, and native GC-SPIO, respectively.

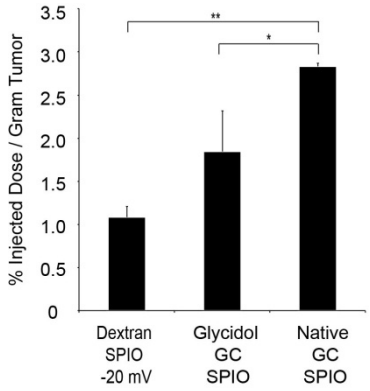


**Figure 5.10** Quantitative tumor delivery of native GC-SPIO, glycidol GC-SPIO, and dextran SPIO. Percent injected dose per gram of tumor tissue was calculated by measuring the concentration of lanthanide tracer in excised tumors using ICP-MS. For the native GC-SPIO, this converts to approximately 6.7 μg Fe / mL. For t-test statistical analysis of the groups, statistically significant values of $p<0.05$ are indicated with single asterisk and $p<0.005$ with double asterisk.

Interestingly, even though MR imaging yielded similar contrast enhancement for the glycidol GC-SPIO and dextran SPIO, there was significantly more nanoparticle delivery for the glycidol GC-SPIO. The contrast enhancement observed in MR images reflects the combination of many variables, including, but not limited to: concentration of agent in the tumor, MR pulse sequence parameters (e.g. TE), and nanoparticle relaxation characteristics (e.g. R2). Specifically, the nanoparticles have a dynamic concentration range in which they linearly decrease the tissue's relaxation time. For the SPIO used in this study the dynamic range, determined during *in vitro* relaxation measurements, was 1 – 50 μg/mL (Figure 5.11). Little contrast may be observed with nanoparticle concentrations at the low end of this range, significant improvements in contrast occur near the middle of the range, and saturation occurs at the top. It is likely that the nanoparticle concentrations achieved by dextran and glycidol GC-SPIO are very near the bottom of the dynamic range, still not high enough to generate significant contrast with the pulse sequence parameters used.

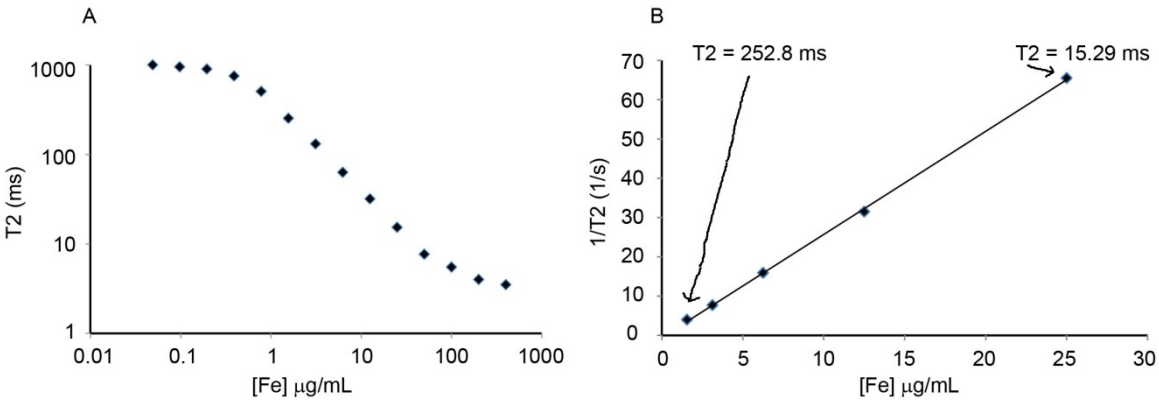


**Figure 5.11** MR signal response profile for native GC-SPIO. At T2 values lower than 5 ms, the signal becomes saturated and a T2 values greater than 900 ms, the signal is not discernibly different from baseline medium (**A**). The linear dynamic range of the native GC-SPIO, therefore, falls roughly between 1 – 50 μg Fe / mL (**B**).

The animals injected with native GC-SPIO nanoparticles showed a further significant increase in tumor delivery from the glycidol GC-SPIO. Importantly, this pH-mediated increase in nanoparticle delivery was sufficient to reach a concentration providing much more MR contrast. This demonstrates the importance of optimizing and maximizing nanoparticle delivery, since the incremental improvement in delivery (i.e. from glycidol GC-SPIO to native GC-SPIO) has the possibility to yield significant contrast improvement. It is envisioned that while a completely passive agent might not reach a concentration detectable on an MR image, the additional improvement in delivery obtained by a pH-sensitive agent could result in detectable MR contrast.

It has been well established that entirely passive tumor delivery of nanoparticles via EPR is a function of the pharmacodynamics of their blood circulation[20-23]. The two GC based formulations are of similar size, have a similar (although not exactly identical) zeta potential at the physiologic pH = 7.4, and have a surface coat constructed from the same polymer. These two formulations, therefore, were expected to have very similar blood circulation profiles. This important hypothesis was validated by using ICP-MS to measure the blood concentration for each nanoparticle as a function of time (Figure 5.12). As anticipated, the native GC-SPIO and glycidol GC-SPIO were found to have very well overlapped blood circulation profiles. Importantly, the small difference between the native GC-SPIO and glycidol GC-SPIO surface charge at physiologic pH did not alter their blood clearance. Therefore, it can be concluded that the incremental improvement in delivery that native GC-SPIO exhibits over glycidol GC-SPIO represents pH-mediated delivery, not attributable to EPR.

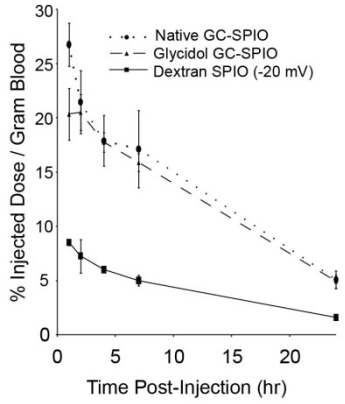


**Figure 5.12** Blood clearance of native GC-SPIO, glycidol GC-SPIO, and dextran SPIO (-20 mV) as measured by concentration of lanthanide tracer in the blood.

In order to see how the pH-enhanced tumor delivery of native GC-SPIO compares to the EPR that could be obtained with surface charges (other than neutral), it is helpful to examine the tumor delivery of the dextran SPIO nanoparticles at -20 mV and other zeta potentials. This can also rule out the possibility native GC-SPIO is simply adopting some positive charge, within its titration range, that would have produced high delivery even if the nanoparticle were fixed at that particular charge. Dextran SPIO with pH-independent zeta potentials of approximately -12 mV, -5 mV, +4 mV, +10 mV and +14 mV were intravenously administered to animals bearing T6-17 flank tumors Chapter 4.[24] Like the -20 mV dextran SPIO nanoparticles in this study, none of the pH-insensitive dextran SPIO nanoparticles accumulated as well as native-GC SPIO (i.e. statistically significant inferior delivery for every dextran SPIO nanoparticle, Figure 5.13). The lower delivery observed for the -20 mV and other charge dextran formulations correlated with their shorter blood residence times (Figure 5.12), characteristic of delivery by EPR. Importantly, the dextran SPIO with strongly positive surface charge accumulated especially poorly at the tumor site. It is, therefore, important for the mechanism of native GC-SPIO delivery that the

nanoparticles not constitutively display a large positive surface charge – rather only after entering the tumor microenvironment.

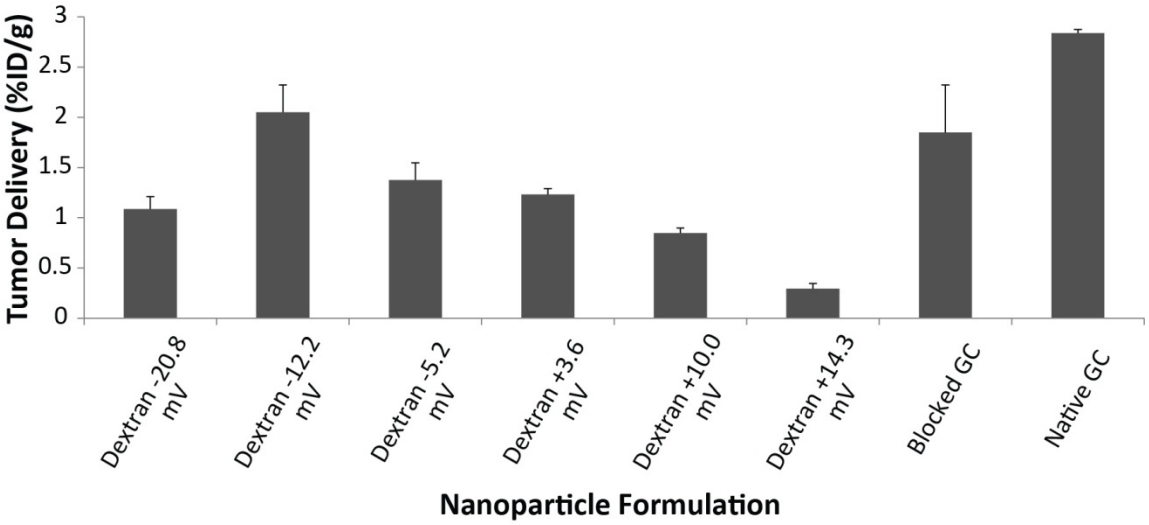


**Figure 5.13** Tumor delivery of native GC-SPIO compared to glycidol blocked GC-SPIO and dextran SPIO formulations with a wide range of pH-insensitive zeta potentials.

Finally, in addition to the pathological environment of a tumor, other groups investigating pH-responsive agents have demonstrated that there are physiologically normal sites of pH < 7.4, such as the renal tubular system.[34-36] Therefore, the delivery of native GC and control SPIO nanoparticles to the kidneys was examined. At 24 hours post-injection, the average renal concentrations, expressed as percent of injected dose per gram of kidney tissue, were found to be 4.49, 2.40, and 1.02 for native GC-SPIO, glycidol GC-SPIO and dextran SPIO (-20 mV), respectively (Figure 5.14). Given the longer blood residence times for the two GC based formulations, it is not surprising to observe a greater renal concentration at 24 hours for those formulations compared to the dextran SPIO. Interestingly, though, the renal concentration of the native GC-SPIO was a

statistically significant 87% higher than that of the glycidol GC-SPIO, despite very similar blood circulation profiles and identical blood concentrations at the 24 hour time point. Furthermore, the native GC-SPIO nanoparticles are not simply being deposited to a higher extent in all organs, since the concentrations of all three nanoparticles in the liver at 24 hours were not statistically distinct from one another. Despite the lack of statistical significance, the native-GC SPIO nanoparticles had a trend towards *less* accumulation in the liver (33.3 versus 44.9 and 37.9 for the glycidol GC and dextran SPIO, respectively, Figure 5.14).

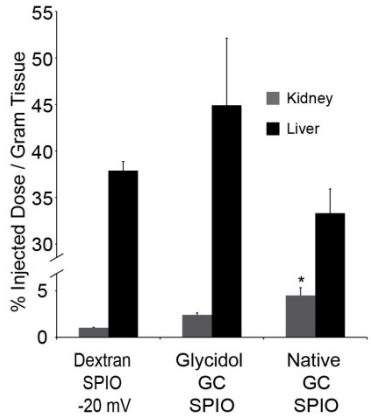


**Figure 5.14** Kidney and liver concentrations of native GC-SPIO, glycidol GC-SPIO, and dextran SPIO (-20 mV), 24 hours post-injection. Asterisk indicates statistical significance ($p<0.05$) between native GC-SPIO kidney uptake and either control nanoparticle.

## 5.5 Conclusion

The biocompatible and biodegradable polymer glycol chitosan can be used to impart pH-responsiveness to superparamagnetic iron oxide nanoparticles. The resulting material demonstrates a pH-dependent surface charge, allowing it achieve long blood circulation at physiologic pH = 7.4 and then transition to a cationic and adhesive form upon entering an acidic microenvironment pH < 7.0. These native GC-SPIO nanoparticles exhibited significantly improved accumulation in a murine tumor model, compared to nanoparticles with similar physical properties, but lacking pH-responsiveness. Higher levels of SPIO accumulation in the tumor also resulted in a clear and quantifiable improvement in magnetic resonance contrast, as shown on $T_2$*-weighted images. Generally, it is believed glycol chitosan could be used to exploit the metabolic profile of a wide range of malignancies and improve the tumor delivery of imaging or therapeutic agents, provided that synthesis of such agents preserves the pH-responsive amino group.

## 5.6 References


1. Tennant, D. A.; Duran, R. V.; Gottlieb, E., Targeting metabolic transformation for cancer therapy. *Nat Rev Cancer* **2010,** 10, (4), 267-77.

2. Basu, S.; Alavi, A., Revolutionary impact of PET and PET-CT on the day-to-day practice of medicine and its great potential for improving future health care. *Nucl Med Rev Cent East Eur* **2009,** 12, (1), 1-13.

3. Nagrath, D.; Caneba, C.; Karedath, T.; Bellance, N., Metabolomics for mitochondrial and cancer studies. *Biochim Biophys Acta* **2011,** 1807, (6), 650-63.

4. Ferreira, L. M., Cancer metabolism: the Warburg effect today. *Exp Mol Pathol* **2010,** 89, (3), 372-80.

5. Schornack, P. A.; Gillies, R. J., Contributions of cell metabolism and H+ diffusion to the acidic pH of tumors. *Neoplasia* **2003,** 5, (2), 135-45.

6. Gillies, R. J.; Raghunand, N.; Garcia-Martin, M. L.; Gatenby, R. A., pH imaging. A review of pH measurement methods and applications in cancers. *IEEE Eng Med Biol Mag* **2004,** 23, (5), 57-64.

7. Gillies, R. J.; Raghunand, N.; Karczmar, G. S.; Bhujwalla, Z. M., MRI of the tumor microenvironment. *J Magn Reson Imaging* **2002,** 16, (4), 430-50.

8. Stubbs, M.; Bhujwalla, Z. M.; Tozer, G. M.; Rodrigues, L. M.; Maxwell, R. J.; Morgan, R.; Howe, F. A.; Griffiths, J. R., An assessment of 31P MRS as a method of measuring pH in rat tumours. *NMR Biomed* **1992,** 5, (6), 351-9.

9. Bhujwalla, Z. M.; McCoy, C. L.; Glickson, J. D.; Gillies, R. J.; Stubbs, M., Estimations of intra- and extracellular volume and pH by 31P magnetic resonance spectroscopy: effect of therapy on RIF-1 tumours. *Br J Cancer* **1998,** 78, (5), 606-11.

10. van Sluis, R.; Bhujwalla, Z. M.; Raghunand, N.; Ballesteros, P.; Alvarez, J.; Cerdan, S.; Galons, J. P.; Gillies, R. J., In vivo imaging of extracellular pH using 1H MRSI. *Magn Reson Med* **1999,** 41, (4), 743-50.

11. Aime, S.; Barge, A.; Delli Castelli, D.; Fedeli, F.; Mortillaro, A.; Nielsen, F. U.; Terreno, E., Paramagnetic lanthanide(III) complexes as pH-sensitive chemical exchange saturation transfer (CEST) contrast agents for MRI applications. *Magn Reson Med* **2002,** 47, (4), 639-48.

12. Wu, Y.; Soesbe, T. C.; Kiefer, G. E.; Zhao, P.; Sherry, A. D., A responsive europium(III) chelate that provides a direct readout of pH by MRI. *J Am Chem Soc* **2010,** 132, (40), 14002-3.

13. Thorek, D. L.; Chen, A. K.; Czupryna, J.; Tsourkas, A., Superparamagnetic iron oxide nanoparticle probes for molecular imaging. *Ann Biomed Eng* **2006,** 34, (1), 23-38.

14. Deng, Z.; Zhen, Z.; Hu, X.; Wu, S.; Xu, Z.; Chu, P. K., Hollow chitosan-silica nanospheres as pH-sensitive targeted delivery carriers in breast cancer therapy. *Biomaterials* **2011,** 32, (21), 4976-86.

15. Shenoy, D.; Little, S.; Langer, R.; Amiji, M., Poly(ethylene oxide)-modified poly(beta-amino ester) nanoparticles as a pH-sensitive system for tumor-targeted delivery of hydrophobic drugs. 1. In vitro evaluations. *Mol Pharm* **2005,** 2, (5), 357-66.

16. Chawla, J. S.; Amiji, M. M., Biodegradable poly(epsilon -caprolactone) nanoparticles for tumor-targeted delivery of tamoxifen. *Int J Pharm* **2002,** 249, (1-2), 127-38.

17. Lee, E. S.; Na, K.; Bae, Y. H., Polymeric micelle for tumor pH and folate-mediated targeting. *J Control Release* **2003,** 91, (1-2), 103-13.

18. Paquet, C.; de Haan, H. W.; Leek, D. M.; Lin, H. Y.; Xiang, B.; Tian, G.; Kell, A.; Simard, B., Clusters of superparamagnetic iron oxide nanoparticles encapsulated in a hydrogel: a particle architecture generating a synergistic enhancement of the T2 relaxation. *ACS Nano* **2011,** 5, (4), 3104-12.

19. Li, Q.; Dunn, E. T.; Grandmaison, E. W.; Goosen, M. F. A., Applications and Properties of Chitosan. *J Bioact Compat Pol* **1992,** 7, (4), 370-397.

20. Enochs, W. S.; Harsh, G.; Hochberg, F.; Weissleder, R., Improved delineation of human brain tumors on MR images using a long-circulating, superparamagnetic iron oxide agent. *J Magn Reson Imaging* **1999,** 9, (2), 228-32.

21. Moore, A.; Marecos, E.; Bogdanov, A., Jr.; Weissleder, R., Tumoral distribution of long-circulating dextran-coated iron oxide nanoparticles in a rodent model. *Radiology* **2000,** 214, (2), 568-74.

22. Zimmer, C.; Weissleder, R.; Poss, K.; Bogdanova, A.; Wright, S. C., Jr.; Enochs, W. S., MR imaging of phagocytosis in experimental gliomas. *Radiology* **1995,** 197, (2), 533-8.

23. Zimmer, C.; Wright, S. C., Jr.; Engelhardt, R. T.; Johnson, G. A.; Kramm, C.; Breakefield, X. O.; Weissleder, R., Tumor cell endocytosis imaging facilitates delineation of the glioma-brain interface. *Exp Neurol* **1997,** 143, (1), 61-9.

24. Crayton, S. H.; Elias, D. R.; Cheng, Z.; Al Zaki, A.; Tsourkas, A., ICP-MS analysis of lanthanide-doped iron oxide nanoparticles as a non-radiative, multiplex approach to quantify nanoparticle biodistribution. **2011**.

25. Frank, J. A.; Anderson, S. A.; Kalsih, H.; Jordan, E. K.; Lewis, B. K.; Yocum, G. T.; Arbab, A. S., Methods for magnetically labeling stem and other cells for detection by in vivo magnetic resonance imaging. *Cytotherapy* **2004,** 6, (6), 621-5.

26. Lewin, M.; Carlesso, N.; Tung, C. H.; Tang, X. W.; Cory, D.; Scadden, D. T.; Weissleder, R., Tat peptide-derivatized magnetic nanoparticles allow in vivo tracking and recovery of progenitor cells. *Nat Biotechnol* **2000,** 18, (4), 410-4.

27. Montet-Abou, K.; Montet, X.; Weissleder, R.; Josephson, L., Cell internalization of magnetic nanoparticles using transfection agents. *Mol Imaging* **2007,** 6, (1), 1-9.

28. Thorek, D. L.; Tsourkas, A., Size, charge and concentration dependent uptake of iron oxide particles by non-phagocytic cells. *Biomaterials* **2008,** 29, (26), 3583-90.

29. Chouly, C.; Pouliquen, D.; Lucet, I.; Jeune, J. J.; Jallet, P., Development of superparamagnetic nanoparticles for MRI: effect of particle size, charge and surface nature on biodistribution. *J Microencapsul* **1996,** 13, (3), 245-55.

30. Moghimi, S. M.; Davis, S. S., Innovations in avoiding particle clearance from blood by Kupffer cells: cause for reflection. *Crit Rev Ther Drug Carrier Syst* **1994,** 11, (1), 31-59.

31. Moghimi, S. M.; Hunter, A. C.; Murray, J. C., Long-circulating and target-specific nanoparticles: theory to practice. *Pharmacol Rev* **2001,** 53, (2), 283-318.

32. Elias, D. R.; Cheng, Z.; Tsourkas, A., An intein-mediated site-specific click conjugation strategy for improved tumor targeting of nanoparticle systems. *Small* **2010,** 6, (21), 2460-8.

33. Gallagher, F. A.; Kettunen, M. I.; Day, S. E.; Hu, D. E.; Ardenkjaer-Larsen, J. H.; Zandt, R.; Jensen, P. R.; Karlsson, M.; Golman, K.; Lerche, M. H.; Brindle, K. M.,

Magnetic resonance imaging of pH in vivo using hyperpolarized 13C-labelled bicarbonate. *Nature* **2008,** 453, (7197), 940-3.

34. Andreev, O. A.; Dupuy, A. D.; Segala, M.; Sandugu, S.; Serra, D. A.; Chichester, C. O.; Engelman, D. M.; Reshetnyak, Y. K., Mechanism and uses of a membrane peptide that targets tumors and other acidic tissues in vivo. *Proc Natl Acad Sci U S A* **2007,** 104, (19), 7893-8.

35. Andreev, O. A.; Engelman, D. M.; Reshetnyak, Y. K., Targeting acidic diseased tissue: New technology based on use of the pH (Low) Insertion Peptide (pHLIP). *Chim Oggi* **2009,** 27, (2), 34-37.

36. Vavere, A. L.; Biddlecombe, G. B.; Spees, W. M.; Garbow, J. R.; Wijesinghe, D.; Andreev, O. A.; Engelman, D. M.; Reshetnyak, Y. K.; Lewis, J. S., A novel technology for the imaging of acidic prostate tumors by positron emission tomography. *Cancer Res* **2009,** 69, (10), 4510-6.

# Chapter 6: Summary Discussion, Future Directions and Concluding Remarks

## 6.1 Summary Discussion

### 6.1.1 ICP-MS Multiplexing Analysis Applied *in vivo*

Since it was first used to analyze amino acids in 1958,[1] mass spectrometry (MS) has become an extremely powerful tool in the investigation of biological samples. For example, mass spectrometry, combined with powerful computational methods, plays a critical role in the field of proteomics and metabolomics.[2] MS can facilitate the identification of protein bands on gels using peptide mass fingerprinting[3] and can be used for de novo peptide sequencing.[4] When MS is coupled to a very high temperature plasma source (ICP-MS) elemental analysis of complex biological samples becomes possible. Recently, it was recognized that unique elemental isotopes (e.g. of lanthanides) could be used to "tag" biomolecules for identification and quantitation by ICP-MS.[5] Given the very large window of atomic masses not normally observed in biological samples, very high order multiplex analysis becomes possible. This remarkable capability was very recently (May 2011) combined with flow cytometry to yield a technique dubbed "mass cytometry".[6] Specifically, conjugated metal isotopes were used to simultaneously measure the binding of 31 antibodies to single cells. This detailed level of analysis (3 – 4 times more powerful than state of the art multi-color flow cytometry) revealed previously unappreciated cell signaling and phosphorylation responses in human hematopoietic cells. The objective of this thesis was to demonstrate the applicability of ICP-MS multiplex analysis to supra-molecular assemblies (i.e. nanoparticles), and more

importantly, pave the way for high-order multiplexing of *in vivo* data such as pharmacokinetics and biodistribution.

Firstly, lanthanide metals were used to tag superparamagnetic iron oxide (SPIO), a promising and widely-researched T2-weighted magnetic resonance contrast agent. A synthetic protocol to stably incorporate the lanthanide metals into the core of SPIO nanoparticles, without abolishing their magnetic properties, was developed. The lanthanide dopant can be used as a unique tracer atom, allowing the sensitive and quantitative detection of the entire nanoparticle by ICP-MS, both *in vitro* and *in vivo*, without interference from endogenous signals. When distinct lanthanide metals are incorporated into nanoparticles with distinct physicochemical properties, ICP-MS allows for the concentration of each nanoparticle formulation to be measured independently of other formulations that may be present in the solution or tissue of interest. As a proof of principle, this ICP-MS multiplex approach was used to evaluate the effect of nanoparticle size and surface charge on tumor delivery, biodistribution, and blood clearance *in vivo*. The results obtained were consistent with the general literature consensus about these properties and only required a small number of experimental animals, due to the inherent and robust statistical power of a multiplex (ratiometric) approach. Furthermore, it is envisioned that the ICP-MS multiplex analysis could prove to be a powerful future research tool in the investigation of other less well-characterized physicochemical properties.

Secondly, more generalizable methods of lanthanide incorporation were pursued. It was found that in addition to precipitating lanthanide metals into the core of SPIO nanoparticles, it is also possible to incorporate lanthanides into liposomes,

polymersomes, and dendrimeric formulations using either encapsulation or chelation. Therefore, it is envisioned that any nanoparticle formulation amenable to labeling with a metal radionuclide would also be suitable for labeling with an ICP-MS metal tracer. Some other types of nanoparticles (*e.g.* gold and silver nanoparticles) inherently contain an ICP-MS metal tracer, without any further need for labeling. In addition to providing a quantitative method of detection with high sensitivity, ICP-MS tracers provide two potential benefits over conventional radiolabeling. Namely, they have the ability to easily multiplex a large number of signals in a single fluid or tissue sample while avoiding the hazards of handling radioactivity. Consequently, ICP-MS based multiplex analysis can be applied to a very wide variety of nanoparticle and macropharmaceutical formulations and allows for "higher throughput" evaluation of the pharmacokinetics and biodistribution of such agents in animals models.

Since active targeting of pathologies *in vivo* at the molecular level is an extremely promising and actively pursued strategy in nanotechnology, we sought to demonstrate how ICP-MS multiplexing could be exploited to streamline the evaluation of actively targeted nanoparticles in vivo. Specifically, SPIO nanoparticles were synthesized with a variety of lanthanide tracer metals and all had overlapping size distributions, so that they exhibit equal levels of passive tumor accumulation. These Ln-SPIO formulations were then be subsequently functionalized with active targeting ligands, such that each targeting ligand is associated with a specific lanthanide tracer. The binding of these nanoparticles to two tumor cell lines, with varying expression levels of three specific receptors, was examined *in vitro* with conventional methods such as flow cytometry. Then ICP-MS analysis was used to independently quantify the cell labeling of each nanoparticle,

compared to a non-targeted formulation, in a single sample. Therefore, it should become feasible in a single study to investigate *in vivo* many nanoparticle active targeting and negative control formulations, collecting data such as nanoparticle blood residence time, tumor delivery, and biodistribution. This represents a powerful tool for nanotechnology investigators to more thoroughly evaluate a greater number of nanoparticle formulations *in vivo*, while reducing experiment time, cost, and number of animals.

### 6.1.2 Development of pH-Responsive SPIO

Another major avenue of investigation in this thesis was the design of a novel pH-sensitive SPIO nanoparticle for relative pH imaging of acidic tumor microenvironments. Such an approach provides a complimentary approach to absolute pH imaging by MRS (where the pH is determined by the chemical shift of the probe) or CEST (where changes in pH influence the chemical exchange kinetics). With a relative pH probe, the goal is to detect regions of relatively abnormal pH by designing agents that preferentially accumulate in these regions. That is, the identity of the signal is not influenced by pH, but the biodistribution of the agent is influenced by pH. In this respect, such an agent has much in common with a classic receptor/ligand actively targeted molecule; the agent washes into the tumor through the enhanced permeability of the tumor vasculature and then is preferentially retained at the tumor site through pH mediated alterations in the nanoparticle's physicochemical properties.

It was found that the biocompatible and biodegradable polymer glycol chitosan can be used to impart pH-responsiveness to superparamagnetic iron oxide nanoparticles.

The resulting material demonstrates a pH-dependent surface charge, allowing it achieve long blood circulation at physiologic pH = 7.4 and then transition to a cationic and adhesive form upon entering an acidic microenvironment pH < 7.0. These native GC-SPIO nanoparticles exhibited significantly improved accumulation in a murine tumor model, compared to nanoparticles with similar physical properties, but lacking pH-responsiveness. Higher levels of SPIO accumulation in the tumor also resulted in a clear and quantifiable improvement in magnetic resonance contrast, as shown on $T_2$*-weighted images. Generally, it is believed glycol chitosan could be used to exploit the metabolic profile of a wide range of malignancies and improve the tumor delivery of imaging or therapeutic agents, provided that synthesis of such agents preserves the pH-responsive amino group.

## 6.2 Future Directions

### 6.2.1 Completion of Active Targeting Comparison *in vivo*

In chapter 4, we used ICP-MS multiplex analysis to evaluate cell labeling of multiple actively targeted SPIO nanoparticles, compared to a non-targeted formulation, all in a single *in vitro* measurement. The final logical experiment, clearly, is to complete the *in vivo* characterization of these nanoparticles. Specifically, the HER2-SPIO, RGD-SPIO, LDS-SPIO, and Blank-SPIO will be pooled into a single sample and administered intravenously to tumor bearing mice. Optimally, the animal subjects will bear both the "receptor-high" T6-17 tumors and "receptor low" HeLa tumors on opposite flanks. This will allow blood clearance of the four Ln-SPIO formulations, as well as tumor delivery to both cell lines, to be evaluated in a single animal.

### 6.2.2 Future Applications of in vivo ICP-MS Multiplex Analysis

This thesis only begins to explore the possibilities of what information can be obtained from *in vivo* use of ICP-MS multiplex analysis. For example, the effect of SPIO nanoparticle size and charge on passive tumor delivery and biodistribution were assessed, so that the results obtained could be compared to the general literature consensus of these effects.[7-10] However, there are many other physicochemical properties (*e.g.* shape, surface chemistry, elasticity, and other mechanical properties) that can affect nanoparticle tumor delivery and biodistribution, all of which are less fully understood and could be investigated using this method.

Additionally, the ICP-MS multiplex method could aid in the evaluation of more nuanced questions in the field of nanoparticle active targeting. Specifically, the ICP-MS multiplex approach could be used to compare variations of a given actively targeted nanoparticle. For example, different ligand types, such as an antibody, single chain antibody fragment (scFv), or small affinity peptide could be quantitatively compared. Or, within a given class of ligand, different specific sequences could be compared (i.e. several affinity peptide sequences obtained from phage display). Furthermore, it is being appreciated that optimal cell binding and in vivo delivery is not necessarily achieved by coating a nanoparticle with the maximum possible ligand density. Thus, ICP-MS multiplex analysis presents a powerful tool to evaluate the effect of ligand density. Also, active targeting of nanoparticles displaying ligands for two or more targets could be compared against more conventional single ligand formulations.

The ICP-MS multiplex approach could also be adapted to more specialized research questions. For example, nanoparticle trafficking and metabolism could be probed by labeling different components of the nanoparticle with different lanthanides

(e.g. encapsulating one metal within a liposome core and chelating another metal to the lipid membrane component). Or chelation stability could be evaluated *in vivo* by constructing a given nanoparticle formulation but using different chelators to incorporate the metal. In general, it is envisioned the ICP-MS multiplex method could be exploited to answer any research question involving the *in vivo* comparison of two or more agents that are amenable to lanthanide labeling.

Furthermore, it is envisioned that the spatial distribution of each nanoparticle within an organ or other tissue sample could also be obtained with the use of laser ablation ICP-MS.[11] With LA-ICP-MS, the tissue sample is directly vaporized, layer-by-layer, with a pulsed laser and transported into the mass analyzer.[12] Another potential advantage of LA-ICPS-MS is the ability to process microgram samples sizes, which could be required for the analysis of smaller organs or specialized tissue (e.g. lymph nodes, adrenal glands).

### 6.2.3 Use of ICP-MS Multiplex Analysis to Generate Standardized Data

Another promising application of this multiplex ICP-MS method is the potential to generate standardized data that can be compared between studies and between laboratories. With so many research groups engaged in the development of nanoparticles, a myriad of different formulations have been synthesized for both imaging and therapeutic applications.[13] Even when nanoparticle (payload) delivery is quantitatively reported, it is difficult for one group to ascertain whether their formulation resulted in better delivery than another's, given the numerous variables, known and unknown, involved in an *in vivo* study. This is a particularly significant problem in the nanoparticle

field, and one that hinders the progress of nanoparticles into clinical evaluation.[14] However, if a rigorously standardized and highly reproducible lanthanide-doped nanoparticle (such as a G5 dendrimer with tightly chelated lanthanide) were available, each group could co-inject the standardized nanoparticle along with their investigational one. The delivery of the investigational agent could, therefore, be reported not only in absolute terms, but also as a ratio to the standardized particle. Such a ratiometric approach could facilitate accurate comparisons between various investigational agents.

### 6.2.4 Future Applications of pH-Responsive Glycol Chitosan and SPIO

Chapter four of this thesis demonstrated the success of using a glycol chitosan (GC) coating to increase the tumor delivery of SPIO nanoparticles based on tumor acidity. There are a number of possible ways to improve and adapt this approach for future investigational agents. For example, glycol chitosan is only one of a number of pH-responsive polymers or peptides that could be used to sense relative changes in pH. Future work could focus on using GC or another polymer to optimize the nanoparticle's titration curve, with respect to starting zeta potential at physiologic pH, the pH at which charge transition begins to occur, and the steepness of the charge switch. Such studies could lead to an agent capable of sensing smaller deviations in pH while further reducing background accumulation at physiologic pH values.

Secondly, GC itself could be investigated as a pH sensor for imaging and therapeutic platforms in addition to SPIO. For example, a T1-weighted MR contrast agent could be developed by decorating a fraction of GC's functional amino groups with small generation dendrimers, each carrying many gadolinium chelates. Similarly, incorporation

of $^{64}$Cu chelates could produce a novel pH-sensitive PET probe. Beyond imaging applications, GC could be incorporated into the design of drug-carrying nanoparticle formulations (e.g. polymeric micelles or nanovesicles) in order to facilitate chemotherapeutic delivery to tumors.

Finally, it may be possible to use the pH-dependent titration of GC to make measurements of absolute pH using chemical exchange saturation transfer (CEST). That is, the amine protons of the glycol chitosan should exhibit variable chemical exchange kinetics depending on the pH of their local environment. If a lower molecular weight form of GC were administered with large enough concentration, a saturation pulse could be applied on its N-H resonance, and the rate of saturation transfer to bulk water could be used as a pH meter *in vivo*.

## 6.3 Concluding Remarks

Over the last two decades, the development of quantitative high-throughput analytical methods has revolutionized the process of molecular discovery and characterization *in vitro*. ICP-MS is increasing being used in these kinds of parallel processing of biological samples *in vitro*, as evidenced by the recent development of mass cytometry. In the future, we envision that "higher-throughput" evaluation of agents at the *in vivo* level using ICP-MS multiplex analysis may constitute a powerful tool to accelerate their pre-clinical evaluation in animal models. Further improvements to modularity and automation of lanthanide labeling (i.e. massively parallel conjugation of preformed metal-chelate complexes to macropharmaceuticals in robotically controlled reactions) would facilitate the use of *in vivo* ICP-MS multiplex analysis on a wider scale.

## 6.4 References


1. Andersson, C., *Acta. Chem. Scand.* 1958, 12, 1353.

2. Dettmer, K.; Aronov, P. A.; Hammock, B. D., Mass spectrometry-based metabolomics. *Mass Spectrom Rev* 2007, 26, 51-78.

3. Thiede, B.; Hohenwarter, W.; Krah, A.; Mattow, J.; Schmid, M.; Schmidt, F.; Jungblut, P. R., Peptide mass fingerprinting. *Methods* 2005, 35, 237-47.

4. Bandeira, N.; Olsen, J. V.; Mann, J. V.; Mann, M.; Pevzner, P. A., Multi-spectra peptide sequencing and its applications to multistage mass spectrometry. *Bioinformatics* 2008, 24, i416-23.

5. Lou, X.; Zhang, G.; Herrera, I.; Kinach, R.; Ornatsky, O.; Baranov, V.; Nitz, M.; Winnik, M. A., Polymer-based elemental tags for sensitive bioassays. *Angew Chem Int Ed Engl* 2007, 46, 6111-4.

6. Bendall, S. C.; Simonds, E. F.; Qiu, P.; Amir el, A. D.; Krutzik, P. O.; Finck, R.; Bruggner, R. V.; Melamed, R.; Trejo, A.; Ornatsky, O. I.; Balderas, R. S.; Plevritis, S. K.; Sachs, K.; Pe'er, D.; Tanner, S. D.; Nolan, G. P., Single-cell mass cytometry of differential immune and drug responses across a human hematopoietic continuum. *Science* 2011, 332, 687-96.

7. Moghimi, S. M.; Davis, S. S., Innovations in avoiding particle clearance from blood by Kupffer cells: cause for reflection. *Crit Rev Ther Drug Carrier Syst* 1994, 11, 31-59.

8. Moghimi, S. M.; Hunter, A. C.; Murray, J. C., Long-circulating and target-specific nanoparticles: theory to practice. *Pharmacol Rev* 2001, 53, 283-318.

9. Poznansky, M. J.; Juliano, R. L., Biological approaches to the controlled delivery of drugs: a critical review. *Pharmacol Rev* 1984, 36, 277-336.

10. Tomalia, D. A.; Reyna, L. A.; Svenson, S., Dendrimers as multi-purpose nanodevices for oncology drug delivery and diagnostic imaging. *Biochem Soc Trans* 2007, 35, 61-7.

11. Hsieh, Y. K.; Jiang, P. S.; Yang, B. S.; Sun, T. Y.; Peng, H. H.; Wang, C. F., Using laser ablation/inductively coupled plasma mass spectrometry to bioimage multiple elements in mouse tumors after hyperthermia. *Anal Bioanal Chem* 2011, 401, 909-15.

12. Koch, J.; Gunther, D., Review of the state-of-the-art of laser ablation inductively coupled plasma mass spectrometry. *Appl Spectrosc* 2011, 65, 155-62.

13. Jain, K. K., Advances in the field of nanooncology. *BMC Med* 2010, 8, 83.

14. Stark, W. J., Nanoparticles in biological systems. *Angew Chem Int Ed Engl* 2011, 50, 1242-58.